SPACE TRAFFIC CAMERA AS AN OPPORTUNISTIC SENSOR TOWARDS REAL-TIME SPACE DOMAIN AWARENESS

SIDDHARTH DAVE

A DISSERTATION SUBMITTED TO
THE FACULTY OF GRADUATE STUDIES
IN PARTIAL FULFILLMENT OF THE REQUIREMENTS
FOR THE DEGREE OF
DOCTOR OF PHILOSOPHY

GRADUATE PROGRAM IN EARTH AND SPACE SCIENCE
YORK UNIVERSITY
TORONTO, ONTARIO

December, 2022

Abstract

The space domain is a congested and contested environment that requires constant surveillance for risk assessment. The adequacy of current and future space domain awareness is limited by our ability to collect quantitative information of the events in low Earth orbit. A network of scalable and geographically distributed sensors has the potential to collect a large volume of data for a more complete sky coverage than is possible today. Classic terrestrial and space surveillance sensors are too large and unsuitable to scale for better distribution and coverage. Spacecraft mounted star trackers present a novel opportunity to collect valuable surveillance data using commercially-proven technologies. Research presented in this dissertation evaluates scalability and detection performance, establishes an image processing and data compression framework, and describes the experimental validation of a prototype sub-orbital mission. The dissertation concludes that the potential data collection capacity of space traffic cameras, adopted from star trackers, are feasible to achieve the desired data volume for improved low Earth orbit surveillance. The sensor network discussed can provide novel access with improved re-visit times to detect, track and classify resident space objects to augment existing space domain awareness (SDA) capabilities. This conclusion is presented in the context of data collection utility and quantity, data processing and means of centralization, and sensor design and feasibility survey. The conclusion is further supported with the knowledge that the necessary hardware required for data collection, i.e., the current count of active star trackers in Earth orbit, is already in place, and is expected to multiply due to increasing launch cadence. The results also suggest that such a network of space traffic cameras is a more cost effective approach for space surveillance, as the design presented can be automated and scalable to large constellations. The data collected can be used for space object characterization studies for development of in-orbit services in addition to spacecraft custody operations. The research concludes with recommendations for future work that further advance the usage of existing low-cost

commercial hardware for space domain awareness. Quantitative data collection is critical towards a real-time, low-cost, automated space surveillance and traffic management system. The contributions of this research demonstrate a sustainable method to achieve commercial space safety and remote services in low Earth orbit.

Dedication

To saving space, the last and most important Earth environment for the future of human civilization

Acknowledgements

As with any multi-year effort, this research would not be possible without many important people in my life. I want to thank my supervisor Dr. Regina S. K. Lee for being an outstanding mentor, guide, teacher and role model. Without her, I would still be drawing on paper with crayons. I want to thank my wife, soon to be Dr. Surabhi Guruprasad, for her unconditional love and support. Her dedication to my success is endearing. I want to thank my parents, Ghanshyam Dave and Hemangini Dave, for their devotion and sacrifice and for instilling me with good values, morals and humour. Their support for my education, and my grandfather's (Babulal Dave) and grandmother's (Kalavati Dave), has taught me to set high standards of myself. I especially want to thank Dr. Ryan Clark for being an amazing best man, friend, mentor, role-model and collaborator. Completing my degree would not be possible without Ryan's optimism and enthusiasm. I want to thank Dr. Donald Bédard for being an amazing adviser, and instilling me with confidence and giving me room to establish a sense of value for my work. I will continue to seek your guidance and support. I want to thank, soon to be Dr., Akash Chauhan for being an amazing best friend, inspiration and support, and for listening to my crazy ideas and sharing even crazier ones with me. I know we will continue our banter forever, and I look forward to all of it. Special thanks to Dr. Hugh Podmore for being an amazing role-model and providing positive encouragement to a novice graduate student. I want to thank all my friends and family for listening to me say *I'll be done in a month* for 2 years straight and still believing that I would actually finish at some point. Well that day is here. I want to thank all my lab mates, Thong Thai, Gabriel (Don't touch me), Perushan (left bicep), Andrea (under the bus), Vithurshan (atmosphere lover), Angel (Frenchie), Shamil (Tatar), KJ (excel lover), Nick (Dungeon Master), Diane (fighter pilot) and Randa (secretly vegan?). I want to thank my family and friends in India and Canada for their continued support. And at last my dearest cat Mittu for staying up many nights with me and providing many free licks.

Table of Contents

List of Tables

List of Figures

Acronyms

CCD charged-couple device.

CMOS complementary metal-oxide semiconductor.

CNN convolutional neural network.

CONOPS concept of operations.

FAI fast auroral imager.

GEO Geostationary Earth orbit.

LEO low Earth orbit.

MOT multi-object tracking.

POBC payload on-board computer.

PSF point spread function.

RSO resident space object.

RSOnar resident space object near-atmospheric edge reconnaissance.

SDA space domain awareness.

STC space traffic camera.

UTC Coordinated Universal Time.

ViCAS Virtual Constellation Analysis Simulator.

1 Chapter One: Introduction

The artificial satellite population around Earth is increasing rapidly due to human activity. Anti-satellite missile tests, orbital conjunctions, and debris due to satellite launch are factors that increase the number of objects. Earth orbit is a congested and contested environment leading to an increase in the probability of collision between orbiting objects. Analogies to the value of environmental protection on Earth, future of the Earth-centric space activity must be conducted safely and sustainably.

1.1 Space Domain Awareness (SDA)

SDA is the study and monitoring of objects in space to ensure that Earth orbit is safe, productive and accessible. SDA is an umbrella term for monitoring space assets, managing navigation and communication, custody operations, conjunction analysis, track launching and re-entering satellites, and intelligence gathering. SDA involves a complex set of requirements and constraints pertaining to satellite and ground systems operations, data collecting sensors, data fusion and analytics, conjunction and propagation analysis, and reporting and warning systems [1]. All systems play a key role in part of a chain of events that occur between data collection and performing maneuvers to assure the safety of an asset. An increase in research for space safety and sustainability in Earth orbit has been in the foreground recently. Many projections estimate a two to ten times increase in the total object count in Earth orbit by 2030 [2]. Due to the expected multiplicity of objects in this decade, the limited operating space is increasingly crowded which further complicates the requirements of existing space surveillance infrastructure.

1.1.1 Instruments for Surveillance and Data Collection

The Space Surveillance Network (SSN) provides a majority of the data used for SDA. The SSN detects, tracks, identifies and maintains a catalog of objects in Earth orbit. The publicly available catalog at *space-track.org* is a part of the United States Space Command's (USSPACECOM) commitment to information sharing to promote a safe and sustainable space environment. The public data is cited for use by the U.S. Department of Commerce for a civilian space traffic management system known as TrACSS. The data collection for this catalog is enabled with instruments on the ground and in space. The instruments vary in the method and mode they operate in. Ground-based instruments include tracking radar [3], telescopes[4] and satellite laser ranging. Space-based instruments include telescopes [5] and tracking radar or LiDAR [6] for close proximity operations. Some instrument operation modes are dedicated to SDA-only, whereas other collateral instruments may switch to fulfill non-SDA roles. The SSN currently maintains a track of over 40,000 resident space object (RSO) sized 10 cm and above [7]. There are also other instrument networks such as the Russian international scientific optical network (ISON) [8] for ground-based geostationary Earth orbit (GEO) surveillance, LeoLabs' network of radar stations, ExoAnalytic's optical ground-based instrument network [9] and European space agency's (ESA) space surveillance and tracking (SST) program. More details are provided in Chapter 2.

1.1.2 Problem Statement

In its current state, our SDA outcomes do not meet the desired objectives [10][1]. The key limitations of the SSN, as summarized by Foley [11], are instrument count, geographical distribution, capability and availability. Instruments currently used for surveillance are expensive to build, maintain, and replace. Due to their high cost, fewer are built. Some instruments may also not be available due to other non-SDA roles. Instrument capabilities and constraints also impact performance. At present, there are vast regions of Earth orbit that are considered blind spots for certain or all types of instruments. Ground-based optical sensors are limited by local weather and daylight hours. Ground-based active phased array radars are capable of high-accuracy multi-object tracking, but have limited range due to available transmission power. Radar's are also generally not dedicated to RSO detection and tracking [12], as the technology is more commonly implemented

for missile-tracking. However, these limitations are being addressed with newer commercial tracking stations coming online dedicated to SDA.

Missions like Space-Based Visible (SBV) [13] [14], Sapphire [15], and NEOSSat [5] have successfully demonstrated how space-based instruments can contribute to our awareness. The progressive capabilities and technologies demonstrated on these missions highlight the need for more space-based space surveillance instruments. However, many space-based instrument designs follow the high-cost, single mission, high-resolution individual object tracking approach adopted by most ground-based instruments, which limits their scalability. This approach requires mission-specific integration of target and tasking operations, communications and ground-link, mission design, test, launch and maintenance. Individual mission costs can range from 10s to 100s of millions of dollars. In addition, these instruments are often tasked to track RSOs in low Earth orbit (LEO) up to Geostationary Earth orbit (GEO), increasing the scope mission requirements. Active tracking of various orbital regimes from space-based platforms adds to the mission design complexity, eventually leading to compromises or cost overruns. Active tracking of both GEO and LEO targets from LEO leads to contrasting sensor requirements with regards to slew rates, field of view, aperture size and scheduling. The highly variable aspects of range requirements, angular velocities, RSO shape and illumination, and observational geometry forces mission designs to converge on a template solution of narrow field of view, large aperture, active tracking and dedicated mission [5]. Tracking objects in LEO is then defined by satellite design constraints regarding slew rate, viewing opportunities, tasking limitations and reliability of observations. Optics-based LEO to LEO surveillance remains a challenge in the industry [16], and is an unlikely candidate for cost savings when considering active tracking. Space-based surveillance instrument costs have been decreasing over time, in part due to increased commercial research in miniaturization technologies. However, the approach to track individual satellites, at high accuracy and large distances often does not directly address the wide-scope objectives of SDA [17]. Instead, these missions are dedicated to specific asset management, which is of key interest to the mission sponsors. This approach is referred to as qualitative awareness.

1.1.3 Future of Space Domain Awareness and Requirements

Current and future SDA objectives have a broader scope of requirements than in the past. Previously conducted and expected future experiments such as anti-satellite missile tests (ASAT), rendezvous and proximity operations (RPO), parasitic satellites, human spaceflight and space station operations, active and passive orbital maneuvering, launch and re-entry operations and all other potential Earth-centric space industry applications require a new set of safety requirements. SDA and commercial space traffic management (STM) are near real-time continuous operations that require constant effort, in part due to the chaotic weather-like nature of orbiting bodies. Factors such as solar radiation pressure, resident space object (RSO) attitude, orbital maneuvers, atmospheric density fluctuation [18] and outgassing drastically alter the orbit from propagation models. Fundamentally, the only way to have a precise, real-time, and holistic awareness of all objects in Earth orbit is by establishing a network to continuously monitor it. Expanding scopes of research in the areas of satellite maneuver detection [19], debris tracking and removal [20], atmospheric effects on general perturbations [21], astronomical data corruption [22], orbital decay rates, and radio frequency interference suggest that these events are far more likely to occur in the near future, in part due to increased commercial activity. Policy and policing solutions also play an important role in enabling sustainable expansion of the space industry without exacerbating the space debris issue. However, the adequacy of our awareness is limited by our ability to collect qualitative and quantitative data of the events in orbit. We may have solved the qualitative aspect of data collection, but new approaches to obtain quantitative surveillance data are required, with novel instrument concepts [11].

In light of establishing new low-cost sensor requirements, space-based SDA instruments need to be scalable, fill existing surveillance gaps (LEO to LEO), complement existing ground infrastructure, automated and low-cost. Instrument and instrument networks need to provide information accurate enough to be useful in making future conjunction analysis with acceptable confidence scores. Conjunction analysis refers to the astrometric study of when and where two orbiting objects may collide and are dependent on the dynamic confidence of measurements available for each. Accuracy and contribution assessment of instruments can be performed via standardization practices established for data collection and sharing services such as the unified data library (UDL)[23], EU

SST (European Union Space Surveillance and Tracking) support framework [24] and commercial data fusion services [25]. Defined below are some of the considered accuracy metrics important to this research.

Angular resolution refers to the smallest angle that can be resolved by the camera. This is typically expressed in terms of arcseconds, and is determined by factors such as the size of the camera's aperture and the wavelength of the light being detected. The smaller the angular resolution, the more precise the camera's measurements of an object's position will be. Pointing stability refers to the camera's ability to maintain a fixed pointing direction over time. Any small variations in the pointing direction can cause significant errors in positional measurements, especially over long observation times. Pointing stability is typically expressed in terms of the camera's jitter, or the root mean square (RMS) deviation of the pointing direction over a given period of time. In addition to angular resolution and pointing stability, other factors can also affect positional accuracy, such as the camera's calibration accuracy, the quality of the data processing algorithms used, and the amount of noise in the data. Overall, achieving high positional accuracy in space-based space surveillance requires careful attention to all of these factors.

Detection, characterization and classification studies are key to assess instrument and network viability [26] for evaluating space missions from a sustainability perspective. Instruments also have to be geographically distributed to provide a larger coverage volume of Earth orbit, and have improved satellite re-visit times. These requirements are necessary for transitioning SDA from a task-based service to a search-based service [17]. For low-cost and scalability, an instrument's approach to data collection should involve minimal manufacturing and operational cost [27]. Scalability and automation are key technologies for managing these requirements, both in a limited and global implementation [28]. Finally, the instrument must be dedicated to SDA objectives or must collect enough data in a non-dedicated mode to meet major SDA objectives. These are some of the key requirements of an instrument that addresses the current gaps of our SDA [11].

1.2 Space Traffic Camera and Network

This dissertation defines and evaluates the space traffic camera (STC) as an opportunistic space surveillance sensor to address the gaps of current SDA infrastructure, specifically in LEO. In large

numbers, a virtual network of automated sensors can provide the data necessary towards a real-time awareness of the activities in space. The camera refers to the combination of a telescopic lens and an electronic imaging instrument mounted on a host satellite. The STC works on the principles of photonics, where light emitted by the Sun is reflected off an RSO and is collected by a camera to produce an image. A very similar kind of image is produced by a star tracker.

A star tracker is an attitude determination instrument commonly mounted on satellites as part of the attitude determination and control system. A star tracker takes periodic images of stars, known as star-field images, and uses a catalog search algorithm to determine the satellites attitude based on the star's identified in the image. A star tracker pointed towards any direction without obstructions, and with a large enough aperture size and field of view, must be able to detect enough stars to provide accurate attitude estimates.

On a star-field image, even the brightest stars appear as a point source of light due to the vast distances light travels. Equivalently, an RSO also appears as a point source of light despite its small size and relatively short range. RSO and stars often appear indistinguishable in a star field image, and examples of this are visible in images collected by the fast auroral imager (FAI) [29] on-board the CASSIOPE spacecraft [30]. Previous works demonstrating detection are explored in Chapter 2 and a detailed analytics of a STC network are provided in Chapter 3. For comparison, Table 1.1 below summarizes some of the FAI specifications adopted for defining the STC [31] [30].

Table 1.1: Fast Auroral Imager Specifications

Aperture diameter	1.7 cm
Field of view	26°
Focal length	6.9 cm
Exposure time	0.1 s

Conclusions from [32] suggest that RSO detections are possible using FAI images and commercial star trackers. Considering this conclusion, paired with the fact that there are several thousand star trackers in LEO already, there is significant data collection capacity in place. Thousands of star trackers in orbit currently may be filtering RSO detections to improve star tracking and identifica-

tion process on a daily basis. If centralized effectively, the images or data collected and downlinked by these star trackers can prove effective in development of novel algorithms and research objectives, which otherwise require dedicated launch efforts. Chapter 4 will address adaptable methods of centralization and efficient data processing frameworks for varying star tracker specifications. Chapter 5 will discuss implementation.

1.2.1 Space Traffic Camera and Scope of Definition

Figure 1.1 below provides a visual illustration of various types of STC definitions as a novel contribution of this research. The highlighted regions identify the scope of work in various interpretations of the STC. A software-only solution can be implemented and validated on operational satellites already in orbit. These solutions includes direct image data downlink with or without processing and compression. A payload solution refers to the customized camera, processor and processing software as an embedded solution. The dual-purpose payload implementation refers to providing the STC as a dedicated hosted payload on-board a spacecraft. The dedicated hosted payload would include camera, processor, and processing algorithms for RSO detections and for attitude determination. Finally, the standalone mission exemplified by previously launched missions focused on passive optics for SDA. All of these interpretations are considered valid as a space traffic camera, and the data collected by each is centralized on the ground.

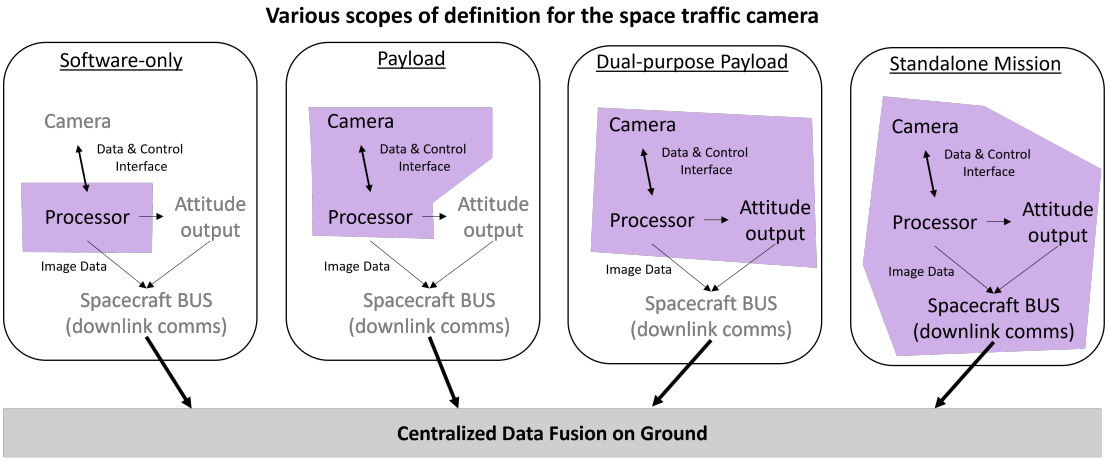

Figure 1.1: Space traffic camera and range of definitions

The STC is a scalable instrument that is constrained by the spacecraft that hosts it, in context

of resource requirements such as power, bandwidth, mass and volume. The definition considered in the research will approximate the FAI and commercial star tracker specifications. The STC's primary instrument is a camera with a field of view between 10 and 26°, an aperture size ranging between 2 and 15 cm, in a nanosatellite mountable form. A nanosatellite is a mass-class of satellites defined loosely below 10 kilograms. The STC is suitable as a potential primary or secondary payload on a nanosatellite. Nanosatellite payload power (up to 20 Watts), size (up to 30 cm side), and mass constraints further define the scope of the STC payload. The STC, defined as fully operational in passive mode, may also involve active RSO tracking using an existing attitude control system. However, there are previous works described in Chapter 2 on active implementation and will be considered out of scope for this research. This research also recognizes that launching large number of satellites for the sole purpose of tracking RSO may exacerbate the space debris issue, and will only consider STC as a virtual constellation. The STC may also be operated in SDA-only or mixed-use roles, as being a multipurpose payload would benefit the likelihood of adoption. One such obvious role is the concept of a dual-purpose star tracker [33].

Nanosatellites don't often carry star trackers unless the mission requires a high accuracy requirement; in this case accuracies of 5 degrees are considered high. However, more and more payloads are eligible for miniaturization to enable deployment on nanosatellites and this constraints the design of the STC to remain low-cost and power efficient. The dual-purpose functionality would certainly have no degradation of the attitude determination accuracy as the same algorithms can be implemented in a modular fashion. The only comparable metric that might differ in performance is star centroiding, however in most star tracker implementations the centroiding is primarily limited by the instantaneous field of view of the image.

A space traffic camera network (STC network) is defined as a virtual constellation of all satellites hosting one or many STC. A virtual constellation is a group of satellites, that may otherwise have unrelated missions, where each satellite acts as common node in a virtual network [34]. For the STC network, each hosted camera acts as a data collecting node contributing to SDA. Similar concepts using a network of ground-based small telescopes [28] and multi-site observation platforms [35] have been studied. A distributed network of ground-based small telescopes are certainly great candidates for contributing sensors, but this research will only focus on the space-based

STC. However, the methodologies developed for the STC are observer agnostic, meaning they do not differentiate processes by the location of the observer.

1.2.2 Benefits, Challenges and Constraints of the Space Traffic Camera

The chosen nanosatellite form factor increases the potential pool of future satellites that can host the STC, allowing for ease of scalability and reducing the cost per instrument. This is a unique requirement established for this research. Using existing commercial off the shelf (COTS) components and subsystems, the STC can draw design choices from star trackers to minimize development costs, easily integrate into existing satellite bus designs and operational practices. A similar approach can be adopted for data processing as an embedded solution. The STC payload concept relies on flight-proven technology in satellite-mounted optical sensors, processing algorithms, processors, data handling and integration technologies. Further details are discussed in Chapter 5. Proof of concept, or a technology demonstration, for the STC is achievable without the need for a dedicated orbital launch.

As part of the Flights and Fieldwork for the Advancement of Science and Technology (FAST) funding initiative from the Canadian Space Agency (CSA), RSOnar had been selected as one of the mission proposals to demonstrate the dual-purpose star tracker functionality on-board a stratospheric balloon launch by the French National Centre for Space Studies (CNES) from Timmins, Ontario. The payload, designed by a team of York University students, contained a camera that has detected LEO satellites from 37 kilometers above sea level. The payload flew in the early morning hours of 22^{nd} August 2022, and the analysis of this data is presented in Chapter 5.

Image processing of star field images from satellites have already demonstrated the feasibility of a single STC sensor to detect RSO [33]. An early feasibility on RSO detection from FAI images concluded that 1 m and 10 m sized objects are detectable at 1,000 km and 10,000 km, respectively [32]. The STC network feasibility can also be demonstrated, in part, with bulk processing of available star field images from in-orbit satellites. Although no such data set exists today, this research aims to be a motivation to aggregate a real star field image benchmark data set aimed at SDA from satellite mounted optical instruments. Some applications of such a data set go beyond just astrometric analysis, as RSO characterization of shape and attitude has also been demonstrated in previous research [36]. Some of these techniques use light curve analysis from images captured

by a ground-based telescope to characterize shape and spin rate of the RSO [37]. Research into multi-spectral filters for better characterization studies have also been discussed in the past [38]. Several challenges remain in this research field, and the collection of a large data set will certainly help advance the research to develop novel applications.

Satellites hosting the STC also require ground communications to report on detected RSO on a regular basis. At volume, digital images occupy large data bandwidth and data storage, which may be cost inefficient. To minimize the amount of data each STC payload produces, data collection duty cycle can be optimized as per the host satellite's mission profile. As discussed in Chapters 4 and 5, image processing and image compression offer sustainable alternatives. The hardware and software necessary for data compression is described as enabling research contributions for the STC and STC network concept.

The benefits of distributed volume data collection with the STC network is proportional to the accuracy of an individual STC sensor and the total population of STC nodes aggregated. Fundamental optical sensor design and engineering specifications determine the accuracy limitations of an individual STC sensor. The camera aperture size and exposure time relates to making consistently high signal to noise ratio measurements for detection accuracy. The frame capture rate affects the temporal resolution of measurements for astrometry and photometry. The star identification algorithm and search algorithm directly impact the attitude estimation. The field of view determines the instantaneous field of view of each pixel, which also affects the attitude estimation and astrometry measurements. More details are discussed in Chapter 5. Chapter 3 studies ideal viewing geometry possible with host satellite orbits, mounting configurations, instrument specifications and constellations available which have an impact on the number, quality and consistency of observations. Chapter 5 describes benefits of hardware accelerators to enable data collection and improvements in accuracy possible via multi-site observations. Chapter 5 also analyzes the data collected from the suborbital resident space object near-atmospheric edge reconnaissance (RSOnar) mission. The benefit of having thousands of STC sensors is the opportunity to observe a common RSO from two different STC sensors. The position and velocity estimation of one STC sensor may be inaccurate, but the combination of multiple observers improves accuracy. However, the number of STC

sensors required to provide a meaningful perspective on SDA may be quite large, and remains an unknown challenge. Further research and experimental missions are required to advance the state of this technology, and this dissertation is a contribution in that direction.

In summary, some of the challenges ahead include STC adoption, resource requirement uncertainties, ease of design duplicability for camera and limits of RSO characterization. The research presented in this dissertation intends to resolve these challenges. Some of the expected benefits are system robustness and built-in redundancy, in-orbit updates, STC size and performance quantization, data downlink optimization and novel viewing opportunities.

1.3 Thesis Objectives

The primary objective of this research is to examine the viability of the STC as a practical space-based space surveillance sensor in a novel implementation. This research demonstrates that it is possible to achieve a near real-time holistic space domain awareness with a network of decentralized and cost effective payloads. The dissertation also demonstrates how the STC network can contribute to space surveillance in a novel capacity. The research is subdivided into three categories of work:

- Examine virtual networks of distributed STC nodes and the potential of their aggregate capabilities to SDA
- Design an adaptable image processing and compression framework for any STC node
- Develop and test a concept of operations for the STC and discuss payload designs

1.3.1 SDA Data Collection from a Network of small-aperture Cameras

The first objective is to define requirements for the STC as part of a data collecting node in a network. Various types of virtual constellations, camera hardware specifications, and camera mounting directions impact the number of RSO detections, RSO detection duration and sky coverage possible. Chapter 3 describes various configurations in which the data collection, in large quantities, is optimized using the hosted payload concept. The objective is to design a simulator that can model satellites in Earth orbit to study architectures of virtual constellations best suited for SDA. Discussion is provided to show why a unique simulator was designed, as replicated by

other researchers in the field. The Virtual Constellation Analysis Simulator (ViCAS) is designed to simulate the optical telescope, image sensor, mounting direction, host satellite orbit, orbit of all other simulated RSO with or without the STC, to understand optimal virtual constellation designs, and to derive STC requirements using the principles of photometry and astrometry. Although tools that can achieve the desired objectives exist, they are not optimized or designed for the scale of simulation studied here.

1.3.2 Image Processing Framework as a Scalable Solution

The second objective is to develop the data processing framework for the STC. Chapter 4 outlines an image processing framework tailored to achieve STC requirements derived in chapter 3. RSOnet is developed to exemplify an image processing algorithm based on artificial intelligence (AI) to detect, track, characterize and classify RSO from other RSO, Star and noise sources. RSOnet also compresses the image data at high ratios, reducing the data management requirements. The design methodology chosen is adaptable to hardware platforms like embedded system on chip (SOC) design, with performance optimization a key focus to increase adoption rate. Several image processing algorithms exist in this research space that will be discussed, however none vertically integrate for the virtual constellation or hosted payload method. These requirements change the design requirements, especially when referring to data downlink and compression.

1.3.3 SDA Payload Concept and Experimentation for Validation of Methodology

The third objective is to study the practicality of implementing the STC. Chapter 5 discusses the results of processing images from various sources, including the RSOnar sub-orbital payload. Chapter 5 also discusses payload requirements, and analyzes the accuracy and practicality of contribution to SDA, demonstrates experimental results and highlights areas where further research is required.

2 Chapter Two: Background

This chapter emphasized the notable research done in the field of space surveillance. The chapter includes a discussion of optical observation strategies, sensor capabilities and justifications for key research decisions.

2.1 Established Research and Practices for Space Surveillance

Remote sensing for space surveillance is primarily carried out using radar and optical instruments. Active radar is most commonly adopted terrestrially, where a transmitter generates and directs high power radar signals towards LEO. Receivers, typically large gain antennas, are placed near the transmitter site to collect faint signal pulses reflected off RSO. The transmitted frequency, power, pulse and geographical location are chosen according to the target RSO population and size, quality of observation, weather-based signal impedance and ease of signal detection and processing. Radar signal wavelength also determines the size of the object detectable. LeoLabs [39] operates S-band terrestrial radars, with signal wavelengths between 7.5 and 15 cm, which can detect RSOs less than 10 cm in size in LEO. Radar instruments are geographically distributed in a sparse manner and their surveillance range is limited by transmission signal power and receiver antenna size. Power, size and mass constraints also limit their application as a space-based instrument. One notable example is the Ku-band space based radar (SBR) [40]. Optical observations are divided into passive and active methods; active methods include laser ranging and LIDAR and passive methods include telescopes and smaller cameras. Active methods for large scale space surveillance is preferred terrestrially, however individual tracking for rendezvous and proximity operations, like docking to the International Space Station (ISS), often rely on LIDAR or laser ranging. The terrestrial constraint for scale surveillance using active optical instrumentation is

also due to available signal transmit power and receiver optical aperture size and mass. However, this dissertation is focused on increasing surveillance instrument count by utilizing the benefits of passive optics. The key advantage of passive optical surveillance is that the maximum detectable range of an RSO is proportional to the square of the distance, as opposed to distance to the fourth power for active surveillance. This advantage enables lower cost and complexity instrumentation design for equivalent performance.

Passive optical observations rely on the RSO being illuminated by the Sun. The brightness of the illuminated RSO is dependent on the viewing geometry of the Sun, RSO and the observer. Brightness of the Moon and Earth reflecting off the RSO are negligible; therefore not considered in this research. The brightness of the full moon is 14 magnitudes below the brightness of the sun and Earth is 9 magnitudes below, making it a challenge for small aperture cameras to differentiate reflected light from background noise. The process of an RSO detection is considered in two steps. First, the visual magnitude of the RSO is considered to compute how much of the RSO-reflected light is captured by the camera. Second, an image processing algorithm is adopted to process the detection.

The visual magnitude, or brightness at a distance, of an RSO depends on the size, shape, albedo, distance, and solar phase angle. Equation 2.1 below describes this relationship. Each RSO is modeled as a Lambertian sphere [41] [42], having a diffusive reflective property:

$$F_{diff} = \frac{2\,a\,r_{RSO}^2(sin(\phi)+(\pi-\phi)cos(\phi))}{3\pi D^2} \tag{2.1}$$

In equation 2.1, a is the albedo, r_{RSO} is the radius of the RSO, ϕ is the solar phase angle and D is the distance between the observer and the RSO. This equation determines the fraction of incident solar flux reflected by the RSO as measured from a distance D. Equation 2.2 below defines how the incident solar flux of the RSO is used to calculate the visual magnitude of the RSO, m_{RSO}, from an observer:

$$m_{RSO} = -26.74 - 2.5\,log(F_{diff}) \tag{2.2}$$

where -26.74 is the visual magnitude of the Sun.

The amount of light reflected off the RSO captured by a camera at a defined distance depends as follows. Research conducted in previous efforts [43] [44] [45] describes the relationship between aperture size, quantum efficiency of the sensor, and exposure time in their effect on the signal to noise ratio (SNR). First, the brightness of the RSO, B_{RSO}, is computed as per Equation 2.3:

$$B_{RSO} = I_{RSO} A\, e\, Q_{eff} \tag{2.3}$$

where I_{RSO} is the irradiance of the RSO, A is the surface area of the aperture, e is exposure time and Q_{eff} is the quantum efficiency of the image sensor. The FAI specifications are used for exposure time and quantum efficiency. Next, the SNR is calculated by estimating brightness of the background noise B_{noise} and the image sensor's read noise B_{rd}. These values are calibrated according to the FAI. Equation 2.4 below illustrates how SNR is computed [45]:

$$SNR = \frac{B_{RSO}}{\sqrt{B_{noise} + B_{rd}^2}} \tag{2.4}$$

For computing the irradiance of the RSO in Equation 2.3, Equation 2.5 below is used [44]:

$$I_{RSO} = 5.6 \times 10^{10 - 0.4 m_{RSO}} \tag{2.5}$$

where m_{RSO} is magnitude of the RSO from Equation 2.2. Using Equations 2.1 through 2.5, the SNR of all RSO from an observing STC is computed. The solar phase angle for a valuable RSO detection is 30 degrees or less. The value is derived by the SNR and duration of detection which determines the quality of characterization that can be performed [46]. The required solar phase angle constraint is achieved in vastly different scenarios for ground and space based cameras. For ground-based observations of LEO RSO, the ideal observation time is immediately after dusk and before dawn. Based on the orbital trajectory of an RSO and a fixed location on the ground, the sky brightness and phase angle are lowest during these times. A few hours after dusk and before dawn, the Earth's shadow prevents the sunlight from directly reaching the RSO, making it too faint to detect. This phenomenon is illustrated in Figure 2.1 below. Sunlight illuminates RSO 1, 2 and 3 for observers 1 and 2 to detect. Observer 1 is situated at a fixed geographical location,

whereas observer 2 is a space-based observer. Although Figure 2.1 is not to scale, it illustrates the smaller solar phase angles achievable with a space-based observer. In fact, a phase angle of 0 is unachievable with a ground based observer at night for a LEO RSO. These are the fundamental constraints that a passive optical surveillance instrument, relying on solar illumination of RSO, needs to operate under. The dotted circular lines represent the orbits of the RSO and observer, whereas the green and blue vectors represent the path light travels in context of surveillance.

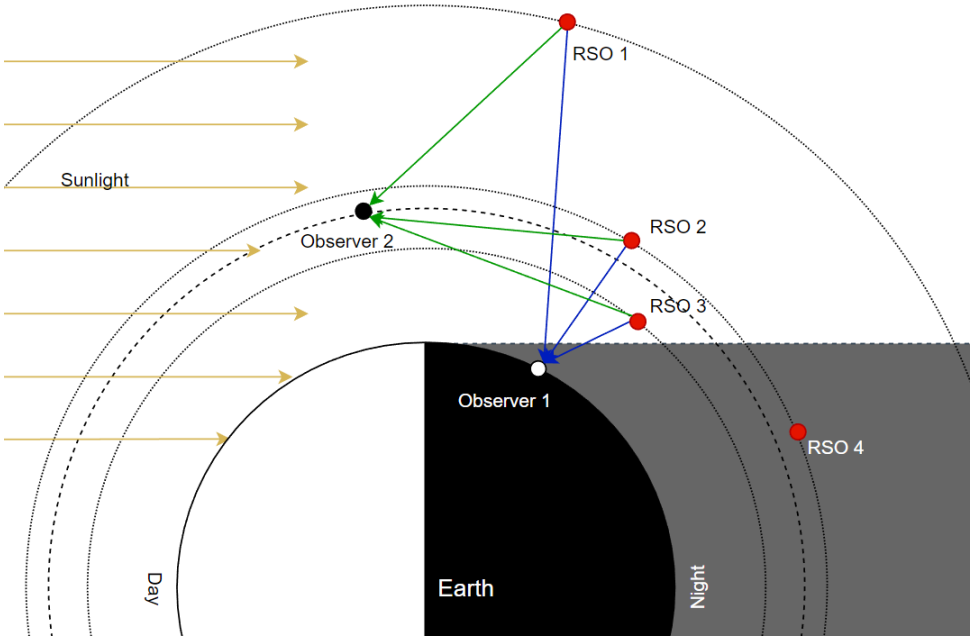

Figure 2.1: Idealized illustration of passive optical surveillance from ground and space-based observers

The time duration of detectability further depends on the latitude of the observation site and the RSO orbit altitude. The further the observation site is away from the Equator, the longer the period of observation. Likewise, the larger the orbital altitude, the longer the period of observation. Observation times near the equator are approximately 30 minutes and exponentially increase to 6 months near the poles depending on time and date of the year. Geostationary Earth orbit (GEO) is situated at an altitude of 35,786 km and also gets eclipsed by the Earth's shadow. However, the percentage of a GEO RSO orbit under eclipse is significantly smaller than for LEO RSO, which makes passive GEO observations from ground very valuable as demonstrated by ExoAnalytic's optical ground telescope network [47].

Space-based passive optics offers unique observation opportunities unconstrained by Earth's

weather and atmosphere. As highlighted in previous works [48] [49], a 3 dimensional viewing opportunity requires geographical spread of the remote sensing instrument, which is difficult to achieve terrestrially. The dimensionality of observation for better characterization of the 3D outline of a satellite requires visibility from all sides. Such a perspective is only achievable when observers view different sides of the RSO, which is unlikely from ground observations. The 3D shape and attitude of the RSO interacting with the effects of space weather directly impact the orbital trajectory with forces that are not accurately accounted for in public catalogs.

2.2 Passive Optical Surveillance Methodologies

Passive optical surveillance refers to a surveillance strategy which relies on collecting reflected sunlight as a remote sensing measurement.

2.2.1 Technology Gaps and Limitations

The volumetric coverage of the utilized Earth orbits using SSN and like-sensors is a known limitation. The exact coverage value is unknown, but at any given moment in time only a fraction of RSOs are detectable by any instrument network. Low Earth orbit (LEO) satellites orbit approximately once every 100 minutes, hence orbit Earth more than 14 times in a day. LEO refers to satellite orbit height from the surface of the Earth between 100 and 2000 km, and is one of the most populated regions in Earth orbit. Orbits are known to passively vary and drift over time due to factors such as nodal precession [50], atmospheric expansion and contraction, and orbit eccentricity and period [48]. The complexity of orbital variations over time, which falls into the chaos theory branch of mathematics [51], are modeled analytically and propagated using the theory of astrodynamics. Due to the complexity of the system, any analytical model for propagating orbits into the future is imperfect and tends to lose accuracy over time [52]. Simplified general perturbations #4 (SGP4) is a widely popular orbital propagator with an accuracy of tens of kilometers for up to 3 days [53]. The accuracy of the propagator model and the sensor making the detection have a direct impact on our ability to meet SDA objectives [54]. There are two acceptable standards to define a high accuracy measurement and propagation, and they are separated by their application. The measurement and propagation accuracy for commercial applications, as standardized and accepted

by the U.S. Department of Commerce, is considered in this research like SGP4. The improved proprietary propagator out of scope is defined and standardized by the U.S. Department of Defense. The number of measurements and their accuracies have a direct correlation on the performance of the propagator, especially when satellite shape and attitude are used as parameters. Due to the limited number and coverage of SSN sensors, each RSO may not require a high re-detection rate. When an RSO is re-detected and matched to a previous detection [55], the propagation error is calculated and corresponding propagator model corrections are applied [56]. Over time, a highly accurate orbital propagator can be developed using the orbit residuals [57]. This technique places emphasis on a sensor to collect target observations at high spatio-temporal resolution, but not directly on revisit times [58]. A significant portion of SSN sensors are based on inter-continental ballistic missile (ICBM) tracking technology, which requires high tracking accuracy for effective countermeasures over a fixed geographical location. Naturally, several non-dedicated SSN sensors prioritize high accuracy tracking of individual or small group of RSO. This approach, of sparse but accurate tracking combined with orbital propagators, has proven qualitatively sufficient for the first 65 years of space surveillance needs. However, with an increasing satellite population and more complex SDA requirements, it is unclear if the current surveillance strategy is a cost-effective and sustainable method for scaling data collection to keep up with future launches [59].

Emerging and continually expanding commercial capabilities providing optical coverage in GEO with ExoAnalytic Solutions and radar coverage in LEO with LeoLabs has demonstrated the industry's demand for more surveillance. Large scale commercial optical capabilities for LEO surveillance are limited to ground-based solutions like Slingshot Aerospace [60]. Slingshot global sensor network (SGSN) operates over 20 optical sites globally with remote tasking ability to track target RSO. Some of these optical sites also operate during the day to improve sensor utilization. Sensor utilization and multiplicity is a common theme not only in the SDA industry, but also for the general advancement of spacecraft borne technologies. Contrasting with other approaches of on-site sensor multiplicity [61] [62], Slingshot aims to improve their instrument by implementing ultra-wide field of view cameras, also known as all-sky cameras. All-sky cameras have fish-eye lenses capable of 180 degree field of view, eliminating the need for robotic task-based tracking. Tasking and scheduling are reduced to a software implementation which describes a search-based service. All-sky photometric data on RSO are collected in bulk, and post processed for photometric

and astrometric characterization [63]. However, the all-sky optical systems are not exempt from local weather and cannot operate in a sky brighter than astronomical twilight [60]. Astronomical twilight is used to define as a period of sky brightness during sunrise or sunset where the Sun is between 12 and 18 degrees below the horizon. Given the wide field of view of the instrument, stray light from road vehicles, towns and planes can cause data corruption, and therefore need to be situated in remote locations. Additional challenges include atmospheric distortion [49], detection sensitivity [60] instrument design complexity and photometric and astrometric characterization [64]. Most techniques also utilize monochromatic sensors, as does this research, which reduces the dimensionality of data collected per observation. Efforts to collect multi-spectral or hyper-spectral observational data, from space-based instruments are also a noted research gap [65]. All existing commercial space surveillance entities have invested in expanding capabilities to address the expected increase in demand and reduce gaps.

2.2.2 Demonstrated Surveillance Methods

Passive optics have previously demonstrated RSO detections from ground and space. Fundamentally, the constraint on the detection sensitivity is determined by the diameter of the aperture. In practice however, the problem is more nuanced. To detect an RSO without previously knowing its orbit, the optical sensor's field of view (FOV) has to overlap with the RSO orbit. The tracking hardware of the optical sensor has to maintain the RSO within the FOV for the duration of the observation, which can require high slew rates when observing LEO RSO from ground. Weather, daylight and geographical constraints can further limit valuable operation time. Efforts to create a mobile telescope to circumnavigate these limitations have been attempted before [66]. The mobile telescope (2.8° FOV) achieved a 13.5 magnitude detection sensitivity on objects 5 cm in size orbiting around 300 km in altitude. Another approach adopted in literature is the setup of an array of telescopes which can collectively observe large areas of the sky [62] [67]. This approach is an improvement compared to a single large telescope, however it suffers from similar limitations prone to ground-based optics. Multi-objective design approach of using small telescopes already distributed around the world are also considered in other research. A thorough analysis is presented on the benefits, applicability and novel contributions telescopes can make to SDA [36].

The space-based surveillance approach discussed in previous efforts are similar to the approach

considered in this research. Du considers a smaller constellation of larger telescopes for active maneuvering surveillance strategy [16]. Sanchez explores such a pointing strategy beneficial for GEO surveillance [58]. Hertwig provides a description for key benefits of a search-based system, which is considered the least-utilized in the industry [17]. Peters analyzes how a sensor network is integrated and discusses the observation benefits of this network [68]. Yanagisawa simulates the results of many non-tracking narrow field of view telescopes co-located for ground-based optical surveillance [69]. Other works also discuss space-based telescopes and how they are utilized for initial orbit determination and orbit refinement analysis [70] [71]. This includes a constellation of satellites equipped with Sapphire's optical instrument [15]. The research considers various constellation sizes and types ranging from 1 - 24 satellites and concludes that constellation scaling is a significant performance factor. The methodology adopted in this research attempts to demonstrate scaling effects using cameras like the star tracker. A similar research effort examines the scope of space-based sensor management for space surveillance [72]. The research considers a proximity-based filter to evaluate detectability of RSO at scale. This dissertation evaluates surveillance capabilities using similar metrics by constraining detectability to the STC instrument capability.

2.3 Data Processing and Instrumentation for SDA

2.3.1 Dual Purpose Star Tracker Concept

Clemens [73] performed a study to determine the feasibility of RSO detections from commercial off the shelf (COTS) star tracker cameras. Clemens' preliminary results, using an optical image simulator found that a baseline of 1 to 10 RSO detections per day are achievable. Clemens' research was verified and validated using the Fast Auroral Imager (FAI) on the Canadian satellite Cassiope. Compared to the 0.8° FOV of NEOSSat, the FAI has a 26 ° FOV, and COTS star trackers range between 8° and 45° depending on the manufacturer and application. Star trackers generally have a wide FOV, small aperture and capture images with a short exposure time to capture light from many bright stars and analyze their motion on the image plane. The FAI [29] is a similarly tasked instrument, with a comparable aperture of 17 mm, and is also considered a primary data

source for this dissertation. In Chapter 4, RSOnet is presented as a star field image processing framework for the dual purpose star tracker functionality. In addition to the FAI, data for validating RSOnet was also sourced from the space-based optical image simulator (SBOIS) developed by Clark [74]. The validation data obtained from real FAI images are labeled manually and not used for training. Part of the labeling is done using the *Astrometry.net* plate-solver [75]. Labeled training and validation data obtained from simulated SBOIS images, of the matching FAI scenario, are used both for training and validation.

2.3.2 Relevant Work for Image Processing

Research by Denver [76] studied the sensitivity performance of a star tracker for debris detection. Fundamentally, detection of RSO using satellite-mounted camera improves based on two key parameters, aperture size and object detection sensitivity of the image processing algorithm. The aperture size determines the amount of light that enters the optical tube. The sensitivity of the image processing algorithm relies on differentiating between an object's light in contrast to its background. For RSO detection, Denver estimates limiting visual magnitudes of 7-9 is possible with star trackers and Clemens estimates a limiting visual magnitude of 8.7. Building on the detection sensitivity, RSOnet is designed as a framework to optimize for object detection, characterization and classification. An object in RSOnet includes physical and virtual objects in an image. Physical objects are celestial objects and Earth orbiting satellites and virtual objects are hot pixels and shot noise. In context of typical operation mode in a small aperture star tracker providing attitude updates at rates of up to 5 Hz, the objects detected can be classified spatio-temporally. The motion and brightness, of each object over time is key to classifying the object class. Badura's [77] implementation of convolutional neural network (CNN) demonstrates how recent advances in artificial intelligence techniques can be used for SDA applications, by classifying objects and their attitude status with light curves from images. It is also clear that RSO position and velocity can be estimated [76] [78]. The accuracy of the RSO position and velocity estimation, which is likely unreliable using just one star tracker, can be improved using a network of star trackers and will be addressed in future works. Other object classification techniques such as support vector machines (SVMs) are also popular in astronomical image processing, for both classification and regression applications [79]. Before artificial intelligence and machine learning

techniques, star detection and centroiding was commonly performed using Gaussian fitting techniques [80]. In this method, manually designed variations of Gaussian distribution functions were used as filters, and the filter activations were used by a generalized model function to predict a detection probability and perform regression-like analysis [81]. In this research, a blend of Gaussian distribution functions and point spread function (PSF) are used to generate training data, a CNN backbone is trained and validated on a mixture of real and simulated images. A similar effort is described in previous works where a CNN is used to model point spread function for astronomical applications[82]. CNN approaches for wide field of view cameras have also been explored using existing ResNet architecture, referred to as RetinaNet [83], and YOLO-based object detection [84] and YOLO-based spatio-temporal tracking [85], but mostly for GEO observations. The CNN algorithm presented in this research will merge the detection with a temporal classification algorithm for LEO surveillance, which is a novel approach.

CNN was preferred over the SVM classifier for two reasons. Firstly, CNNs offer shorter inference times during deployment when compared to SVMs, making it easier to achieve real-time results. This is crucial to achieve the desired 5 Hz frame rate as each image frame may consist of well over 200 objects. Secondly, the ratio of computational power during training to deployment is greater than 1, which determines the choice of model design. CNNs are a preferred in this scenario as the embedded FPGA firmware development for the RSOnar mission can be standardized and development time can be reduced. CNNs can effectively extract features from images, such as stars, RSO, and background noise. The convolutional layers in CNNs can detect and extract the local patterns and features from the images, while the pooling layers can capture the spatial relationships between them. This enables the model to make regional and global predictions, which is crucial for wide field of view imagery. Once features are extracted from the images, CNNs can be trained to characterize the detected objects. Wide field of view images are often affected by various types of noise, including electronic noise, shot noise, lens flare and image aberrations. CNNs can be trained to denoise the images beyond traditional astronomical techniques, thereby improving the signal-to-noise ratio and enabling better detection of faint objects. Deployed models are also able to learn and adapt to dynamic noise variations over longer time frames. This robustness can improve the reliability and accuracy of star identification and attitude determination, even in challenging imaging conditions. CNNs can be trained to accurately identify stars in the images

captured by the star trackers, even in low light conditions or with high levels of noise, thereby improving the accuracy of spacecraft attitude determination.

A key step after processing detections is multi-object tracking (MOT). In star field images, multiple point source objects have varying angular velocities, which is a key feature for classification. The FAI images have a 0.1 second exposure, avoiding a scenario where a moving point source object creates a streak. Therefore, sequenced over many image frames, an object can be tracked and differentiated using MOT approach. Techniques such as image stacking to reduce noise and Gaussian parametrization to determine streak characteristics and object tracking have been studied in the past [86] [87] and also utilized for faint satellites in geostationary Earth orbit [88]. These techniques are not suitable for wide star field images, as active tracking, ranging and long exposure images are not in the scope of this research. Instead, tracking and classification techniques like re-identification [89] and shortest path are considered [90].

2.3.3 SDA Characterization Methodology

RSOnet combines photometric and astrometric feature extraction of objects, which are beneficial in estimating RSO attitude and spin rate [37] [91], RSO identification [92] [93], host satellite attitude determination and potentially more applications. All such applications require a large labeled and continually updated training data set of star field images, something not currently available for public research. RSOnet provides a framework for a scalable and portable tool for star field image processing and data collection. Examples of similar photometric data extraction has been demonstrated on previous missions, and have yielded promising results [94]. Using stars as a spatio-temporal reference and a photometric reference, RSO characterization can be improved up on. The improvements will be further detailed in Chapter 5. Part of the RSOnar payload data processing aim is to demonstrate the feature extraction ability of RSOnet, by adapting specifically to the instrument and its images. The objectives were to collect and process thousands of images from a high altitude payload to detect and characterize RSO for SDA.

The contributions of this research enable any star tracker migration capabilities from an attitude determination sensor to a surveillance sensor, as long as imaging is done in a statistical and random pattern without actively seeking out targets. The implication of converting star trackers into space-based space surveillance sensors is that it could greatly expand the number of surveillance sensors

in orbit. Star trackers are already present on many spacecraft, and converting them into surveillance sensors could provide a cost-effective way to increase SSA coverage. This would improve our ability to track and predict the movements of objects in space, and would help to reduce the risk of collisions and other space hazards. Another implication of this conversion is that it could allow for more frequent and accurate tracking of objects in space. Star trackers are highly sensitive and precise instruments, capable of detecting even small changes in the position and orientation of an object. This would enable more accurate determination of an object's orbit and would provide better situational awareness of space threats.

However, there are also some potential drawbacks to converting star trackers into space-based space surveillance sensors. For example, it could require modifications to existing spacecraft, which could be costly and time-consuming. Additionally, there may be concerns about the privacy implications of using existing space assets for surveillance purposes. Although an orbital demonstration is out of scope in this research, a sub-orbital mission will address the potential drawbacks and mitigate the number of modifications necessary to existing star tracker processing methodology, which are the key contributions of this dissertation.

2.4 Summary

In this chapter, previous research efforts have been analyzed in their effectiveness to collect valuable SDA data. As concluded in previous works [11] [10], no one methodology addresses all SDA requirements, and data fusion is required for a holistic view of SDA. The research and methodology presented in this dissertation is aimed at providing a more quantitative, low-cost, near real-time and holistic view of the situation in LEO.

3 Chapter Three: Virtual Constellation of Space Traffic Cameras for Space Domain Awareness

This chapter describes the simulation efforts undertaken to study observation scenarios at scale. Research in this chapter focuses on observation strategy, observer and RSO orbits and how they relate to SDA.

3.1 Virtual Constellation Analysis Simulator

The Python-based simulator is designed to propagate 100s of thousands of orbits for the target RSOs and observers. The simulator's customization enables detections to be analysed in pseudo real-time.

3.1.1 Simulator Requirements

To determine the specific requirements of the STC using the equations from Chapter 2, a simulation environment called virtual constellation analysis simulator (ViCAS). ViCAS is a simulation tool that is designed to study and simulate thousands of observers and RSO interactions simultaneously, without generating observation images. ViCAS is built in contrast to previous tools such as Systems Tool Kit (STK) and Space-Based Optical Image Simulator (SBOIS), which only simulate a few observers and RSO at a time, but generate simulated images. STK and SBOIS require accurate ephemeris data of existing satellites, which describe the position, velocity, and attitude of

an RSO. These tools accurately propagate orbits and can be used to determine space situational awareness (SSA) requirements. However, they are limited in their ability to simulate large-scale interactions between multiple observers and RSO. ViCAS was designed to overcome these limitations by simplifying the propagation and modeling of RSO-observer interactions at scale. It is a statistical and numerical simulator that focuses on the spatial densities of RSO to identify the most suitable orbits, camera mounting configurations, and specifications for observers. Unlike STK and SBOIS, ViCAS does not generate observation images but provides insights into the optimal SSA configurations for given observer locations and RSO densities. A similar modeling tool has been developed at the United Kingdom's Defense Science and Technology Laboratory (DSTL) [72] previously, which is unconstrained by a specific instrument, and only considers distance to target.

The simulator built for this research had a unique set of features. The simulator follows the Sun-Earth reference frame to optimize for viewing geometry. The simulator has capacity to propagate the 22,000 RSO currently tracked by SSN, but also model into the future with up to 50,000 RSO. It is also built to facilitate several thousands of STC, and process all potential detections for each STC. The STC network configuration, size, and orbits had to also be defined based on existing, planned and recommended future constellations. The custom simulator built for this research optimizes on processing time, varying STC network configurations and scalable model functions.

3.1.2 Objective and Scope of Simulation

Virtual constellation analysis simulator (ViCAS) is a Python-based open sourced simulator designed to derive STC sensor requirements. RSO orbit simulation is simplified using quaternion rotation functions, by defining the key reference frame responsible for optimizing detections [95] [96] [97]. Figure 3.1 below illustrates the Geocentric Celestial Reference Frame (GCRF) adopted for the simulator where the X-axis is aligned with the mean equinox of Earth at 12:00 Terrestrial time of the 1st of January, 2000, and the Z-axis is aligned with the Earth's rotation axis. The Sun lies on the ecliptic plane, where as the spin axis of the Earth, which is perpendicular to the equatorial plane, is tilted by 23.4°. The terminator marks the line dividing the Earth into two equal sized hemispheres, one with sunlight and the other in shadow. The terminator line is in fact a gradient

between sunlight and shadow due to atmospheric scattering, however, this definition is excluded as Earth reflectance is not considered due to negligible effects.

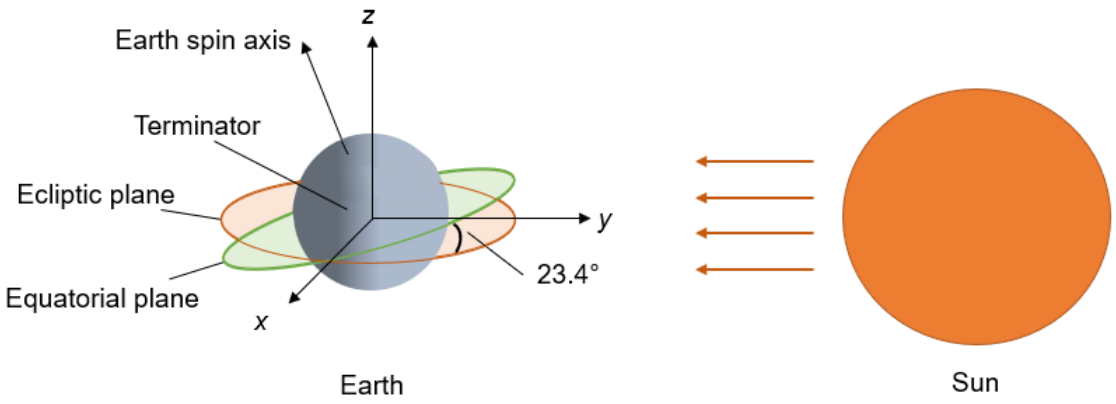

Figure 3.1: Visualizing key reference frames for optical RSO detection

Various orbits can be defined using quaternion rotations about the reference frame. Table 3.1 below identifies the key orbit classes utilized in ViCAS. These orbital simulations are verified by creating identical scenarios in STK, where distance vectors are used between the observer, RSO and Earth. The propagators used on each are identical, therefore the root mean squared error of each distance vector was confirmed to be below 5 km, which has a negligible impact on the statistical simulator.

Table 3.1: RSO Orbit Classes defined in ViCAS

Orbit Class	Defined Inclination	Axis of Rotation	Axis of Phase
Dawn-Dusk	98°	Y	N/A
Sun Synchronous	98°	X and Y	Z
Polar	near 90°	X and Y	Z
Low Inclination	80° or below	Earth spin axis	Z

Sun-synchronous orbits closely lead, lag or match the terminator over the course of the year. A dawn-dusk orbit is a special case of a sun-synchronous orbit, where the orbit matches the terminator, ensuring the Sun is always on the same side of the satellite. The 98° inclination is further refined depending on mission requirements to revisit the same position on the Earth's surface at the same time every day. In ViCAS, the Sun-synchronous class orbits rotate about the X and or Y axis

depending on the phase shift applied along the Z axis. Polar orbit ground-tracks pass closely by the Earth's poles, and are popular for high latitude applications. Low inclination orbits, generally prograde but may also be retrograde, service the middle latitudes, where a majority of the Earth's population resides. This technique allows for nearly all LEO classes to be simulated using ViCAS. Visual examples of each orbit are shown below in Figure 3.2.

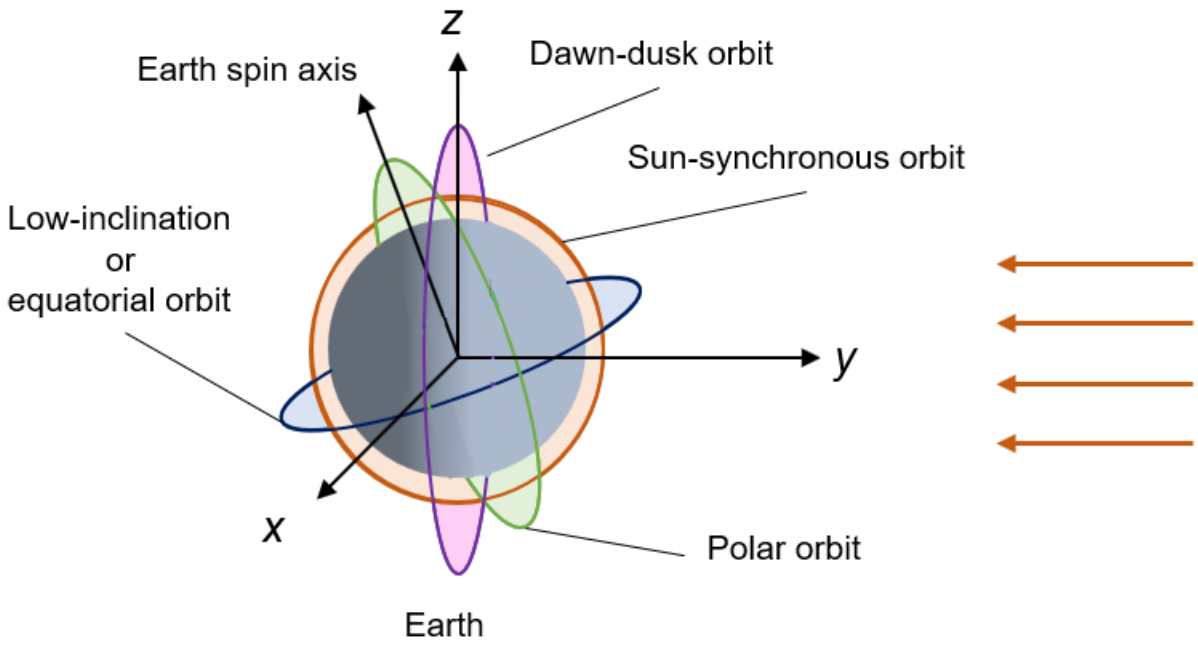

Figure 3.2: Visualizing examples of the orbital classes in ViCAS

The purpose of the simulator is to study RSO viewing opportunities for the STC with a statistical and numerical approach. ViCAS is designed to take as input a total RSO count, which defines the Earth RSO population. The Earth RSO population is a customizable feature with a default setting of current RSO population as per space-track.org. A second input defines the STC network configuration, usually in the form of a constellation of a group of constellations. The network configuration requires manual input to customize the observers, their orbits and their payload specifications. A time step function propagates orbits and STC pointing direction as per a defined step size. At each time step, detections are computed and stored. All STC follow an Earth-pointing scheme, where the nadir vector points at the centre of the Earth. An illustration is shown in Figure 3.3. The Earth pointing is not the only pointing condition possible; however, the analysis is easier

to contextualize at any moment in time during the simulation. The pointing is discussed in section 3.2.2.

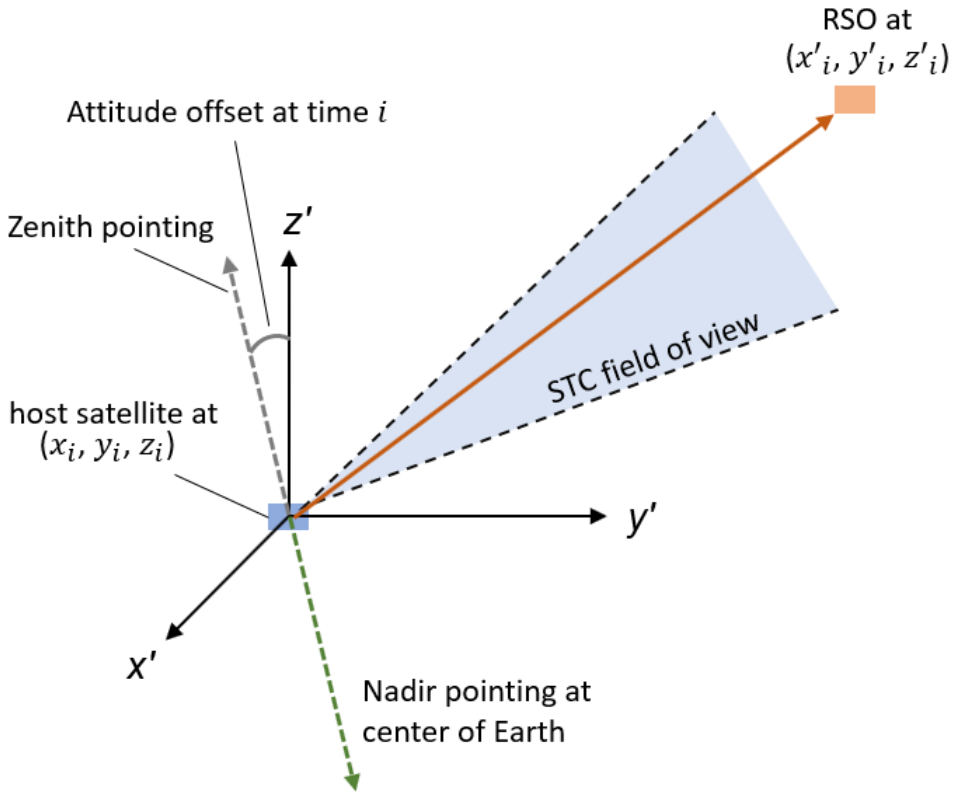

Figure 3.3: Visualizing host satellite attitude and relative RSO positioning

At each time step, all potential RSO detections are computed using Equations 2.1 to 2.5 and the necessary data is recorded. Processed over several time steps, a simulation scenario is generated.

3.1.3 Earth $E_\emptyset$

Earth $E_\emptyset$ is defined as the current RSO population, and is generated using current RSO demographic characterization. The characterization of RSO for ViCAS is defined using size, inclination and altitude. The size distribution is divided into 3 bins, centered at 10 cm, 1 m and 10 m. The total RSO pool for each size bin is a scalable form of the RSO size distribution function [16]. The orbital inclination and altitude distribution of the current RSO population [98] is also a scalable input.

RSO orbit inclination, altitude and size are not enough characteristics to define unique orbits in ViCAS. The position of an RSO along it's orbital arc is determined by a random rotation along its axis of rotation. The phase of the orbit is determined by an even spacing of all RSO at the same inclination and altitude. These techniques allow for easy constellation mapping on to ViCAS reference frame. The scalable functions for size, inclination and altitudinal distribution of RSO allow for easy scaling operations to study future Earth scenarios. Following this format, Earth E_{2022} is the standard RSO population applied to all Earth scenarios considered in this research. Earth E_n defines an Earth in year n, where a scaling factor is applied based on expected multiplicity of RSO.

3.1.4 Simulator Validation

Astrometric validation of the simulator was conducted by comparing the distance vectors and signal to noise ratios in various scenarios to previously validated simulators like STK and SBOIS. In the first validation scenario, two identical orbits were defined for the RSO and observer with the observer lagging behind the RSO at a fixed phase value of 0.11°. The observer carried an optical payload pointing in the ram direction, or the direction of travel. The pointing orientation ensured the RSO was always visible and in field of view. At an orbiting altitude of 800 km, the RSO is approximately 12.2 km ahead of the observer. The same scenario was generated in STK where the distance between the RSO and observer was validated to be 12.2 km. Over the course of the orbit, the distance variance for ViCAS and STK was no greater than 0.5 km. This scenario was replicated for each orbit illustrated in Figure 3.2.

Additional astrometric validation was performed by studying the signal to noise ratio in ViCAS. In this scenario, an RSO was placed in the same orbit as the observer travelling in the opposite direction. The RSO was detected at the specified 300 km maximum range and gradually approached closer to the observer. The scenario tested for detection confirmation at ranges between 0 and 300 km. The scenario also validated the time two orbiting objects approach each other using their orbital velocities by sampling at 100 Hz. Since the measurements were made using the simulator, the data points exactly matched the results provided by Equations 2.1 - 2.5. This scenario was replicated for each orbit illustrated in Figure 3.2 using a Lambertian sphere as the RSO.

The steps taken above ensured that the simulator introduced no new sources of error to the

modeling of RSO and observer interactions. The final scenario verified that two observers detected the same RSO by merging the previous two scenarios. Here, the observer travelling in the opposite direction first detected the RSO, followed by a delayed detection of the other observer confirming its position lagging behind the RSO. The identities of the RSO are logged upon detection. A simple software was written to verify matching identities of the RSO at the same time from both the observers.

3.2 Analysis and Discussion

Future RSO demographic modeling of RSO has proven to be highly unpredictable, as the true value depends on economics, launch cadence, launch capacity, ride sharing and other factors. Instead, this research will consider a few scenarios for a comparison study.

3.2.1 Simulation Scenarios

The first scenario considered is the Starlink constellation by Space Exploration Technologies Corporation or SpaceX [99]. There are over 2000 Starlink satellites already in orbit and that number is expected to double in the next 2 years. Following this trend, the Starlink scenarios are considered at 2, 4 and 6 years into the future. The second scenario considered is the Lightspeed constellation by Telesat [100]. Lightspeed is expected to scale to 300 satellites in 2 years. This research will project forward and estimate a total of 1000 satellites in 4 years and 2000 in 6. The third scenario considered is one proposed by this research as potentially the most efficient scenario. A group of dawn-dusk sun-synchronous orbit (SSO) satellites with a projected count of 100, 1000 and 2000. The final scenario considered is a random subset of the total RSO population as it increases over time. At random, 5% of the RSO population is converted into an STC network instrument, orbit irrelevant. A summary of the scenarios considered in this research is presented in Table 3.2.

Table 3.2: Constellation satellite count and RSO population scenarios

Constellation	E_{2022}	E_{2024}	E_{2026}	E_{2028}
Starlink	2,000	4,000	6,000	10,000
Lightspeed	N/A	300	1,000	2,000
Dawn-Dusk SSO	N/A	100	1,000	2,000
5% of total RSO population	1,100	N/A	N/A	2,500
Total RSO population	22,000	30,000	40,000	50,000

Each constellation scenario consists of various kinds of orbits distributed depending on the mission objectives. For example, Starlink [101] and Lightspeed are LEO communication satellites which rely on low-inclination, low altitude orbital shells to provide wide network coverage. The key difference between these two is the orbital altitude and satellite count. The SSO constellation is a virtual grouping of all the dawn-dusk orbit satellites at varying altitudes. The 5% chosen at random is the control scenario. A summary of each constellation's breakdown is provided in Table 3.3. The selection for the altitude for Starlink and Lightspeed are based on their design specifications. The selection for the altitude for the SSO constellation is selected to cover all of the defined LEO region, centred around the regions considered to be the most crowded [98]. Given the 300 km distance limit established on the simulator, the maximum distance between two orbital regions for SSO is less than 600 km. The choice for the 98° inclination is to ensure the observer is ideally tracking the terminator. In a real-world scenario the orbit of the satellite would not follow the ground-track of the terminator exactly, however the effects of this variation on the final results is considered negligible for the statistical simulator. The statistical analysis of the simulator, which repeats each scenario 100 times, averages out minor deviations that may otherwise exaggerate the results. An example of this is visible in Figure 3.3.

Table 3.3: Constellation scenarios and parameters that define them

Constellation Scenario	Inclination (°)	Altitude (km)	Share of Total
Starlink	50±5	550	66.7%
	70±5	550	11.1%
	90±5	550	11.1%
	98	550	11.1%
Lightspeed	70±10	1000	66.7%
	90±5	1000	33.3%
SSO	98 (dd)	400	20%
	98 (dd)	800	20%
	98 (dd)	1000	20%
	98 (dd)	1400	20%
	98 (dd)	1800	20%

(dd) refers to the dawn-dusk classification of the sun-synchronous orbit

3.2.2 Simulation Results

The simulation results are discussed in the context of SDA with the following objectives:

- Study the changes to simulation parameters that affect the total RSO detection count in single and multiple observation scenarios
- Identify key metrics that optimize the efficacy of the STC
- Identify and discuss key metrics that optimize for RSO detection and characterization
- Derive a set of requirements and constraints for the STC, in context of RSO detection, characterization and payload hardware feasibility

Some important ViCAS assumptions are listed below:

- ViCAS identifies an RSO detection valid above a SNR of 1. It is theoretically possible to detect RSOs above SNR of 1 on a star field image; however, this may not always be true for all detection algorithms. The detection sensitivity will be further discussed in Chapter 4.
- All STCs in ViCAS have a fixed field of view of 26°. The field of view of a camera is dependent on the aperture size and focal length. In a significant majority of cases, a large field of view is achievable via negligible size and mass changes.

- All STCs in ViCAS have a fixed exposure time of 0.1 seconds. A longer exposure time may skew the results in favour of more detections than is otherwise possible with a stare-only camera. The observation strategy is further discussed in Chapter 4.
- Every time step is defined at 1 minute. Every simulation scenario is run at intervals of 100 minutes, that is 100 steps. ViCAS can simulate at time steps of 1 second, but the simulation results are not significantly affected by this finer adjustment. The 1 minute interval improves the simulation time by 60×, which is significant considering that some simulation runs take upwards of 7 days.
- All RSO detections are range limited to 300 km. The range limitation is introduced to minimize simulation time. Instead of studying the range, the results study the visual magnitude and the SNR of the RSO detection to determine the sensitivity of the camera. Based on this assumption, for larger aperture cameras, the detection estimates are considered conservative.

A second simulation effort is presented in [102] using ViCAS for a modified set of assumptions, requirements and results. The modifications pertain to a specific satellite constellation and different imaging strategy. Results of both the variations offer useful insights discussed below.

Aperture Size The aperture size directly impacts the sensitivity of a telescope. Larger apertures collect more photons, and therefore are more desirable. However, the camera's size directly impacts the payload volume and mass, which will be further discussed in Chapter 5. The trade-off for a larger aperture size can also be measured by the increased number of detections for the same constellation scenario. Figure 3.3 plots the number of detections over 100 minutes of simulation per constellation scenario over varying aperture sizes.

Each constellation scenario's results are duplicated over a 5 cm, 10 cm and 15 cm aperture size. The height of the bar plot represents the average number of RSO detections for a given constellation scenario. The vertical black line represents the range of the number of RSO detections over many simulation runs. The top of the black line represents the number of detections in the E_{2028} simulation run, and the bottom represents the same for E_{2022}. Each simulation run randomizes the starting positions of the STC host satellite to ensure that the results of one simulation run is not an anomaly. There are 100 total repetitions of the scenario to account for the randomization, which is considered a large enough sample size to account for the minor deviations in the simulator. The

number of detections in Figure 3.3 is an average for all simulation runs E_{2022}, E_{2024}, E_{2026}, and E_{2028} combined, which is why the range of detection count for each aperture size is so large. The bottom of the black line represents the least number of observers for each bar plot, whereas the top represents the most observers. Figure 3.3 (a) shows the expected number of RSO detections for the random 5% scenario and the Lightspeed constellation. Figure 3.3 (b) shows the same for Starlink and SSO constellation scenarios. It is evident from the results that the observer count is not the most significant factor for passive surveillance as previously thought.

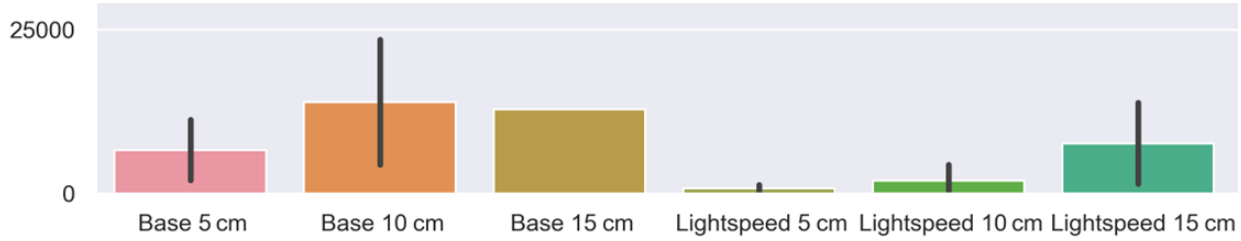

(a) Base and Lightspeed constellation

For each scenario, increasing the aperture size correlates to an exponential increase in RSO detection count. This is expected, since a linear increase in aperture diameter increases the aperture surface area by the square, causing an exponential increase in the number of photons collected. This is also despite the simulation being range limited to 300 km. For larger aperture sizes, RSO detections occur at slightly higher solar phase angles. Figure 3.4 illustrates this. There are certainly more detections possible beyond the 300 km range limit. As per the detection definition, more RSOs pass the detection SNR limit of 1 to register a detection.

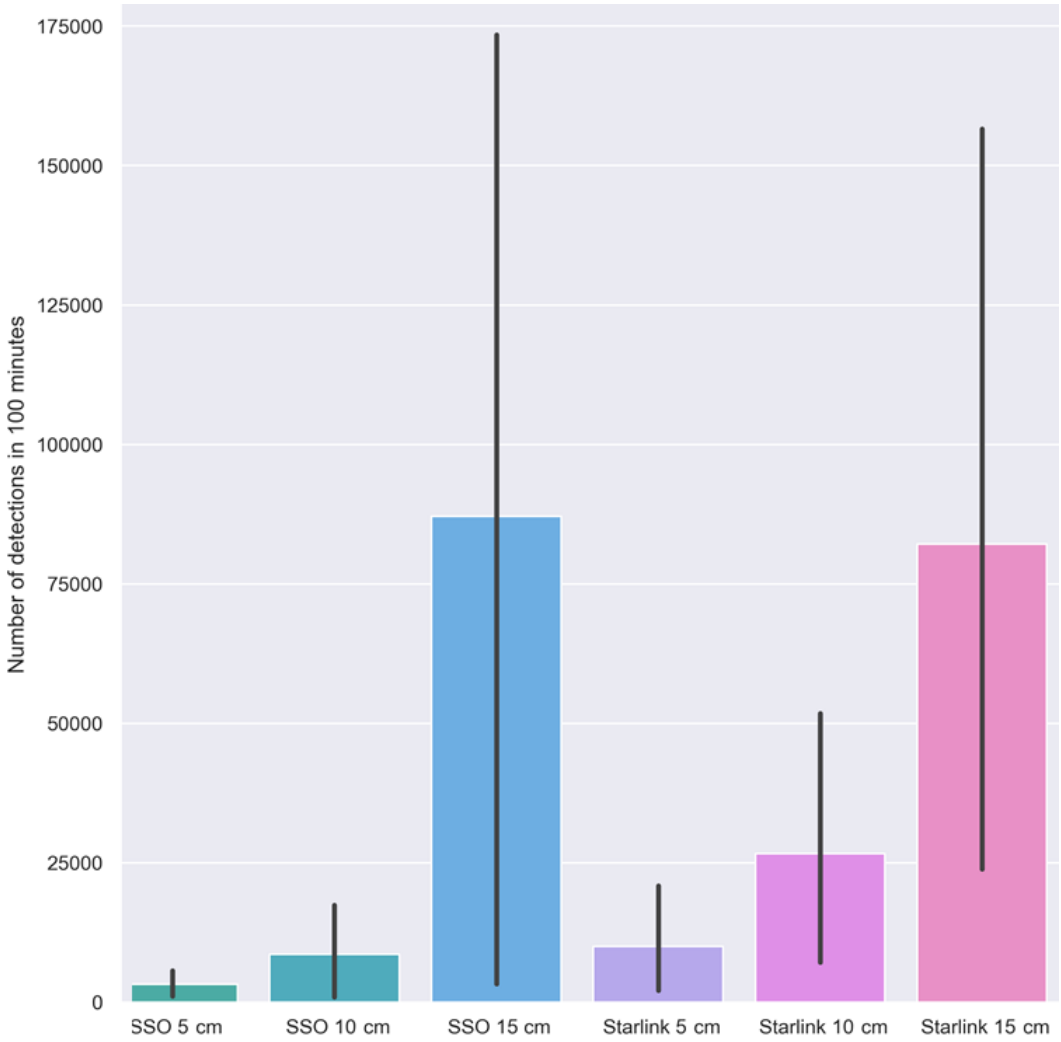

(b) SSO and Starlink constellation

Figure 3.3: Effects of STC aperture size on the number of detections in 100 minutes of simulation

(a) Aperture size = 5 cm

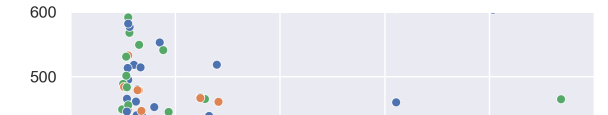

Beyond detection count, a larger aperture size also improves the duration of RSO detection. Figure 3.5 below compares aperture size variation to the average duration of observation. The effects are considered marginal, as the increased duration of observation is likely due to the increased sensitivity of detection. This applies to two scenarios. Firstly, a scenario where the RSO's range from the STC is increasing and or decreasing and the RSO crosses the specific distance limit for registering a detection. Secondly, a scenario where an increasing and or decreasing solar phase angle has the same effect. Registering even a modest increase in the duration of observation for larger aperture sizes, at a step size as large as 1 minute, indicates an unexpected benefit of larger aperture cameras. The improved sensitivity and longer duration of observation are relevant metrics for RSO detection and characterization.

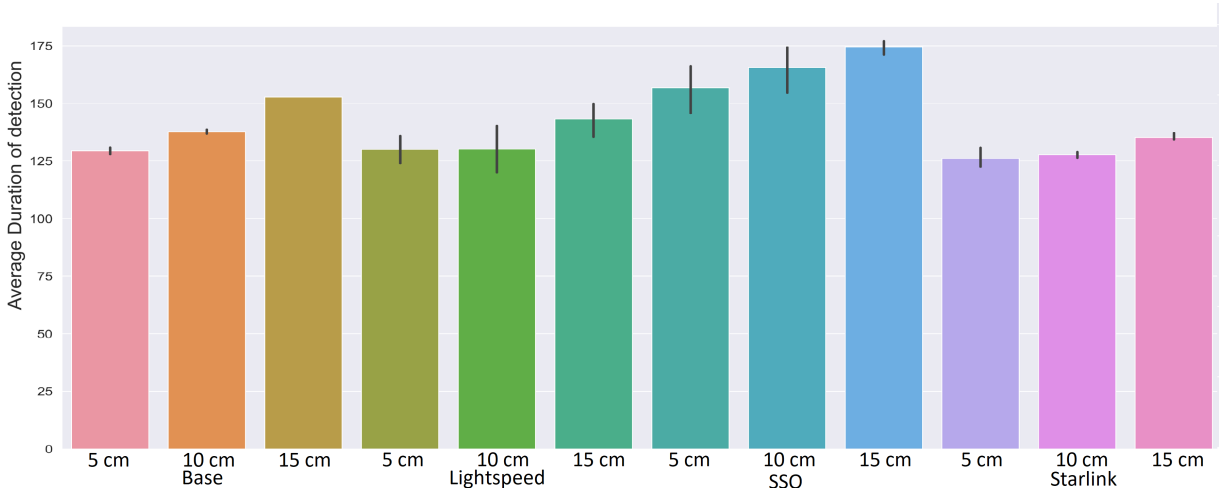

Figure 3.5: Effects of aperture size on object detection duration for each constellation type

The conclusion, regarding the choice of aperture size, is a complicated trade-off. A smaller count of STC at 15 cm aperture achieves similar results as a larger count of STC at 5 cm. Figure 3.6 below is a plot of the average percentage of time each individual RSO remains detected during its orbit. A comparison of the many trade-offs suggest that every satellite capable of hosting one or many STC should be accommodated for. Meaning a one-size fits all payload solution may limit the overall STC payload adoption, and a gradient of STCs should be considered. This trade-off also depends on the orbit of the satellite, as some orbits are favoured for lower apertures than others. In specific the dawn-dusk sun-synchronous orbit is ideal.

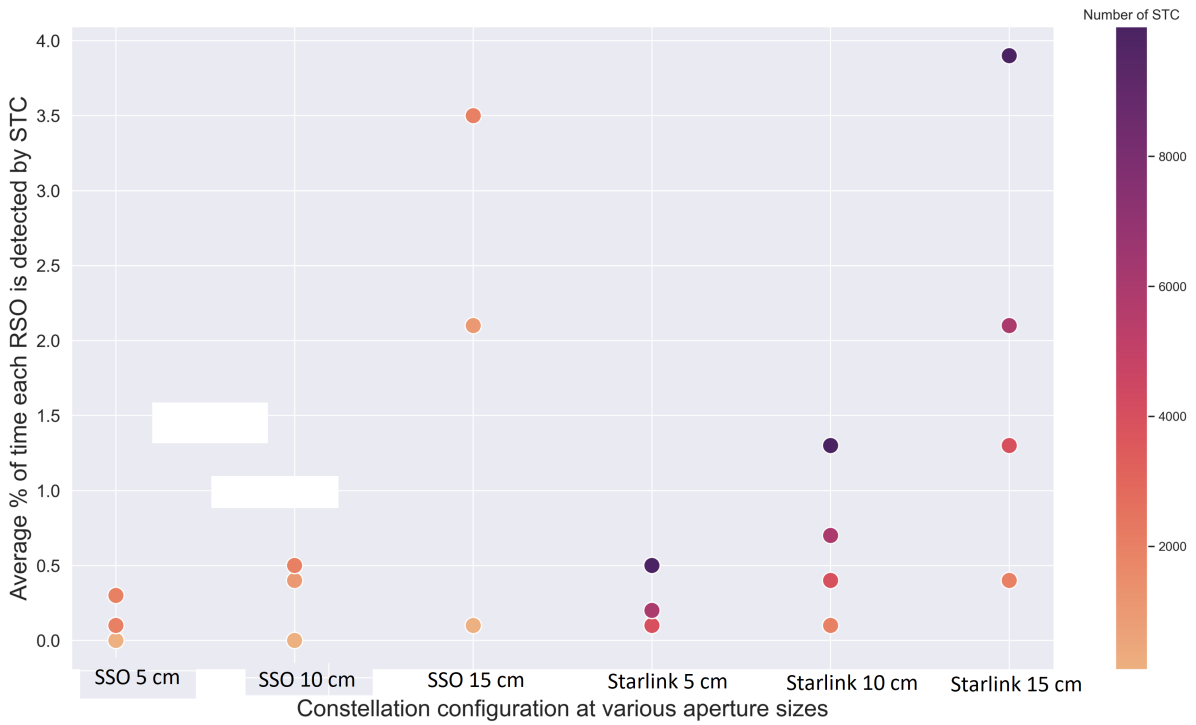

Figure 3.6: Average RSO detection and coverage statistics

Camera Mount The mounting direction of the camera also impacts the detection count of an STC. Since individualized attitude regimes are not in scope of the simulation, all satellites are considered Earth-pointing in the nadir direction. For reference, Figure 3.7 below illustrates the directional terminology used. When referring to a particular mounting direction, the boresight vector of the camera is the same as the pointing vector. The boresight refers to the vector between the center of a circular aperture and the imaging sensor. After boresight alignment, an object directly along the pointing vector appears in the center of the image.

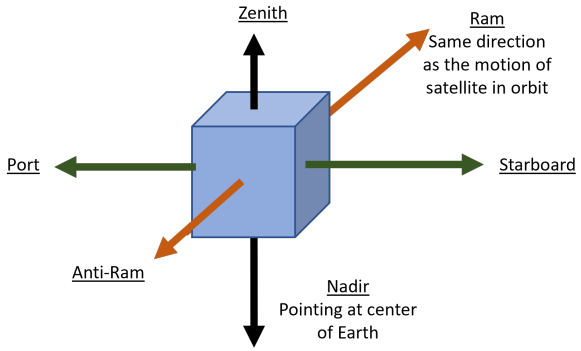

Figure 3.7: Camera mounting direction and terminology

Figure 3.8 provides a summary of the detections possible with each camera mounting direction per constellation scenario. Nadir pointing is not considered as RSO detections with Earth's surface in the background is not in scope of the research. In all scenarios, zenith pointing is the least rewarding. Part of the reason for the reduced detection count facing zenith may be the 300 km detection limit in the simulator; however, the primary reason is due to the high solar phase angle and large step size. The minimum solar phase angle for a zenith detection is 75°, at which point the object's facet play a larger role. These results will vary drastically when considering a more accurate 3D model of the RSO, as supposed to the Lambertian model in ViCAS.

The large simulation step size also plays a significant role as objects have a higher angular velocity in the zenith direction even at large distances. Future simulation efforts should take this into account. RSO detections are still feasible with a zenith camera mount; however, the relative distribution of RSOs from any given host satellite is greater in the port-starboard and ram-anti-ram plane compared to the zenith-nadir axis. Specifically for the STCs in the SSO constellation scenario with dawn-dusk orbits, the port mounted STC achieves the highest number of detections and the starboard mounted STC achieves almost none. In most orbit configurations, however, ram and anti-ram facing STC have consistent detections throughout their orbit. Sun sensors are a critical component for efficient mission automation and to ensure safety of the camera from the damaging effects of direct sunlight.

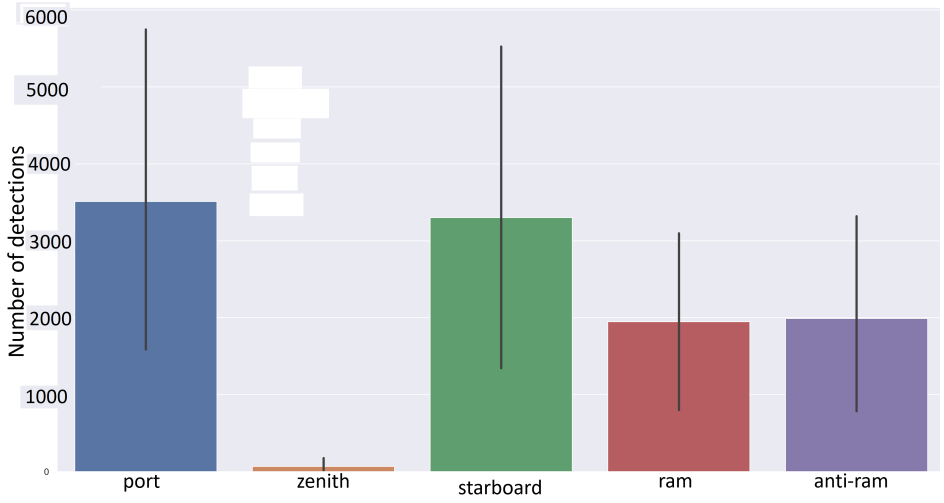

(a) Base constellation

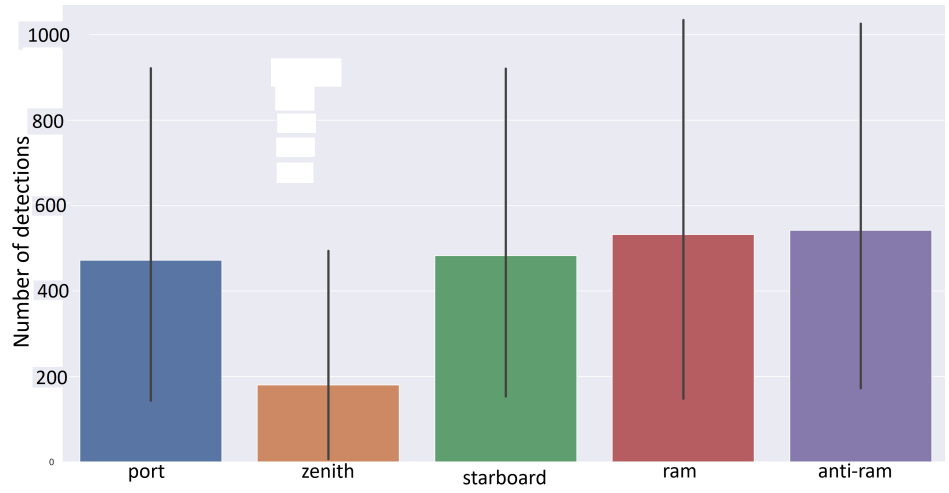

(b) Lightspeed constellation

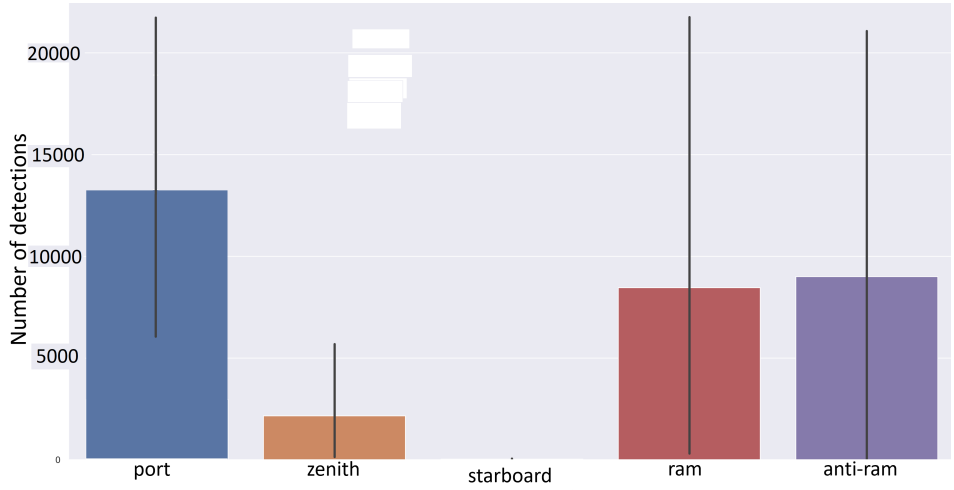

(c) SSO constellation

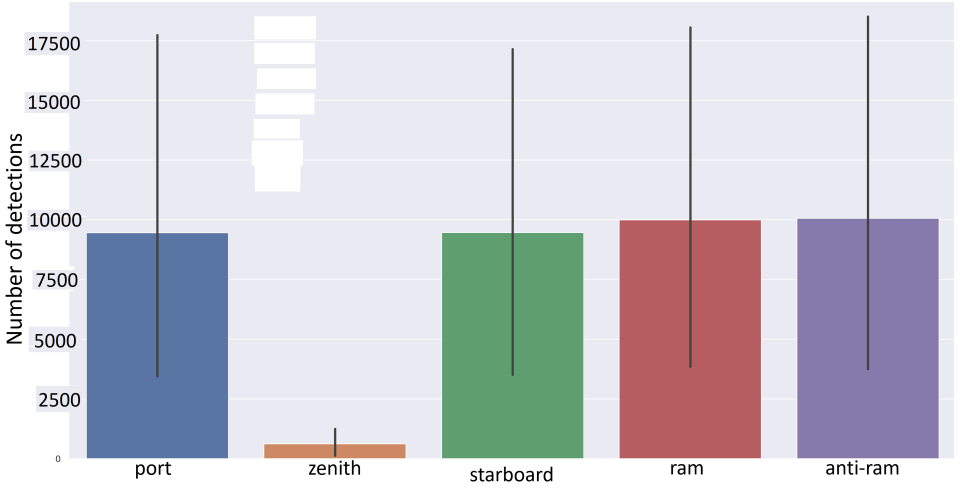

(d) Starlink constellation

Figure 3.8: Effects of camera mounting direction on the number of detections in 100 minutes of simulation

The high detection count in the port direction in Figure 3.9 (a) is because the sun is ever-present in the starboard direction of the STC. As inferable from Equation 2.1 and Figure 3.2, the ideal situation is when the positions of the sun, satellite and RSO are close to a straight line, in that order, which is the case for a port mounted camera on a dawn-dusk orbiting satellite. A solar phase angle of 0° is achievable routinely. Figure 3.9 (a) further illustrates this point.

For the SSO scenario, most of the detections occur around the poles. Figure 3.9 (b) shows the position of the observer on the Z axis when a detection is registered. The top and bottom of the Z axis represent the polar regions of the Earth. LEO satellites crowd inclinations 57° and higher, and higher inclinations are preferred for most mission objectives. In high latitude regions in the northern and southern hemisphere, more orbital planes intersect than near the equator. Thus, detection density increases above 4000 km and below -4000 km on the Z axis. Depending on the inclination difference between the observer and the RSO, the duration of time varies. As seen in Figure 3.9 (b), some RSO have similar inclinations as the observer and are consistently detected for over 40 minutes. The long duration tracking scenario is extremely rare to occour naturally; however, it is common for a formation flying or rendezvous operation.

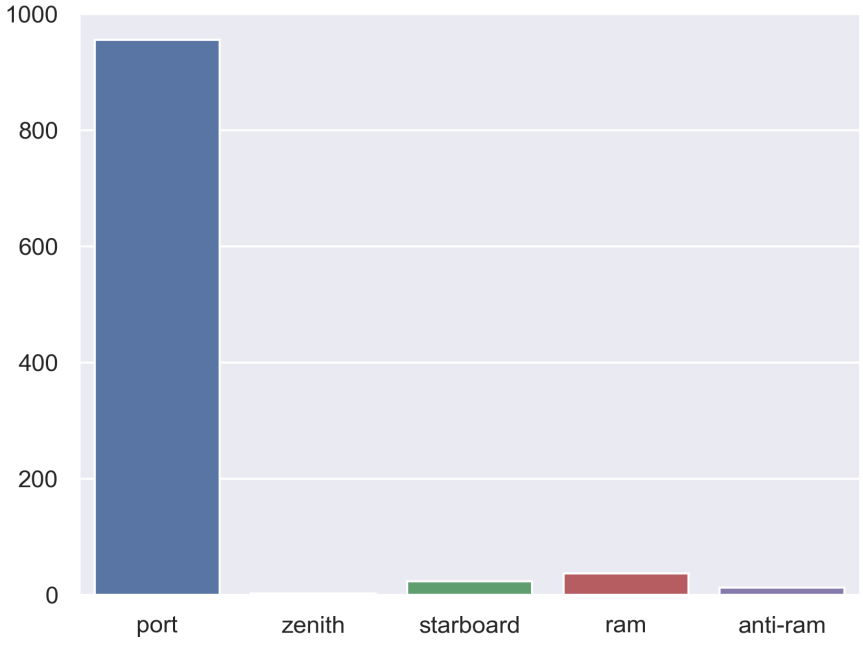

(a) Detection count per camera mounting direction

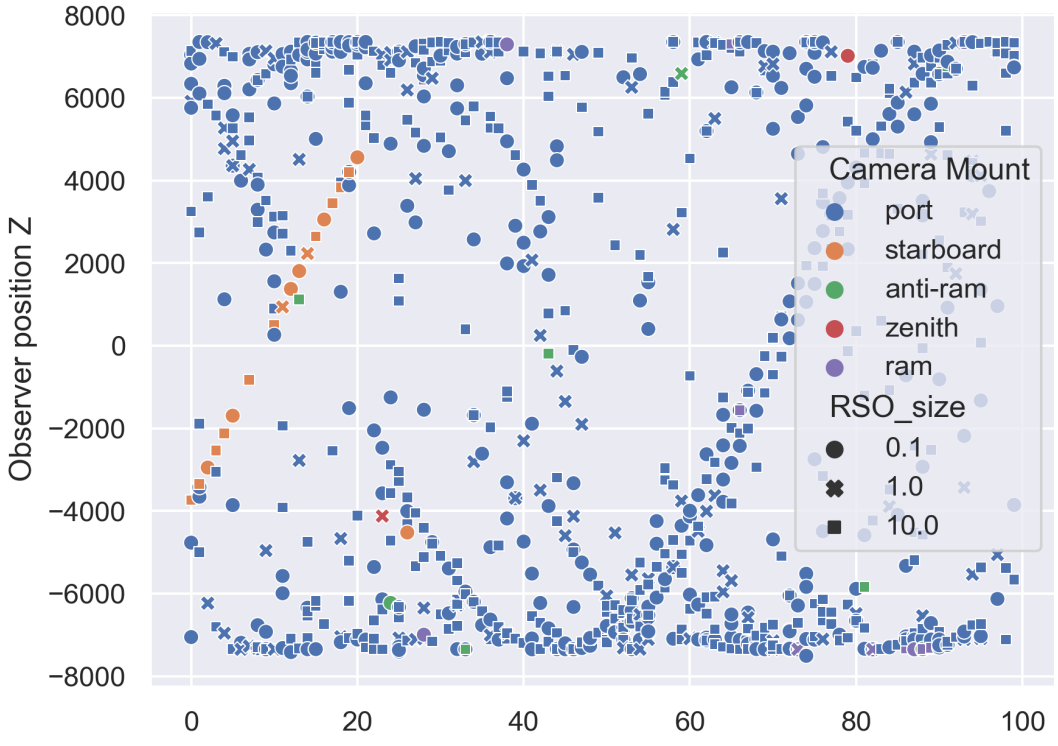

(b) The Z axis position of host satellite when an RSO detection is registered

Figure 3.9: Camera mount and host satellite position results for $E_{2024\,SSO}$ with an aperture of 10 cm. Please refer to dawn-dusk orbit illustration in Figure 3.2 for Z axis position definition.

A summary of results for the average detections based on mounting direction is provided in Figure 3.10. The results are averaged over all observer orbits to provide an overall summary of surveillance. Camera pointing along the horizontal plane, perpendicular to zenith-nadir axis, is preferred. In most cases however, the camera pointing direction can be optimized according to the host satellite orbit. There is a trade-off to consider between active and passive surveillance approach. For future efforts to improve these results, it would be beneficial to determine the pointing vectors and present the results as a heat map in 3D space. In many cases, hosted payload slots on satellite are determined after the requirements for the primary mission are met. Therefore, the results presented here indicate the flexibility of a passive STC's mounting direction, and also stipulate the possibility of multiple STCs being hosted on the same satellite.

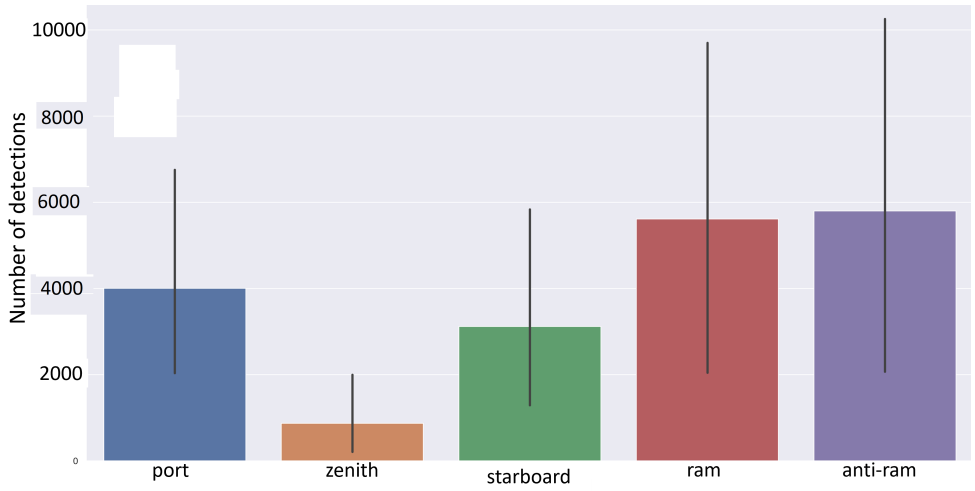

Figure 3.10: Effects of camera mounting direction on the number of detections in 100 minutes of simulation

Duration One of the major benefits of space-based optical instruments, specifically for SDA in LEO, is the potential for long-duration RSO observation. Assuming a circular orbit, from the surface of the Earth a LEO satellite with an altitude of 1000 km has an approximate angular velocity of 1500 arcseconds per second or 0.42° per second. At this rate, a ground-based observer is in direct line of sight with the satellite for less than 12 minutes through varying atmospheric densities. The ground-based observation is often complicated with varying seeing conditions, angular rate tracking accuracy, weather, obstructions and pass prediction. From space, even with non-tracking body-fixed camera mounts, short-duration RSO observations can be routine. Figure 3.11 below illustrates the average lengths of observation possible for each RSO detected, separated by constellation scenarios. The girth of the coloured violin plot indicates the expected probability density of observation duration. The scatter points represent the averages from each simulation run. The thin line stretching out from each scatter point indicates the standard deviation observation durations for each simulation run. As evident from the diagram, the duration lengths do not change significantly depending on the constellation scenario. The exception is with the SSO constellation scenario, where the average is marginally higher and the range of possible values increases significantly. Figure 3.9 (b) illustrates how a port mounted (see Figure 3.6) STC on a dawn-dusk sun synchronous orbit satellite has opportunity to detect an RSO for longer durations, as seen by the sinusoidal detection patterns for size consistent RSOs.

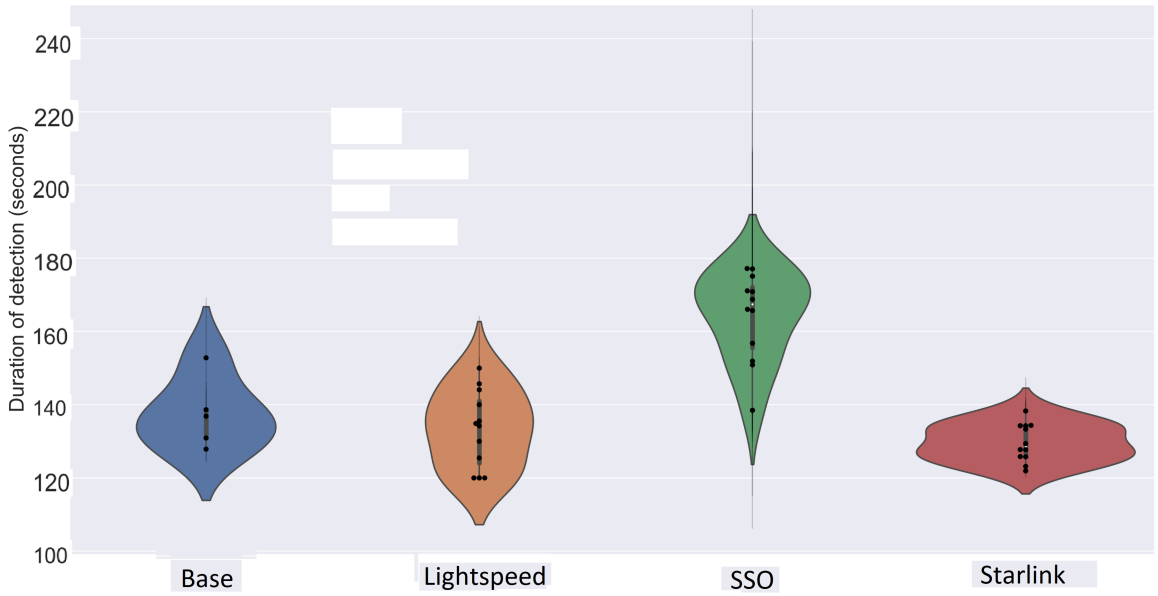

Figure 3.11: Length of continuous observation duration for RSOs detected

Virtual constellation configuration It is clear that the SSO constellation scenario is ideal for RSO observation. Figure 3.12 below illustrates this clearly. Far fewer STC-hosting satellites are required for a comparable number of detections in another constellation scenario. In some cases, similar number of RSO detections are possible in the SSO constellation scenario with smaller aperture size or fewer host satellites or both. However, this comparison does not consider the adoption and launch rates for satellites in these constellation scenarios. Dawn-dusk launches are non-deal for Earth observation, communication satellites and most scientific objectives. However, an increase in launch to this niche orbit will likely increase due to it's benefits for space surveillance. A reason for separating the simulation scenarios, referring to $E_{2022,2024,2026,2028}$, is to place context on the size of the STC constellation. By the assumptions laid out in Table 3.2, the constellation scenarios are not to be considered as competitors, rather as requirement modifiers. The control scenario, where 5% of the satellites host the STC payload, is the second best performer and likely a more practical real-world scenario. The control scenario assumes the current launch cadence and orbit selections continue until 2028.

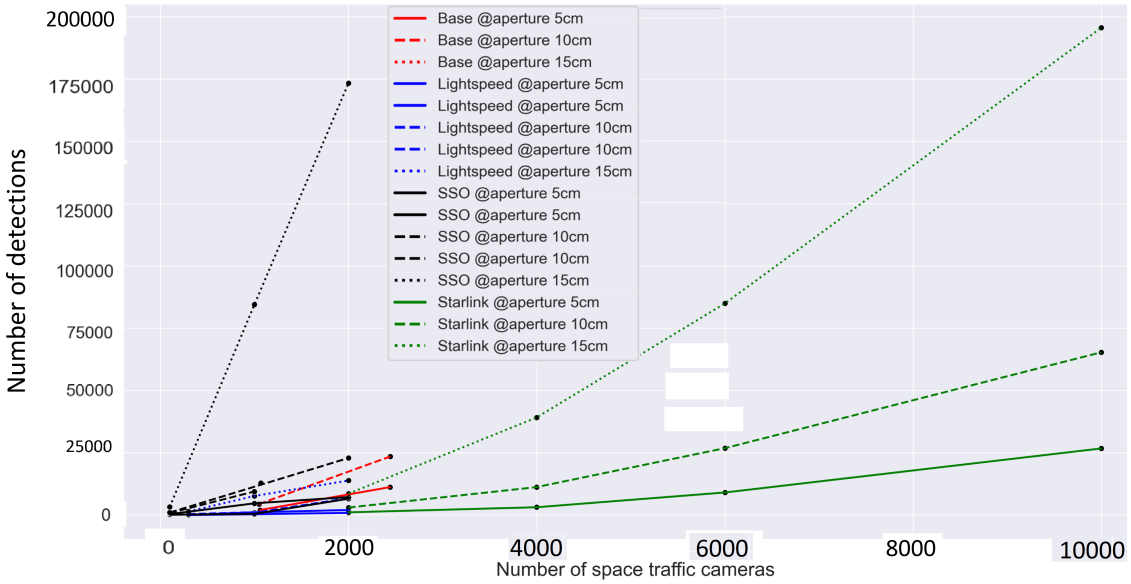

Figure 3.12: Number of RSO detections possible with number of satellites with STCs

One of the main advantages of the STC network concept is the probability of multi-site detections. Figure 3.13 below illustrates the multi-site observation results, where 2 or more STCs observe the same RSO at the same time. Given the geographical spread of the STCs in a network, multi-site detections have scope for improving RSO astrometric and photometric characterization.

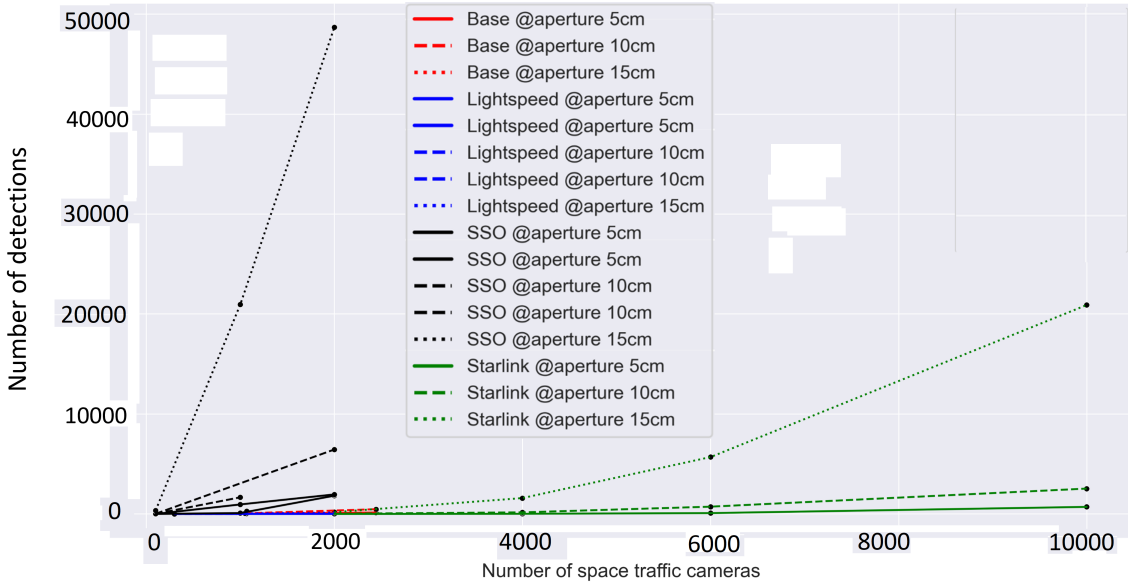

Figure 3.13: Number of multi-site RSO detections possible with number of satellites with STCs

Analysis of RSO from multiple perspectives have been shown to improve astrometry and photometry results [49]. An STC has a high likelihood to be a supporting observer by enabling many

multi-site observations, hereby reducing the measurement uncertainties. Collaboration of data with other ground-based instruments would certainly augment the capabilities of surveillance.

Other noteworthy benefits of the STC network concept include on-the-fly calibration and benefits to RSO identification and characterization due to longer-duration and multi-site observation. On-the-fly calibration refers to astrometric and photometric calibration of the STC optics when an STC-hosted satellite is detected by another STC-hosted satellite. This includes calibrating for position, velocity, optical properties and detection sensitivity. Further study of these research topics, which are out of scope for this research, can be enabled with the STC network concept.

3.2.3 Summary

The simulator design in this research enables a comprehensive assessment of the STC payload and its contributions to the surveillance aspect of SDA. ViCAS is capable of evaluating the potential surveillance benefits of enabling surveillance capabilities on the current star trackers in orbit. It is also capable of projecting the surveillance potential of future launches with the STC payload. ViCAS has a modular design and also has the ability to include additional sensors and features to reduce the difference between simulation and real-world outcomes. The key outputs of the simulator are the analysis metrics which are produced and discussed below.

It is clear that adoption of the STC payload in large numbers is the key to the STC network's success. Even in small numbers, novel observation opportunities persist. As a standalone system, there are several limitations of the STC network. For example, tasking observations of a specific RSO at specific times are not feasible. The qualitative metrics of any specific observation are also not always reliable or consistent. However, these are already proven capabilities of the current state of SDA. The STC network instead offers several advantages. It offers a decentralized and geographically distributed method of continuously collecting vast amount of data to move towards a search-based SDA. The STC network facilitates the observation of conjunction events, near-misses, parasitic satellites, and nefarious activities, which would otherwise be missed by the task-based SDA approach. The STC network does not replace or outperform any specific SDA instrument, instead it offers a novel perspective on the events in LEO. The large volume

of data collected by the STC network has the potential to improve satellite re-visit times, overall volumetric coverage, RSO optical characterization, and orbit propagation models. Upgrades such as multispectral imaging can also improve RSO characterization [103]. These upgrades can be achieved by designing payloads of various size gradients. Payloads of various sizes, defined mostly by the aperture size of the camera, can be adopted to fit on as many satellites with capacity. Another notable source of star field images is a star tracker. In many cases satellite already carry several star trackers and posses the ability to downlink these images. A practical verification method of the results obtained using ViCAS can be achieved using star trackers. Procurement of a star field image data set is recommended as part of the future work.

To enhance SDA capability in LEO, we need to leverage large constellations with STC in order to achieve sub-hourly revisit rates, perform optical characterization of RSO smaller than 1 m, and transition from a task-based to a search-based surveillance approach. These improvements will enhance the lacking accountability of events in orbit and enable the users of the space environment to directly provide data that improves the state of awareness. The simulator built for this research shall further be expanded with additional functionality for proof of concept and is a novel contribution in this area of research.

4 Chapter Four: Image Processing Framework for the Space Traffic Camera

In this chapter, an automated image processing framework is outlined for the large volume of star field images collected from the STC network. Of key interest is adaptability to varying camera specifications, processing speeds and characterization accuracy. The work presented here has the following objectives:

- Determine detection sensitivity possible with available data for training and validation. The objective is to understand how many STC detections from Chapter 3 can be actualized.
- Identify and extract key astrometry and photometry features.
- Evaluate STC image capture mode(s) that capitalize on extracting astrometric and photometric characteristics.
- Develop an automated framework for star field image processing which is adaptable to camera hardware.

4.1 Mechanics of Observation

This section describes how images of RSO are captured in context of the imaging instrument and passive observation strategy. The discussion includes impact of noise sources, observer angular motion and RSO photometric properties. Also described are metrics used to evaluate the image processing algorithm and it's performance.

4.1.1 Star Field Images

The study of astrophotography has been standardized over many decades of research. Digital astrophotography produces, analyzes and records some of the largest quantities of data. The fundamental principles of this practice remain unchanged. The objective is to collect photons using an opening, or aperture, and focus the light onto an imaging sensor. Technologies such as charged-couple device (CCD) and complementary metal-oxide semiconductor (CMOS) have greatly advanced the capabilities of digital photography [104]. These advances have led to the development of the star tracker as an attitude determination instrument commonly found on satellites [69]. Photons collected by the aperture are spatially divided into bins or pixels. The size of the pixel, usually measured in micrometers, and the number of pixels divide the total amount of light that enters the aperture. The number of photons collected in each pixel registers a data number (Dn) value. The Dn value for each pixel is stored as an 2-dimensional array, which is the raw digital image.

Bright and distant stars appear like point sources of light on a star field image. The angular size of a star the size of our sun at 1 light-year is approximately 3×10^{-2} arcseconds. For comparison, the Hubble space telescope's pixel resolution is estimated at 5×10^{-2} arcseconds [105]. The pixel resolution is also referred to as the instantaneous field of view (IFOV). The FAI's IFOV is 365.6 arcseconds, and a commercial star tracker's IFOV can range from 9 to 45 arcseconds. For an ideal optical system, all the light from the star would be contained within one pixel, even for Hubble. However, in the non-ideal case, optical systems are incredibly sensitive to temperature fluctuations, mounting errors, misalignment [106] and charge overflow[104]. Additionally, the impulse response function of an imaging system, defined as the point spread function (PSF), transforms the point-like angular size of a star into a diffused "blob". Illustrations of the types of PSF shapes possible is outlined in Figure 4.1 below. The PSF is typically modeled as a 2-dimensional Gaussian; however, shapes can vary significantly for various optical systems. Some illustrations include positive and negative spherical aberrations, which form airy disks with equal and unequal axis scaling. Defocused PSF examples are also shown.

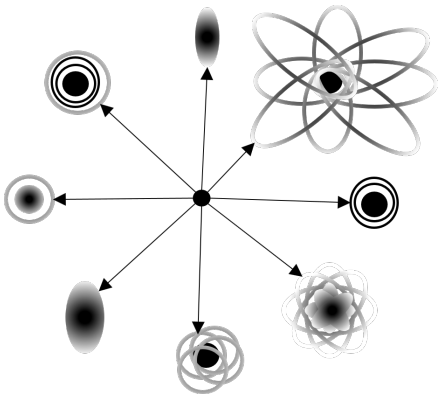

Figure 4.1: Various types of point spread function transformations

The 2-dimensional Gaussian, $g(x)$, is modeled using Equation 4.1 [107]:

$$g(x) = \frac{1}{\sigma\sqrt{2\pi}} e^{(\frac{-(x-\mu)^2}{\sigma^2})} \tag{4.1}$$

where σ represents the standard deviation and μ represents the mean. In this dissertation, the centroid of the object is a reference to localization of the object on the image, which refers to the combination of the x and y axis mean or μ.

When detecting an RSO, the PSF is integrated over the angular displacement (δs) of the RSO. An illustration is shown in Figure 4.2 below. For a non-tumbling host spacecraft, the stars and RSOs on a star field image drift at different angular velocities. Stars provide the reference frame for an attitude determination system, and tend to drift a negligible amount over short exposure times. The range of relative orbital velocities between two RSOs in LEO can range from few meters per second to 20 kilometers per second. During an exposure time of 0.1 seconds, the relative displacement of an RSO can reach up to 2 kilometers. The angular displacement (δs) of an RSO in a sequence of images depends on the distance between the STC and RSO. The PSF transformation applied to such an angular vector produces a streak spread function (SSF). In Figure 4.2 the area of effect, shown at 2σ, is significantly larger for the orange streak compared to the blue streak. On the bottom of the figure, a sequence of image snippets of an RSO captured by the FAI are shown at an interval of 1 second and exposure time of 0.1 seconds. The distance between the center of adjacent pixels in the vertical and horizontal direction is 1, and $\sqrt{2}$ in the diagonal.

Due to this, a pixelated PSF transformation creates a plus-like (+) symbol. It is important to note that the PSF model loses accuracy when the object brightness saturates the pixel's charge well, and the charge overflow occurs primarily from the saturated pixels into the vertical direction (up and down the column).

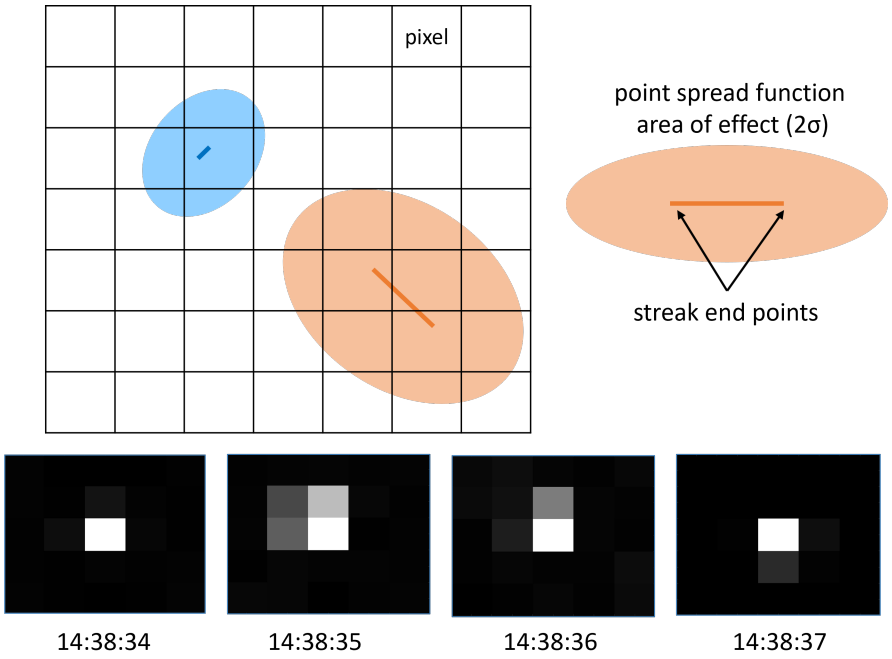

Figure 4.2: Differences between streaking and non-streaking objects on star field images

4.1.2 Signal-to-Noise Ratio (SNR)

As discussed in the previous chapter, the detection sensitivity of an RSO depends on the SNR. There are two methods of computing the SNR of an object using Equation 2.4, SNR_{bp} and SNR_{ap} [43]. SNR_{bp} represents the ideal scenario where signal and noise are aggregated in one pixel. SNR_{ap} defines the signal and noise on a defined contiguous set of pixels of various shapes (Figure 4.2). The shape of the synthetic aperture is often defined as a circle, square or rectangle. For ViCAS, a square aperture with a side length of 7 pixels is chosen. As derived from FAI characterization report [108], 7 pixels is the approximate full width at base (FWB) for the PSF. This knowledge defines an ideal filter size for the synthetic aperture in this research. In this manner, the signal to noise ratio threshold for a detection algorithm can be evaluated and optimized for sensitivity.

4.1.3 Imaging modes

There are 3 types of attitude control profiles on host satellites for the STC payload to expect. Tracking refers to maintaining an attitude to position RSO(s) at a spatially fixed point in the image sequence [109]. Sidereal tracking is when stars are spatially fixed. Finally, stare or undefined profile refers to a state where neither stars nor RSO(s) appear constant in the image sequence. The STC is defined to operate in both active (tracking) and passive (stare) modes, due to it's dual purpose applicability as a star tracker.

A key consideration for RSO detection and characterization are the imaging modes. The imaging modes refer to a predefined subset of possible states the camera can capture images in. Table 4.1 outlines some basic examples of the parameter values considered for passive optics. The δs values described in Table 4.1 are STC extremities. Imaging modes are often defined based on instrument constraints, like power, thermal and bandwidth, and application requirements. For star trackers, an exposure time of 0.1 second is enough to detect stars of magnitude 6 or brighter. The duty cycle refers to the utilization efficiency of the instrument, where the maximum frame rate for a 0.1 second exposure is 10 Hz at 100% duty cycle. At 50% duty cycle, that yields a frame rate of 5 Hz. Burst mode is defined as an ideal setup for the STC, where the maximum amount of information from a star field image can be extracted. For comparison, the duty cycle used for ViCAS is also listed.

Table 4.1: Example imaging modes of a space traffic camera

	burst	ViCAS	star tracker	terrestrial
exposure (seconds)	0.1	0.1	0.1	5-15
RSO δs at 300 km	0 - 0.38°	0 - 0.38°	0 - 0.38°	N/A
RSO δs at 1000 km	0 - 0.11°	0 - 0.11°	0 - 0.11°	N/A
maximum frame rate (Hz)	10	0.1	1 - 5	0.2 - 6.7×10^{-2}
duty cycle	100%	1%	$10\% - 50\%$	100%

Even for short exposure times, the maximum angular displacement (δs) of an RSO can exceed several pixels. Since RSO detection depends on the SNR_{ap}, the number of pixels occupied by the RSO is irrelevant towards detection sensitivity. The number of pixels considered as part of the synthetic aperture depends directly on the RSO's angular size and the PSF properties of the

imager. However, a longer exposure time impacts the minimum range of characterizing an RSO. If the exposure time is too large, the RSO may enter and or exit the field of view of the camera during the exposure. Without knowledge of the length of the streak, characterizing RSO for astrometric applications becomes impossible. Therefore, shorter exposure times are preferred [110].

Long exposure times also compound two more sources of data corruption. First, the host spacecraft attitude must be determined to deconvolve it's effects on the RSO angular displacement measurements. Secondly, the host spacecraft's positional displacement causes a parallax distortion on the RSO angular position as well. For shorter exposure times, the attitude and parallax displacement deconvolution can be simplified using a linear estimator, whereas for longer exposure times, a non-linear estimator is required.

4.1.4 Auxiliary Data

In addition to images, auxiliary data plays an instrumental role for both photometry and astrometry applications. Information such as attitude and rate of the host spacecraft, position, velocity and time (PVT) are key in developing SDA applications using the STC network, and these are referred to as the ephemeris data. The ephemeris data can be independently collected by the STC payload using a suite of sensors which will be further discussed in Chapter 5. The FAI data set was chosen for this research as images were tagged with ephemeris data.

For SDA applications, no labeled and standardized optical data set exists. This research aims to be a motivation for such a data set. Following is a brief summary of the labels that are highlighted in this research and from previous works [32][74] as aspirational ground truth labels.

1. Characteristics of all RSOs in image
    - centroid. The x and y pixel values for the starting and ending position of the streak of the RSO over the duration of the exposure.
    - full width half max (FWHM)
    - relative position and velocity (relative to host satellite)
    - RSO orbit. Usually defined as a two-line element (TLE) or covariance matrix
    - NORAD Catalog ID

- RSO shape and optical reflective properties
- RSO attitude and rate

2. Characteristics of all Stars in image
   - star identity. A star catalog stored in memory can be referenced using the ID to determine visual magnitude and right ascension (RA) and declination (DEC).
   - centroid. The x and y pixel values for the centroid of the star on the image.
   - FWHM
3. Ephemeris of the host satellite
   - position
   - velocity
   - time

This research leverages data set from previous simulation efforts [32][74] for training and validation purposes, referenced to as the space-based optical image simulator (SBOIS). The simulator provides the auxiliary data to independently develop algorithms to estimate the characteristics deemed relevant for SDA.

4.2 Image Processing

To develop a robust image processing algorithm, a large training data set is required. The labeled simulated images can be adopted for training and validation; however, the unknown PSF shapes and sizes of various camera systems introduce sources of error. Therefore, the Gaussian PSF model is used as a standard template to generate the initial set of training images.

4.2.1 Synthetic Macro Generator

The synthetic macro generator (SMG) is a data set generator which produces images specifically for training. Similar methodologies have been studied previously [82], and have demonstrated promising results. The SMG creates a data set based on a set of predefined camera parameters. The SMG designed for this research uses exposure time, pixel size, quantum efficiency, field of view and Dn resolution as functional inputs. These inputs are used to calculate a range of expected

outcomes with regard to streak sizes, object brightness, and aperture size as discussed in the previous section. Using the SMG as per FAI specifications, the ideal aperture is a 7 pixel square, which complements the 7 pixel PSF from characterization report [108]. The data set generated by the SMG is referenced as FAI_{syn}, from SBOIS as FAI_{sim} and real images as FAI_{real}. The labeling for FAI_{real} was done using the Astropy python package's PSF characterization function.

Table 4.2 below outlines the range of parameter values used for creating synthetic data set using the Monte Carlo simulation method. All combinatorial variations of the provided parameters are used to create a randomly indexable data set with the labels that generated them. The values are provided in pixels referenced to the FAI, however the functions are adapted to the camera specifications provided. The noise values are adopted from dark frames observed from FAI_{real}.

Table 4.2: Range of parameter values for creating the FAI_{syn} data set

	min	max	steps
centroid (pixel)	-0.5	0.5	20
PSF σ (pixel)	0.05	2.56[108]	20
δs (pixel)	-0.5	0.5	20
read noise [108]	7.5	40	20
noise (% of pixel data resolution)	1	10	100

4.2.2 RSOnet: CNN architecture and training

A CNN architecture was designed to accompany the SMG to create a tool with the ability to adjust training parameters shown in Table 4.2. RSOnet is referenced as the image processing algorithm. Figure 4.3 summarizes the training process where the arrows represent data adaption and transfer for the next step. The diagram origins at the green SMG block, where a data set is created called the synthetic image bank. This data is used to train and test various CNN architectures for their performance. When one design is selected, it is tested against the real and simulated data set for verification and performance characterization. These results are used to update the SMG generator parameters to improve image generation to match the specific optical features of the real data set.

The CNN for RSOnet consists of 3 convolutional layers followed by a fully connected layer. A convolutional layer is composed of convolution filters that when applied to a training dataset, assist

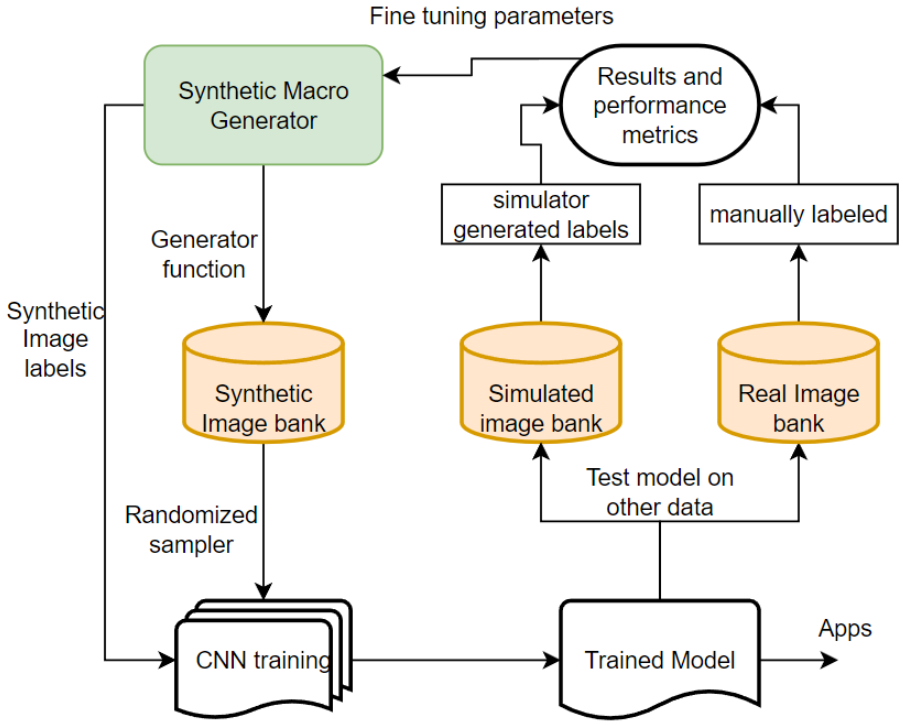

Figure 4.3: CNN training method

in training the spatial dependencies of objects. A fully connected or dense layer is feed-forward neural network that is fed the output of the convolutional layers to train for patterns in convolution filter activations for identifying objects in an image. The CNN architecture is shown in Figure 4.4.

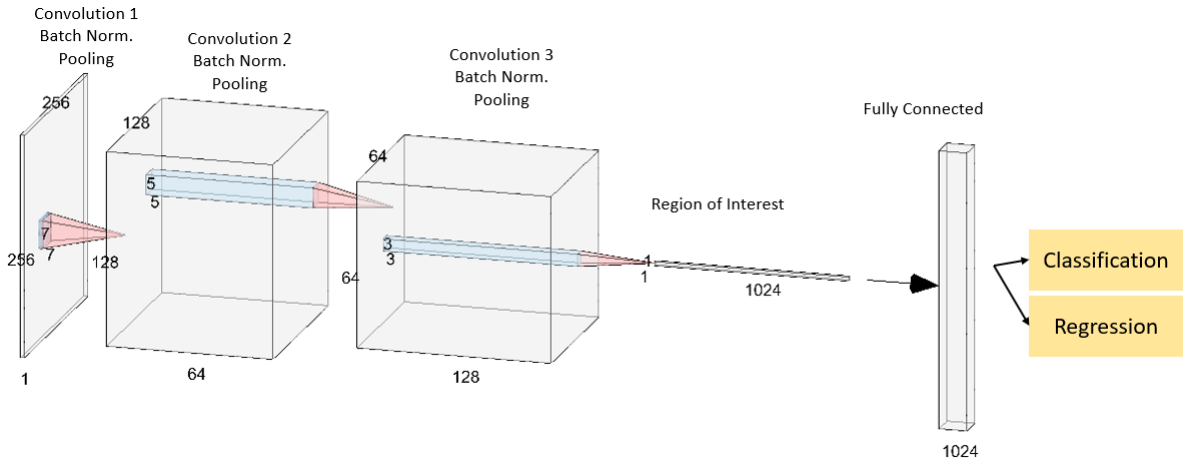

Figure 4.4: CNN architecture and it's outputs

The output of the neural network was split for classification, classification confidence and regression using softmax, sigmoid and rectified linear activation functions, respectively. The two

classes are detection and non-detection. Regression involved prediction of PSF features provided to SMG for image creation. They key outputs from processed images are features of a digitized 2D Gaussian distribution such as mean, standard deviation and photon count which are utilized by the SMG. The results of this training are shown and discussed in section 4.3.

4.2.3 Tracking and classification

Detected objects are then classified into stars, RSO or others during the tracking process. In wide field of view star field images, there can exist hundreds of potential detections with varying angular motion. Groupings of angular motion separate stars from RSO. To perform multi-object tracking (MOT), detections from a processed image sequence are used to create a k-partite graph layout (directed acyclic graph), where k is the total number of images processed [111][112][113]. In this layout, each detection acts as a node and no edges connect detections from the same frame. There is a start node, end node and a detection node. The detection node is further split into nodes u and v. An example graph is illustrated in Figure 4.5. The graph is then simplified by using a distance limit of 20 pixels between two frames to reduce required computation.

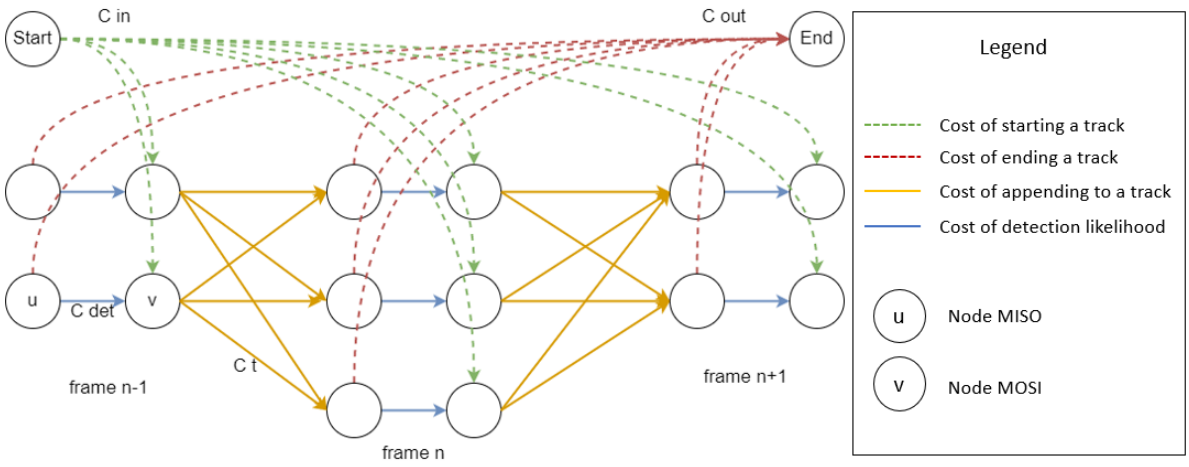

Figure 4.5: Multi-partite graph layout for multi-object tracking

The objective function is described below in Equation 4.2 as T. There are four cost functions associated with the objective function to track the motion of an object detected in multiple consecutive frames of a sequence. The first function is the cost of a tracking edge, defined by C_t, which is based on polynomial curve fitting metrics, with maximum polynomial order of 1. The cost of

the tracking edge depends on the distance d traveled between the two nodes of the edge and the variation in the brightness b of the object. The second and third functions are the cost of starting a new object track and track termination, as defined by C_{in} and C_{out} respectively. Finally, C_{det} defines the cost of detection, which is the negative cost associated with detection probability. B_i refers to the probability that the detection is false. f defines the corresponding indicator function which identifies which nodes are connected by taking on a binary value 0 or 1. Starting and ending cost functions provide connectivity to all nodes of the graph to ensure tracks can be started and ended at any point during the sequence due to detection discontinuity. Both the start and end cost functions are designed to preserve track flow conservation and are a fixed value. Flow conservation ensures that the inflowing indicator function adds up to the out-flowing indicator function which is between 0 and 1. Flow conservation allows the graph solving algorithm to determine the lowest cost approach to start, traverse and end object tracks.

$$T = argmin \sum_i C_{in}(i) f_{in}(i) + \sum_{i,j} C_t(i,j) f_t(i,j) + \sum_i C_{det}(i) f_{det}(i) + \sum_i C_{out}(i) f_{out}(i) \tag{4.2}$$

$$\text{where} \qquad C_{det} = log \frac{B_i}{1 - B_i}, \qquad \text{and} \tag{4.3}$$

$$C_t = \sum_{i,j} d(i,j) + b(i,j) \tag{4.4}$$

The track of an object is classified into celestial objects, RSO and noise.

4.3 Performance Evaluation

In this section, the performance results of the model are discussed. The metrics of evaluation include accuracy of classification, detection and characterization.

4.3.1 RSOnet Performance

Evaluation of the CNN and training process is demonstrated with precision and root mean squared error (RMSE) during the training process. 50 epochs of training were performed to have a high precision for the training data and a significant improvement against the validation data. Stopping training at 50 epochs avoided over-fitting to synthetic data set, which in turn yielded better performance against simulated and real data set. RMSE values for regression had achieved desired PSF mean accuracy of 0.02 by epoch 30. Several combinations of the SMG, SBOIS and real FAI data set were attempted for training. The training data set was obtained from the SMG and SBOIS [74] and FAI, at a shuffled split of 40-20-40, respectively. The overall training and validation data split was also at 80-20. The training precision and loss are shown in Figure 4.6. Approximately 7 million object instances were used during training and validation with varying noise levels, object brightness, object PSF-shapes, and motion vectors. In future efforts, an autoencoder and decoder architecture should be adopted to minimize the training data labelling bias. However, important considerations need to be made to ensure star tracker functionality remains possible on-board the satellite.

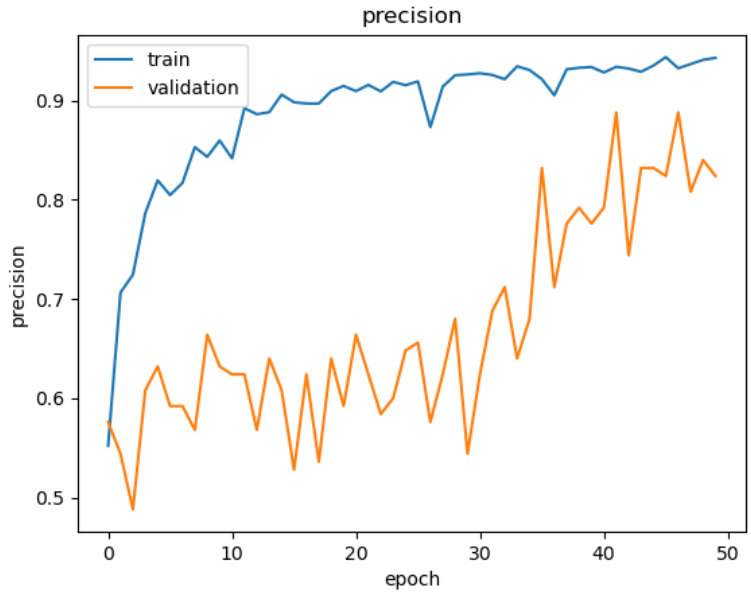

(a) Precision

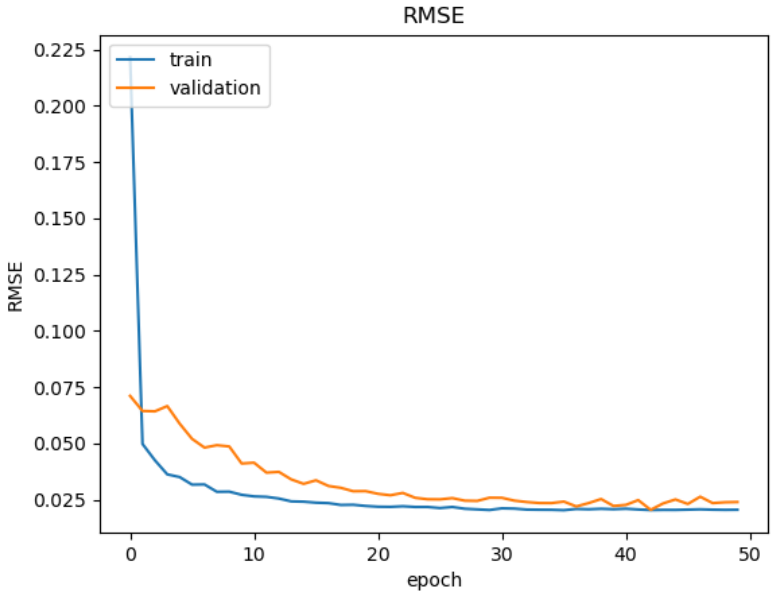

(b) RMSE

Figure 4.6: CNN training evaluation

The accuracy of the CNN is measured against synthetic, simulated and real images for comparison. Object detection accuracy is measured by looking at the ratio between the sum of true positives and true negative to the sum of all four possible outcomes, only for objects with a SNR above 6. As expected, the detection accuracy of the network drops against simulated and real images. The accuracy of detection against the real data set can certainly be improved provided a real labeled data set is folded into the training process. Object characterization is demonstrated with mean squared error (MSE) and RMSE for mean, standard deviation and photon count against synthetic and simulated data. The results are summarized in Table 4.3. The regression accuracies of the PSF mean or object centroid, PSF scale or object angular size and photon count have significantly better performance with the synthetic data. This drop in accuracy is reflective of the apparent differences in the three data sets considered. The accuracy values for each data set are also limited by the labeling method. In the SMG training images, faint objects that might otherwise be undetectable, generate a false flag throwing off the accuracy. The loss in accuracy is persistent even for images from SBOIS. Additionally, in the real FAI images, the RSO labels are highly inconsistent and may not include fainter RSOs that would be detectable. A fundamental limitation that primarily affects the PSF characterization accuracies of FAI_{syn} is the instantaneous field of view of the FAI.

Table 4.3: CNN accuracy results in pixels after 50 epochs against three data sets

	FAI_{syn}	FAI_{sim}	FAI_{real}
Object detection	92%	83%	88%
PSF mean (MSE)	5×10^{-4}	4×10^{-2}	0.2
PSF scale (RMSE)	4×10^{-2}	0.11	0.15
Photon count (RMSE)	7×10^{-2}	0.1	0.1

The PSF modeling effort in [82] yielded a PSF mean of $0.784 \pm 1.561 \times 10^{-3}$ and $0.931 \pm 1.987 \times 10^{-3}$ for x and y axis, respectively. RSOnet achieves a marginally better accuracy, however the results are not directly comparable. The training data parameters, their range and the data set used for training and validation are not identical. However, a similar training process, using SMG, generated nearly equivalent results. Furthermore, the PSF scale, or full-width half max (FWHM), for [82] is marginally better than RSOnet at $0.26 \pm 11 \times 10^{-3}$. The likely factor is that RSOs considered during the training data generation process have an angular velocity component, which directly affects the network's ability to resolve the true angular size.

When compared to the PSF-fitting method, the CNN designed and trained in this study resolved images 44% faster. The PSF-fitting method achieved a centroiding accuracy of 0.17 on real images, which is marginally better than RSOnet. However, the biggest advantage of RSOnet is the SNR cutoff, which was defined at 6 dB compared to 18 dB for PSF-fitting for this data set. PSF-fitting has demonstrated 4 dB SNR on other astronomy data set [114], however, RSOnet was trained using custom data set generated by the SMG specifically built for the FAI sensor. The combined SMG and RSOnet training process ties hardware specifications to algorithm performance in wide FOV camera sensors, and also making it a transferable and modular framework. Figure 6 below shows the filter responses for objects detected on a set real FAI images, one with a lens flare. Figure 6 below and Table 1 above demonstrate the resiliency of the RSOnet CNN to detect faint objects and handle noise real images due to synthetic data training.

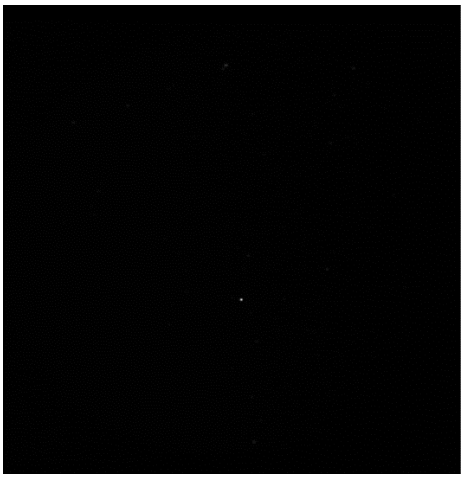

(a) Real FAI image

(b) CNN filter response

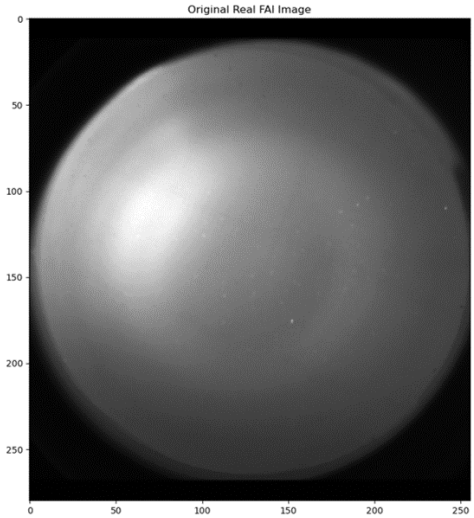

(c) Lens flared FAI image

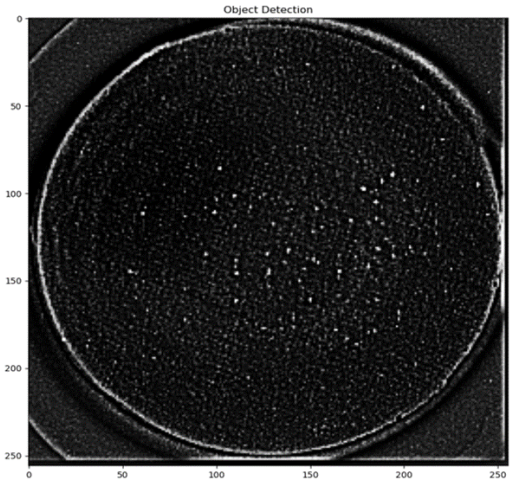

(d) CNN filter response

Figure 4.7: RSOnet on real FAI images

For evaluating object class identification, accuracy of each class is shown in Table 2 from the graph-based tracking results. RSOnet's graph-based MOT implementation shows promising classification results and can certainly be improved with real data. Previous efforts use a stacking or streak characterization approach for classification problems. The closest comparison is made to [115], which studies GEO object tracks over long exposure images.

Compared to [115], RSOnet-derived MOT implementation achieves a lower classification accuracy and precision, but a comparable recall value. In the compared literature, GEO objects traverse the imager's field of view at a slower speed than for RSOnet's FAI images. Additionally,

Table 4.4: Tracking and classification performance metrics

	Star	RSO	Noise
Accuracy	84.2%	68.1%	32.6%
Precision	81.1%	60.4%	25.8%
Recall	98.5%	95.6%	30.0%

the algorithm has to differentiate between stars, which are small streaks, and GEO objects, which are long streaks. In case of FAI and RSOnet, the algorithm has to first generate the best tracks to append together into a comparable tracklet. The track proposal is based on shortest distance, however that is not always accurate given eclipse scenarios. Despite differences in image type, data set and algorithm, the performance of RSOnet demonstrates classification for a multitude of object from low exposure, high frame rate image sequences.

Further improvements based on more accurate labels can improve RSOnet's detection and classification accuracy. Some of these improvements should target the failed cases as follows. The most common failed case for detection occurred at the edge pixels, when an object was entering or exiting the field of view. A mean padding was applied to convince the algorithm that the additional pixels were background noise. Average padding is used when a sliding window filter reaches the edge of the image, where additional pixels are appended using an mean value of the image. This failure is likely caused when a significant portion of the PSF shape is abruptly replaced with values that don't always correspond to the local background noise. The two possible corrections are to avoid padding to ignore the edge objects and ensure the entire circular field of view is contained within the image frame. The FAI images did not suffer from this failure mode as the entire circular field is encompassed on the image frame as seen in Figure 4.7(c).

Another common failure mode occurred during the MOT classification step and relates to the occultation event where one object merges or overlaps with another object. Nearly all the failure cases consisted of an RSO crossing over a star, with the image processing step yielding 1 detection for two objects with inaccurate centroiding. The most efficient way to resolve this failure case is to provide large number occultation examples during training and to evolve the MOT classification metric beyond using just closest distance.

It is far easier to track and classify stars than RSO because of their coordinated motion and

non-fluctuating visual magnitude over the course of an image sequence. RSO on the other hand tend to cross paths with other RSO, star and noise, making it harder to classify RSO accurately. In terms of classifying noise sources like hot pixel, shot noise, Earth's limb and the moon, the vaguer definition of noise for the CNN makes for a more difficult classifier. Hot pixels are the easiest amongst the noise to classify because the same pixel is being activated continuously throughout an image sequence. In future work, attempts should be made to tie real verified detections using an orbital propagator. In this method, the RSO catalog information is used to pair a detection to an orbital track to verify if the RSO sequence detected by the imager is a true positive [92] [93].

4.3.2 Summary

The PSF mean accuracy of RSOnet is outlined in pixels and not acrseconds to provide the adaptability to various star-tracker like imagers. For the 256×256 pixels of an FAI image, an accuracy of 0.2 pixels represents 73 arcseconds. Whereas a similar telescope with a higher resolution imager, like a wide FOV camera, at 1024×1024 pixels could represent up to 18 arcseconds accuracy. Similarly, the detection sensitivity of RSOnet on FAI image sequences is 9. Magnitude of 9 is not enough to detect objects in geostationary orbit, but is possible for objects less than 1000 km away in LEO. As predicted, these are qualitatively a worse measurement than the NEOSSat imager with 2.3 arcseconds accuracy. The lower accuracy can largely be attributed to the smaller aperture size and worse image resolution on the FAI. Star trackers have a narrower FOV and better image resolution comparable to FAI. It can be estimated that cross-track accuracy of 15-38 arcseconds can be achieved with a standard COTS star tracker [116]. Table 4.3 below provides a summary of the accuracy using FAI, COTS star tracker and NEOSSat. It is important to note that not all observations can be made at the defined accuracies, and they represent the best case scenario of each sensor. For typical observations, the cross-track accuracies can drift into the kilometer range. The results indicate that the algorithm introduces minimal error to the astrometric measurements compared to attitude determination efforts which is measured to be greater than 100 arcseconds for the FAI imager, validated with the Astrometry tool-kit.

One of the primary limitations of a passive optical instrument is estimation of radial accuracy. A common application of passive optical instruments is in the use of custody operations, where a known and expected RSO is intentionally tracked and the catalog is updated accordingly. The

Table 4.5: Cross-track accuracy of RSO detections by optical sensor

	FAI	COTS star tracker	NEOSSat
Cross-track accuracy (arcseconds)	73	15-38	2.3
Error (m) at 300 km range	100	20 - 60	3.3
Error (m) at 1000 km range	350	70 - 180	10

cross-track accuracy is used to determine relative cross-track velocity, which can be used to refine RSO ephemerides. In case of discovering new RSO, the passive optical instrument suffers from poor radial accuracy. In this research, the radial accuracy, or simply the displacement between the host satellite and the RSO can be computed by accumulating multiple STC detections. Moreover, quantitative multi-site observations have the potential to improve the overall accuracy of the RSO astrometry using joint probabilistic data association (JPDA) [10], which will be explored in future works. Another method of compression analysis is using the autoencoder method, where a convolution-deconvolution architecture is trained to improve compression and performance using unsupervised learning. This should be considered as part of future work and viable for a non-star tracker implementation.

5 Chapter Five: Experimental Results and Contributions

This chapter of the dissertation describes the results of various experiments, functionality of a prototype payload, and possible contributions to SDA. The RSOnar mission is described in this chapter as the primary experiment to validate results from Chapters 3 and 4.

5.1 RSOnar Mission Overview

Resident space object near-atmospheric edge reconnaissance (RSOnar) mission represents the experimental validation of the research discussed in this dissertation. The scope of the mission was to demonstrate the dual-purpose star tracker functionality critical to the success of a STC. RSOnar was designed as a 2-U CubeSat payload on a sub-orbital flight of a stratospheric balloon. As a critical member of the mission team, my contributions include defining the scope of work, mission design, project requirements, success criterion, project scheduling, test plans, field campaigns, prototype and flight hardware development, sub-systems design of software, firmware, electrical hardware systems, post-launch data analysis and report writing.

The mission objective was divided into three categories of work, RSO detection, tracking and characterization. A summary of the objectives are shown in Table 5.1 below. The table summarizes the RSOnar mission objectives, along with their corresponding minimum, expected, ideal, and achieved outcomes. The mission objectives are RSO detection, RSO tracking, and RSO characterization. The minimum objective for RSO detection is to detect at least one RSO per hour with an average detection duration of at least one second, while the ideal objective is to detect at least ten RSOs per hour with an average detection duration of at least 30 seconds. These estimates

were made as part of the initial systems design review by simulation. The achieved outcome is nearly ideal with detection of 69 RSOs per hour, and an average detection duration of 23.5 seconds. For RSO tracking, the minimum objective is to accurately determine the centroid of the RSO and classify it with the star with an accuracy of at least 65%, while the ideal objective is to accurately determine the centroid of the RSO and classify it with the star with an accuracy of at least 90%, with a centroiding accuracy of up to 1.5 arcseconds. The achieved outcome is a centroiding accuracy of 6.3 arcseconds, with a classification accuracy of 92%. For RSO characterization, the minimum objective is to identify 80% of the RSO detections, while the ideal objective is to identify 95% of the RSO detections and estimate the RSO attitude with an accuracy of up to 10 degrees. However, the achieved outcome is the identification of less than 24% of the RSOs. Overall, the mission is considered a partial success and validates the high volume observation hypothesis of this dissertation.

Table 5.1: RSOnar mission objective description

Objective	Minimum	Expected	Ideal	Achieved
RSO Detection	$\geq$ 1 detection per hour. Average duration of detection $\geq$ 1 second	$\geq$ 2 detections per hour. Average duration of detection $\geq$ 15 seconds	$\geq$ 10 detection per hour. Average duration of detection $\geq$ 30 seconds	69 detections per hour. Average duration 23.5 seconds
RSO Tracking	Centroiding $\leq$ 15 arcseconds. RSO and Star classification $\geq$ 65%	Centroiding $\leq$ 7.5 arcseconds. RSO and Star classification $\geq$ 75%	Centroiding $\leq$ 1.5 arcseconds. RSO and Star classification $\geq$ 90%	Centroiding 6.3 arc seconds. 92% classification accuracy.
RSO Characterization	Identify 80% of detections	Identify 90% of detections and size estimation accuracy $\geq$ 70%	Identify 95% of detections and estimate RSO attitude up to 10 degrees accuracy	Identified $\leq$ 24% RSO

The stratospheric balloon launched from Timmins (Ontario, Canada) on the night of 21^{st} August 2022 until the early morning hours of 22^{nd} August for a total flight duration of 13 hours. The flight reached a maximum altitude of 37 kilometers at approximately 2 am local time and remained

there until sunrise at 6 am local time and this was the key observation period for RSOnar. The payload weight was 2 kg without the interface plate to the gondola. After final integration, the power consumption was an average of 10 watts. An image of the integrated payload is shown below in Figure 5.1 (a). The payload chassis is covered in thermal insulation to avoid component damage from direct sunlight, with an opening for each camera lens. The primary payload is contained in the angled rectangular chassis section on the top in Figure 5.2 (b). The primary payload contains the camera, processor and power distribution unit that is evaluated in this research. The secondary payload is also a camera pointed at the horizon, and also acts as the support structure for aiming the primary camera at a 45° elevation angle. The secondary payload's electrical connections are separated from the primary and are not accounted for in the results presented here. The RSOnar payload is mounted onto an interface plate, which is fixed to the gondola frame. There was one electrical connection from the RSOnar payload to the gondola's power and distribution unit with a remotely controlled switch.

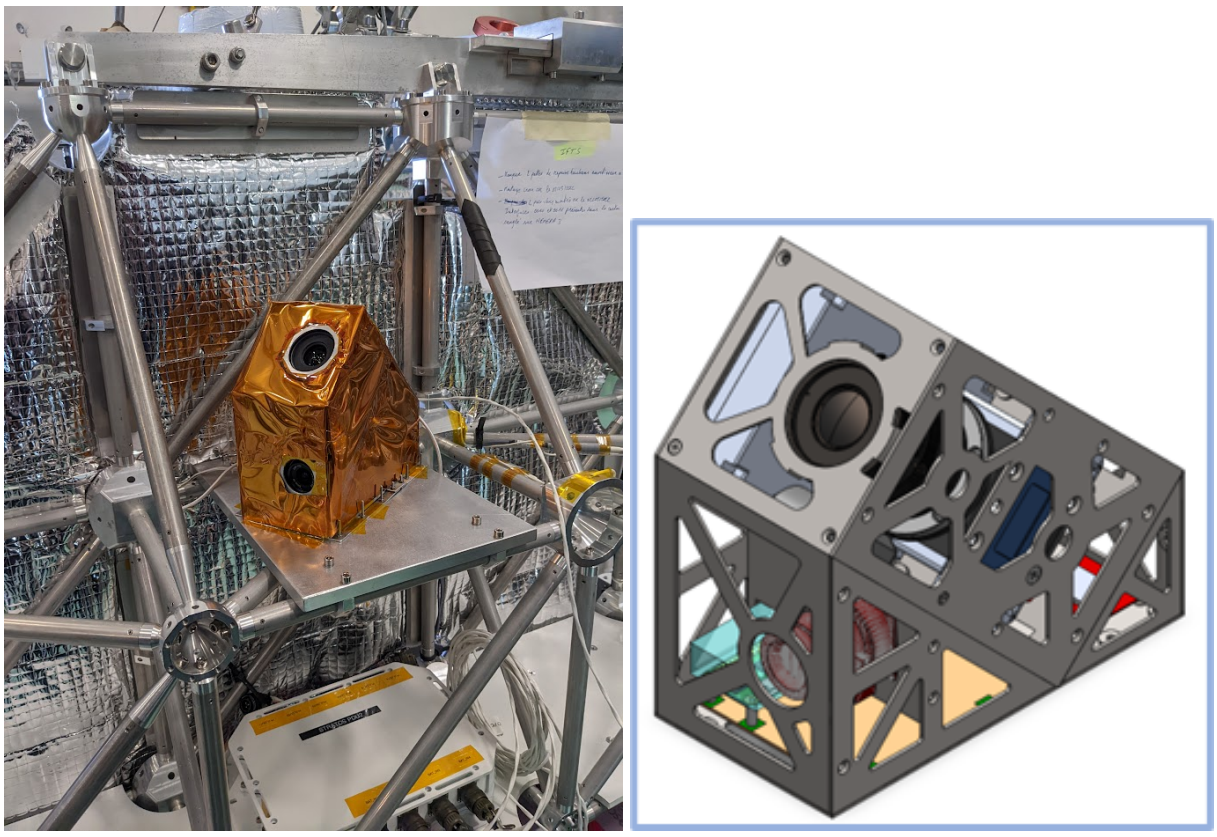

(a) Integrated payload (b) Payload model

Figure 5.1: RSOnar payload and model

5.1.1 Camera

The primary camera for the payload is a PCO Panda 4.2 mated with a ZEISS Dimension 2/25 optical lens. Figure 5.2 shows images of the camera components.

(a) PCO Panda 4.2 monochromatic [117] (b) ZEISS Dimension 2/25 [118]

Figure 5.2: Primary camera components

Table 5.2 provides a thorough comparison of the various cameras and their specifications considered in this research. GBO_{Ottawa} refers to the ground-based observatory located at the DRDC facility in Ottawa [119]. Celes-ZWO refers to observations of the Intelsat 10-02 and MEV-2 rendezvous at St. John's by Jim Johnston. DSLR refers to a Nikon 3500 camera used at various different locations. One of the key factors of considering the RSOnar camera is the IFOV, which has a direct impact on the cross-track localization accuracy of an RSO. IFOV is directly dependent on the field of view of the camera system. However, the trade-offs are such that a wide field of view camera can be used in a search and detect mode, whereas an imager like NEOSSat would require prior knowledge of an object's position. Thus, the RSOnar camera is considered suitable as both as a star tracker and a RSO seeker. Another key metric not described in the table is the exposure time, which for the smaller field of view cameras is generally higher. In many cases, the larger telescopes are used for tracking GEO objects, whereas the RSOnar camera is suited for LEO observations from ground, sub-orbital and orbital platforms.

Table 5.2: Camera specification summary

Characteristic	RSOnar	FAI	NEOSSat	GBO	Celes-ZWO	DSLR
Image resolution	2048^2	256^2	1024^2	2048^2	5496×3672	4948×3280
Field of view	21.2°	27°	0.8°	0.183°	0.52°	52°
IFOV (arcsec/pixel)	37	375	3	0.3	0.5	38
Aperture size (mm)	57	17	150	356	280	45
Pixel size (μm)	6.5	26	13	13.5	2.4	3.9
Bit depth (bits)	16	16	16	16	16	12
Quantum Eff.	82%	81%	94%	91%	84%	75%
Spectral Resp. (nm)	350-800	650-1100	350-850	400-870	400-770	450-850
Sensor type	sCMOS	CCD	CCD	CCD	CMOS	CMOS
Chromaticity	mono	mono	mono	RGB	mono	RGB
Altitude (km)	37	330-1408	776-792	0	0	0

Note: GBO_{Ottawa} refers to the ground based observatory in Ottawa, Canada on the DRDC campus [119].

5.1.2 Payload On-Board Computer and Concept of Operations

The payload on-board computer (POBC) refers to the primary processor hosting the operating system and the mission-specific concept of operations (CONOPS). For the STC payload, the CONOPS is designed to regulate power consumption, data management, states of operation, and communications. In digital communications terminology, the POBC is a slave with the host satellite being the master. This designation ensures that the primary mission of the host satellite is unaffected by the STC, making the STC a truly opportunistic payload. A representation of the POBC for the STC is conceptualized in Figure 5.3 below. In this setup, the camera is the slave device controlled by the FPGA. The image data is streamed to the FPGA memory where in a sequence of steps the image is formatted, processed with RSOnet and the output is transferred to on-board memory. The POBC block, which manages the shared data and control bus, dictates the flow of information based on the current state of operation. A skeleton state diagram in the POBC block illustrates some of the potential states the payload can exist in. In idle state, the payload is powered off and awaits instructions from the host satellite. In downlink state, the most suitable data is formatted into packets and streamed out of memory. Capture state is the agglomeration of multiple capture states that command the camera and FPGA to capture images. In safe mode, the system performs in a degraded state minimizing power consumption and data throughput. Finally, the program FPGA

state refers to over-the-air upgrades to RSOnet for improved performance. The upgrades and the data output will be discussed in section 5.2. Supporting instruments like the Global Navigation Satellite System (GNSS) receiver, sun sensor, inertial measurement unit (IMU) and temperature sensors allow for independence from the main payload. These supporting instruments are not only for redundancy, but also for accuracy improvements in measuring the pointing, keeping the optics safe from solar damage, accurate time stamping and monitoring the health and status of the payload. Not every STC variant requires such a suite of supporting instruments, as most host satellites generally carry these instruments.

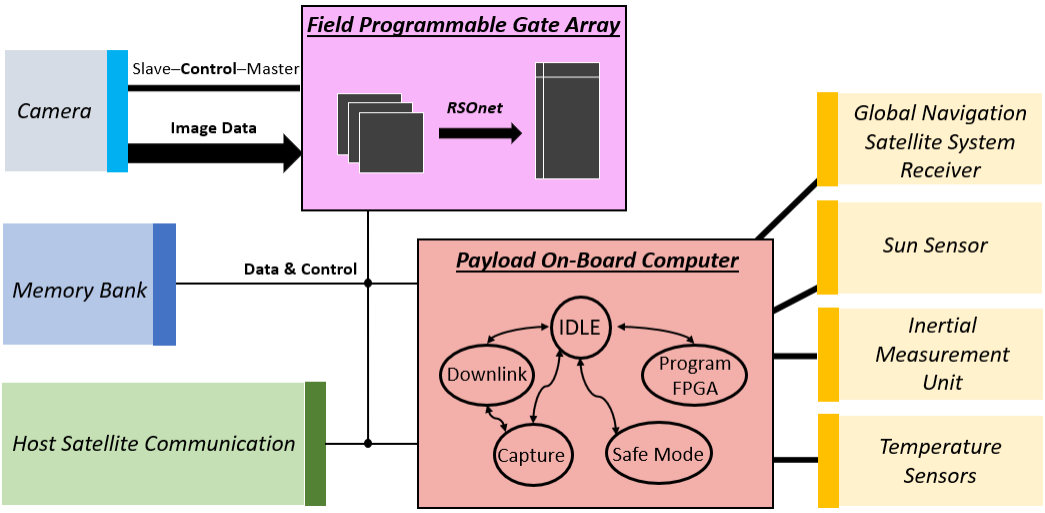

Figure 5.3: Payload Conceptual Description

For the RSOnar mission, the payload was simplified to perform passive data collection for post processing. The FPGA implementation was scaled down, and set of RSOnet image filters were implemented for in-situ processing. The camera control and data interface was done directly through the POBC processor, with the images directly stored in memory. The POBC images were also collected in only one mode, which simplified the CONOPS of the mission. Images were collected in bursts with a 4 second delay between each burst so as to not overwhelm the data rate capacity of the memory component. The exposure time was fixed to 0.1 second and the capture rate was 5 Hz. No sun sensor or IMU was installed as host gondola maintained a record of the orientation and position during flight.

5.1.3 Field Programmable Gate Array

In many applications image processing requires a dedicated processor hardware independent of the POBC. This independent processor hosts a control interface with the camera, and communication interfaces with the POBC and data storage drives. Three of the most common options are central processing unit (CPU), graphics processing unit (GPU) and field-programmable gate array (FPGA) [120]. Each option presents their own unique advantages and disadvantages, some of which are highlighted in Table 5.3 below. The relevant metrics for the STC payload include design flexibility, power consumption per computation cycle, cumulative efficiency of inference and design complexity.

Table 5.3: Comparing Hardware for Image Processors

	CPU	FPGA	GPU
Power Consumption	High	Low	High
Design Flexibility	High	High	Medium
Inference Latency	High	Low	Low
Design Complexity	Low	High	Medium

The FPGA is chosen as the best alternative based on the defined criteria. A reconfigurable or reprogrammable fabric enables in-field or in-orbit algorithmic updates for improved performance. Efficient inference, especially low inference time [120], enables faster processing and compression speeds for the overall payload performance. Handling higher data throughput at lower latency enables the payload to operate at more efficient duty cycles. The overall power efficiency of the payload also has a direct impact on duty cycle, thermal management, and quantity of data collected. FPGA-derived processors are flight proven [121], designed to be radiation tolerant and benefit from industry-accepted standardized development process [122]. Open source intellectual property (IP) cores enable integration of standard interfaces, algorithms, protocols and data management tasks. On the RSOnar mission, RSOnet convolutional filters processed a set of images from memory as a proof of concept. On future missions, real-time in-situ processing is identified as a key objective.

5.1.4 RSOnet for RSOnar

RSOnet is an image processing framework from which a custom solution is built to process images for a specific camera. As seen in Table 5.2, the hardware specifications vary greatly and no individual trained network is optimal for all the detection and classification tasks. The multitude of objects, optical effects, operational states and accuracies require a deep learning approach as the sizes of objects vary drastically. In this research, RSOnet is designed to optimize for detection, which requires adjustments to process images taken from imagers that vary in specifications from the FAI. Figure 5.4 below contain example raw images from each instrument discussed in Table 5.2. 5.4 (a) and 5.4 (b) are indistinguishable as the chosen RSOnar camera adopts FAI specifications and CONOPS, and is comparable to images produced on a star tracker. 5.4 (a) stacks 121 images from the RSOnar mission showing the motion of multiple RSO crossing the field. These images are captured on 22^{nd} August 2022 between 08:28:51 and 08:30:33 Coordinated Universal Time (UTC). 5.4 (b) stacks 51 images from the FAI showing how a similar effect is reproduced. These images are captured on February 9 2014 between 16:20:00 and 16:21:46 UTC by the FAI over the north pole. Figure 5.4 (f) stacks 28 images from the DSLR Nikon 3500 (with stock short lens) camera to produce RSO streaks comparable to RSOnar and FAI. These images were captured from Timmins Ontario on 15 August 2022 between 02:33:35 and 02:33:47 UTC. As concluded in Chapter 4, when using star tracker like imaging modes, spatio-temporal classification yields the most promising results.

NEOSSat image, Figure 5.4 (c), is a equivalent to a crop of the previous two images taken over a longer exposure time. Hence the grayer background and saturating light from one of the stars. GBO_{Ottawa} and Celes-ZWO, Figures 5.4 (d) and (e), are tracking RSO which appear as a PSF. The long streaks represent stars. In Figure 5.4 (d) GBO_{Ottawa} is tracking the satellite NEOSSat. Figure 5.4 (e) is taken by the Celes-ZWO telescope and it is tracking Intelsat 10-02 and can be seen as the right most PSF in the middle of the image circled in green. The other PSF objects trailing to the left are Meteosat 8, AMOS 3 and Eutelsat 5 coloured red, blue and yellow, respectively. The image quality and PSF characteristics of imaging using ground and space-based optics are similar regardless of location, and RSOnet has demonstrated detectability on these images. RSOnet's ability to detect PSF across various images without customization demonstrates its use-case as a

benchmark model for various optical instruments. Long streak detection and characterization is also possible with RSOnet, however, it is not a suitable architecture for this application.

In-situ processing of STC images using RSOnet requires further training to improve the accuracy and functionality. RSOnet is a benchmark framework upon which a real training data set can be applied for improved accuracy in centroiding and characterization. However, RSOnet is capable of object detection without any custom training. Using this object detection feature, macros of objects are extracted from the RSOnar flight images for training purposes. Any further training performed is a customized solution for that camera. Hence will be referred to as RSOnet$_{PCO}$ for the PCO camera and RSOnet$_{FAI}$ for the FAI imager. The primary reason for customized training solutions is hardware acceleration and optimized object detection. Using customized solutions for each STC variant can improve the adoption rate for the STC network, and enable a power and process optimized payload. If an optical imager is tracking, as in Figure 5.4 (d), then RSOnet$_{GBO_{Ottawa}}$ will have optimized filters for SSF and PSF detection and characterization. Future work should further train the RSOnet$_{FAI}$ base model, or equivalent, further with the autoencoder and decoder architecture. With autoencoder method, the newly trained custom model will adapt PSF features from the camera, as well as specific anomalies to that mission data.

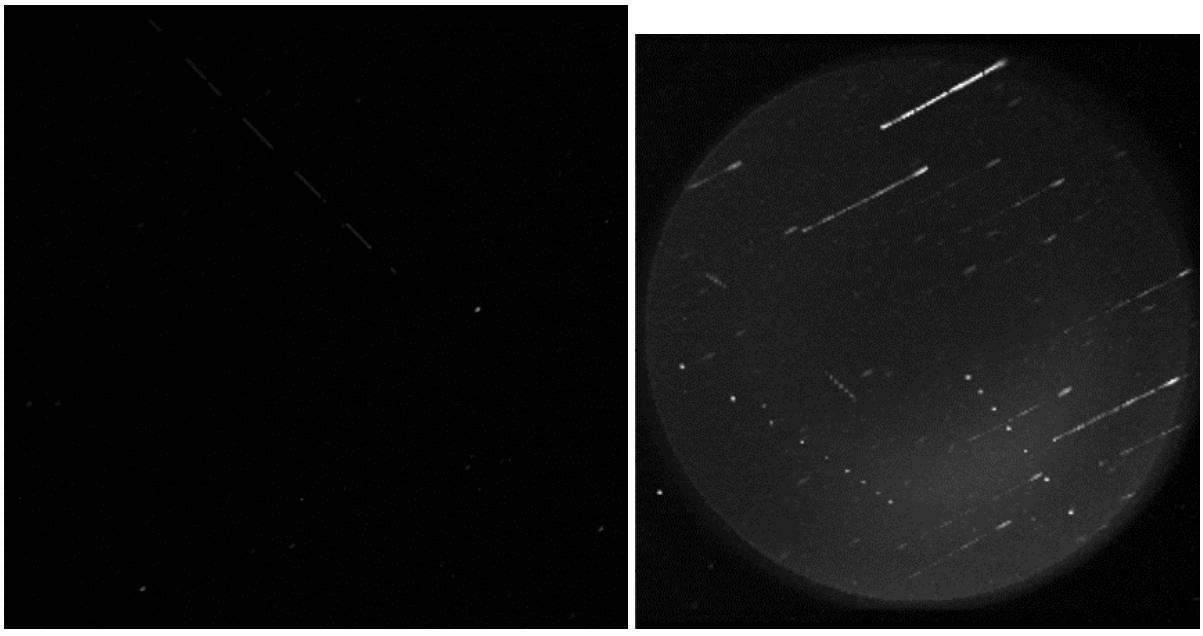

(a) RSOnar (b) FAI

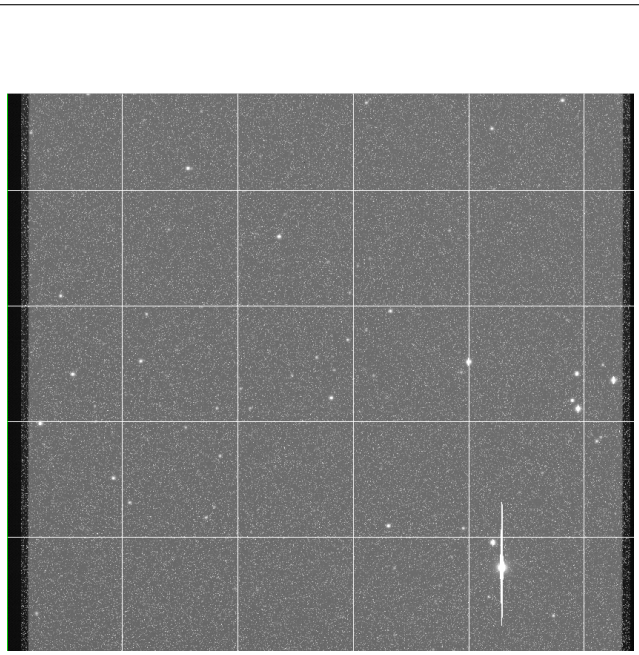

(c) NEOSSat

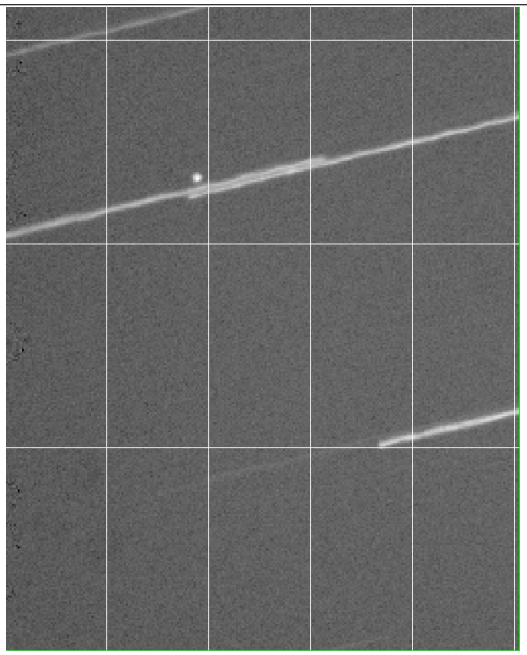

(d) GBO$_{Ottawa}$

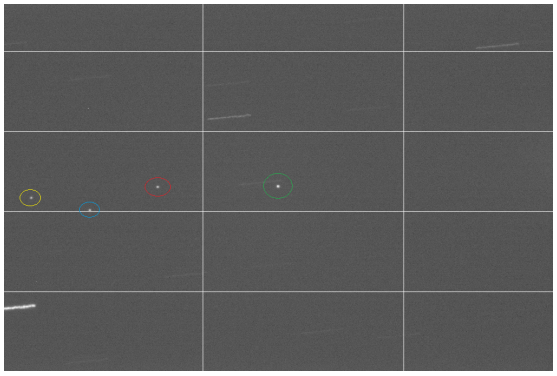

(e) Celes-ZWO

(f) DSLR

Figure 5.4: Example raw images from various cameras

An overview of this custom training method is highlighted in Figure 5.5 below. First the base RSOnet model is applied on real images. Using the detection, characterization and classification steps from Chapter 4, data extraction is performed. The data are used to produce more accurate labels for the real images using a tool labeled the estimator function. The estimator function accumulates the centroids of a given RSO, produces a second order line of fit to counter the centroiding inaccuracies related to a new PSF shape. Since the RSOnet base model has encountered a new PSF shape, the centroiding accuracy is low. The accuracy reduction will be further discussed in section 5.1.5 with the discussion of experimental data. A similar function is applied to extract the brightness values of a known star of a fixed magnitude. The estimator function takes advantage

of the star's constant brightness for photometric calibration of the poorly trained base model. The new centroiding and brightness estimates are collated together with the original RSOnar mission images to produce a new custom labeled training data set. With enough samples collected after a data mining step, the new training data set is used to further train the RSOnet base model to produce the custom RSOnet$_{PCO}$ model. In case of the PCO camera, which is comparable to FAI in many attributes, a further 10 epochs of training with an equal sized sample as the original model is sufficient to improve the accuracy.

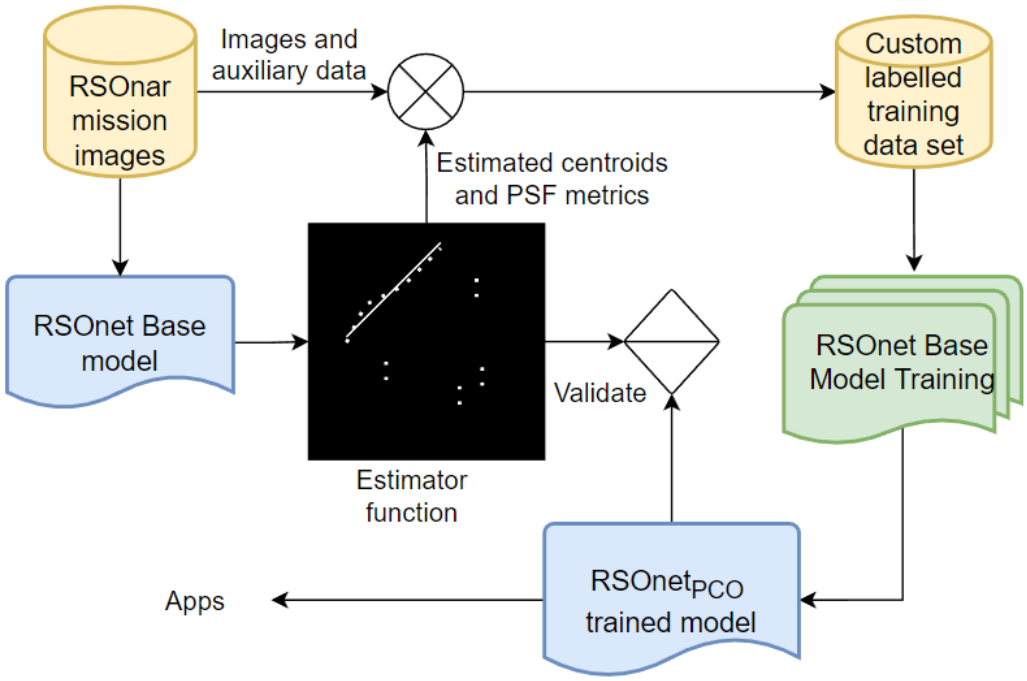

Figure 5.5: Customized training solution for RSOnet$_{PCO}$ using RSOnet base model

A similar methodology is applied to the other camera images. For RSOnet$_{DSLR}$, each color filter is processed separately and then collated together. The CONOPS for the DSLR are similar to PCO and FAI; however, the training data required is significantly larger. The addition of color filters produces novel errors in the centroiding by the estimator function. In such cases, a custom estimator function is required with larger training sets. The case is similar for NEOSSat, GBO$_{Ottawa}$ and Celes-ZWO images. During track mode, the streaking objects requires larger data set and custom filter sizes for training.

5.1.5 Experimental Results

The estimator function for creating centroid labels for RSOnar is illustrated in Figure 5.6 below. The blue dots represent the estimated centroid position as an RSO track is propagated forward by a line of best fit. The line of best fit is calculated using over 200 RSO centroid position from RSOnet base model. As visible in the image, the red centroids are erroneous estimates by the base RSOnet model. By using the blue estimates, a new training sample is generated at each macro or dot where an image sample exists. Using the new training data, the centroiding accuracy of RSOnet base model, at 1.8 pixels, was improved to 0.17 pixels for RSOnet$_{PCO}$. That represents a centroiding accuracy of 6.3 arcseconds.

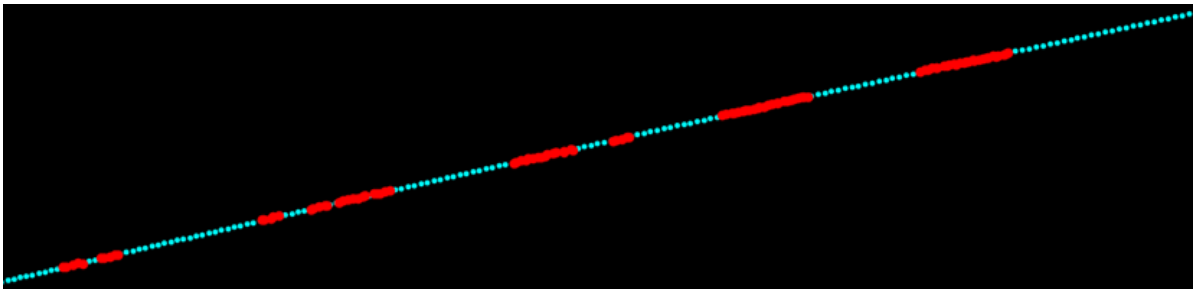

Figure 5.6: Centroiding comparison between RSOnet base model and Estimator function

A similar estimator function was built for estimating the incident flux from a star shown below in Figure 5.7. Each scatter point represents the measured instrumental magnitude of an object using base RSOnet model, where blue and green are two stars and red and purple are two RSO. The solid blue and green lines represent the expected instrumental magnitude of the identified stars. The expected value is calculated using a combination of Equation 2.5 and PCO camera specifications. The detailed version of this calibration involves computing the zero point of the image, calibrating the image against the bias, dark and flat frames and then computing the expected instrumental magnitude of the star. These steps were performed using the Astropy python package.

The expected instrumental magnitude requires robust calibration steps; however, for RSOnet, the largest source of error is the slow movement or shift of the PSF. The synthetic training data does not provide the model with the opportunity to train on a slow moving PSF, wherein the model predicts a varying amount of brightness for the same object shifted half a pixel in either direction. There is a sinusoidal pattern to the shift of the star, demonstrating the base model's brightness

drift with respect to the sub-pixel position. When the flux is centered in the middle of a pixel, the model assumes higher incident flux than when the centroid is on the edge of a pixel. To correct this behaviour, the custom RSOnet$_{PCO}$ training data also includes photometric calibration from stars.

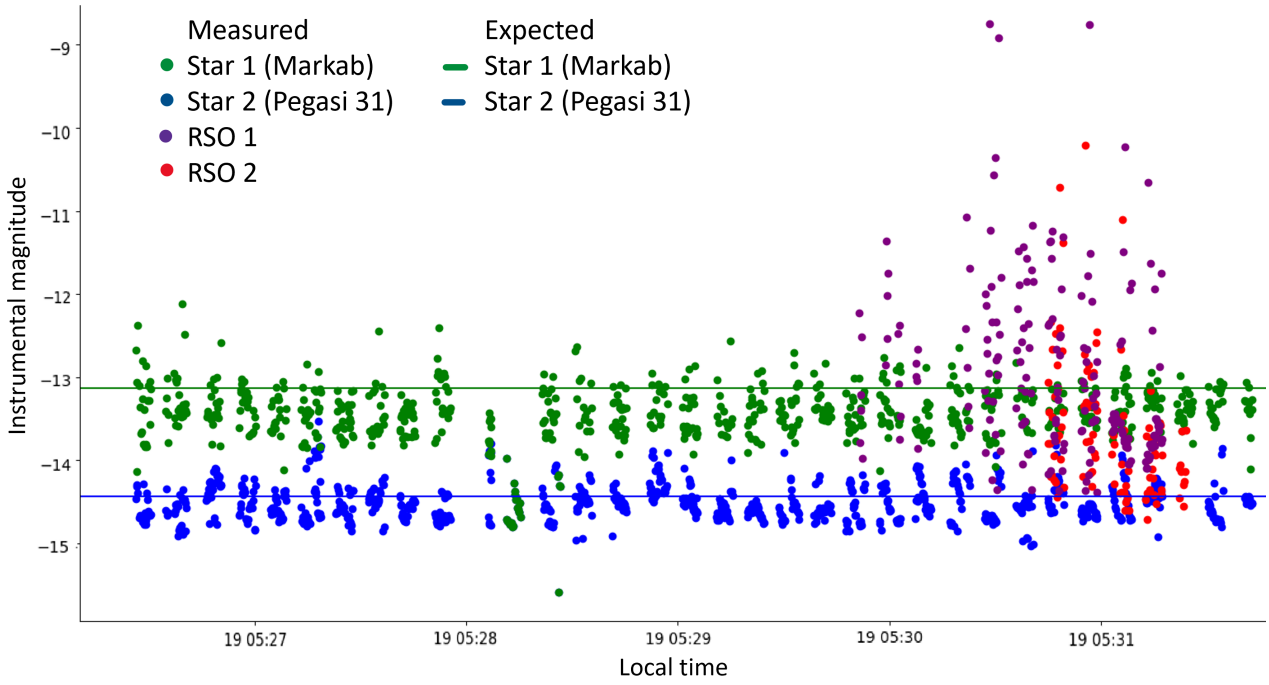

Figure 5.7: Uncalibrated instrumental magnitude over time for sample stars and RSO

Once the new training data is applied, the custom RSOnet$_{PCO}$ model is applied to the same sample stars and RSO as shown in Figure 5.8. The resulting calibrated model filters out some extreme samples in the RSO photometry. Additionally, a more evident trend is observed where the RSO brightness is decreasing over time. Although not all of the sinusoidal behaviour is accounted for, the improved calibration assists in brightness trend convergence faster. Using the custom model yields a 38% improvement in object magnitude estimation as experimented with over 110 star samples. A similar custom training solution, especially if applied over days of observations, can improve photometric analysis accuracy further. Calibration is also possible with RSO observations of known objects with known shape, attitude and position, of which many exist in the public catalog. These RSO offer a unique in-situ calibration opportunity for improved characterization of unknown RSO.

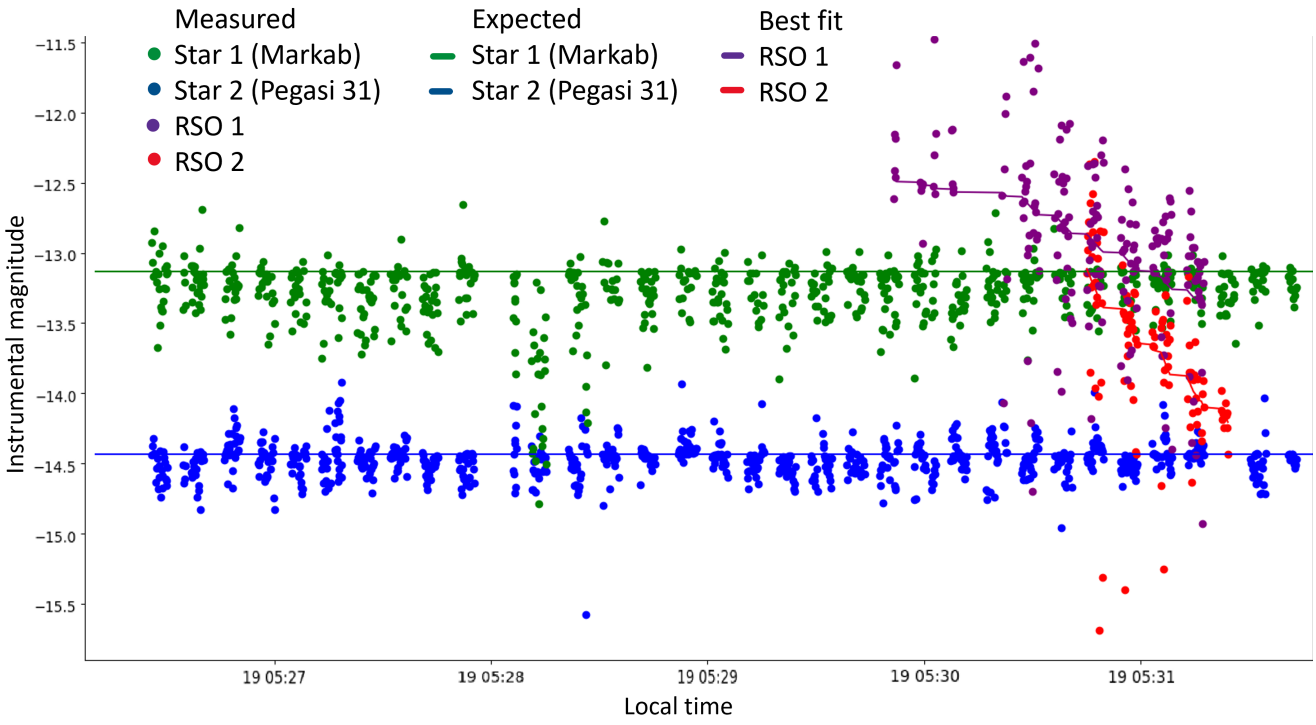

Figure 5.8: Calibrated instrumental magnitude over time for sample stars and RSO

One of the major benefits of photometric analysis is to characterize the RSO, as the brightness of an RSO is the compression of a multi-dimensional observation phenomenon. RSO size, shape, orientation, albedo, solar phase angle, observer instrument and atmosphere all affect this one dimensional characteristic. Light curves collected over many thousands of measurements, in multiple wavelengths of light, from multiple observers can improve RSO characterization accuracy. More research and experimentation is needed to further study the scale of improvement given multi-site observation on photometry for orbit determination as well.

An example of a potentially tumbling RSO is shown in Figure 3.9 below, where the sinusoidal brightness pattern is visible in a long exposure image from the DSLR camera. Work done by Clark [37] and others [49] have demonstrated the potential of detailed characterization by the design of novel simulators. With the use of the bidirectional reflectance distribution function, shape and spin rate estimates are possible.

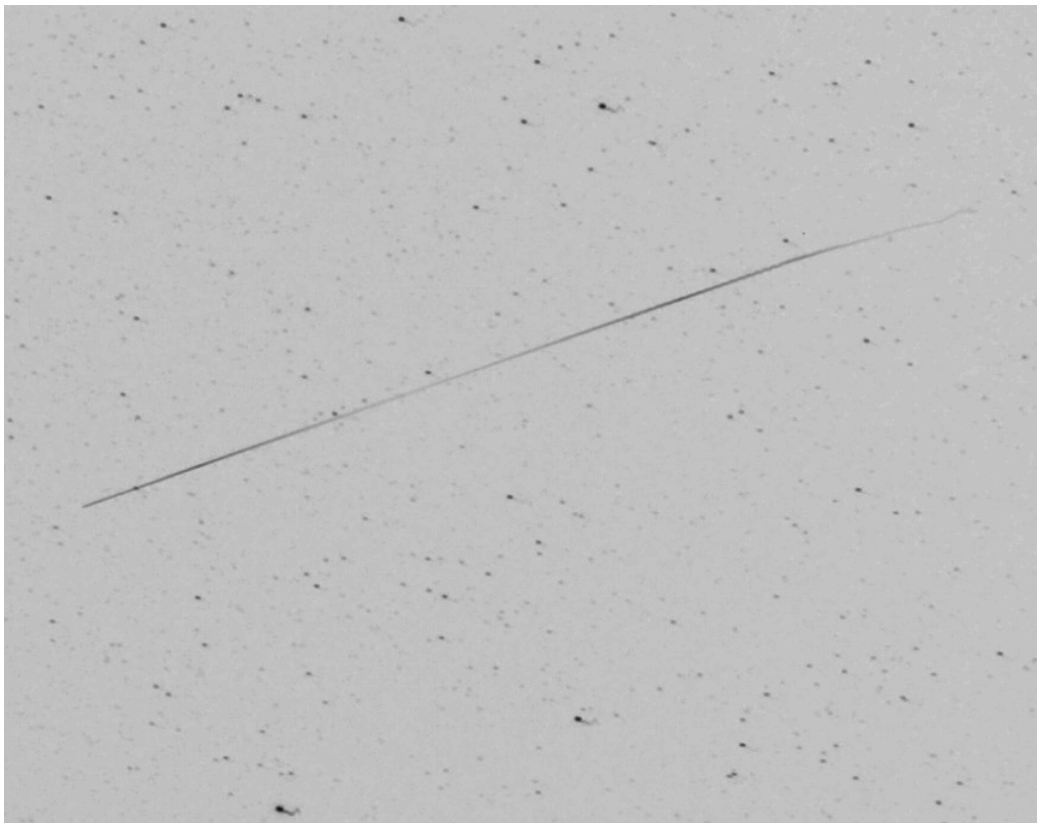

Figure 5.9: The negative image of a long exposure capturing a tumbling RSO with sinusoidal brightness

Overall during the RSOnar mission, over 500 unique RSO detections are predicted by the RSOnet$_{PCO}$ model. This is a considered a conservative estimate as the sensitivity of detection was reduced to optimize for processing time. The total count surpasses the expected value of 10 per hour by ViCAS and previous research [32]. RSOnet$_{PCO}$ achieved expected centroiding accuracy of 6.3 arcseconds, with an ideal classification accuracy of 92%. RSOnet$_{DSLR}$ achieved centroiding accuracy of 2.8 arcseconds and 97% classification accuracy.

RSOnet demonstrates automation of image processing and object characterization on images taken from space and ground-based cameras. The custom models developed for the PCO, DSLR and FAI camera systems are ideal for RSOnet as their CONOPS are similar to star trackers. RSOnet's training customization also makes it viable for on-orbit updates in light of changing PSF characteristics, longer exposure imagery, and tracking smaller debris with high angular rates. It is a lightweight model, well suited for in-situ processing and compression applications on low-power edge-computation hardware. Unoptimized desktop implementation processes images at 1

frame per second in Python. Further improvements can be achieved with additional training on real labeled images.

5.2 Implications for the Space Traffic Camera

The improved performance on the base RSOnet model has important implications for space-based space surveillance. It enables any optical imager to perform surveillance tasks in a statistically random manner. The impact of this novel contribution is described in this section.

5.2.1 Astrometry and Photometry

Astrometry refers to data analysis with the purpose of obtaining information about position and velocity of RSO. To accurately determine the relative position and velocity of the RSO, the star field images need to be tagged with position, velocity and time (PVT) from a Global Navigation Satellite System (GNSS) receiver. A GNSS receiver is a common satellite component, and can be included within the STC payload or externally derived from the host satellite. The host satellite position is Earth-centered, where as the RSO position is relative to the position and orientation of the host satellite body frame. Due to this, the host satellite position and attitude determination accuracy has a direct impact on the accuracy of the RSO PVT estimation. In Figure 5.6, x_i, y_i and z_i refer to the host satellite position coordinates and x_i', y_i' and z_i' to the RSO position referenced to the body frame of the host satellite. The i refers to a particular moment in time the star field image was created. At time step $i+1$, the position and attitude of the host satellite propagate forward in time, influencing the position of the RSO in the star field image.

The body frame orientation, after accounting for the camera boresight offset, can be determined using the STC as a dual-purpose star tracker. A star tracker implementation using STC is already considered feasible, however is out of scope for this research. As discussed in Chapter 2, inertial measurement units commonly accompany star trackers for accurate and reliable attitude determination. Star tracker functionality requires additional memory and processing capabilities for attitude determination, however the star detections are processed using RSOnet. As discussed in Chapter 4, star detection and tracking is a necessity for efficient STC functionality. Paired with an IMU, as commercial star trackers are, the STC can independently determine host satellite attitude.

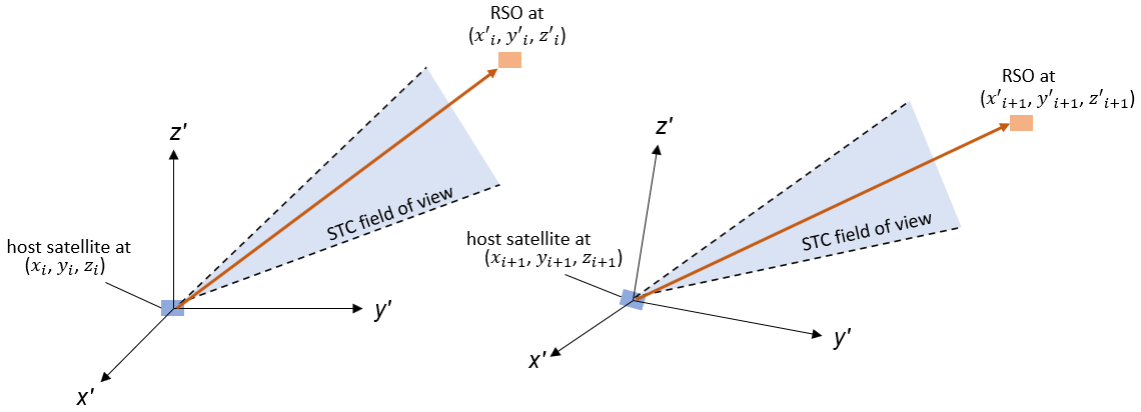

Figure 5.10: Visualizing RSO Positioning relative to host satellite attitude

Results from ViCAS also analyzes the amount of sun exposure for the STC. Exposing an open aperture directly to the sun is damaging to the optical instrument, and a sun sensor is a common hardware component to avoid this situation. The sun sensor allows sunlight to enter through a small aperture and onto a surface covered with photosensitive receptors. The differential light intensity measured in each photoreceptor is used to determine the direction of the light source. Using a sun sensor, specifically for mount configurations most likely to be exposed to the sun, can aid the POBC in determining safe operation modes.

5.2.2 Data Generation and Power Consumption

Evaluating the compressed data produced by RSOnet per image is key to efficient STC operation. However, as a practical implementation the system requires real images to be collected periodically to perform customized training. PSF functions are also known to drift over time due to degrading optical properties and require frequent calibration. This calibration and re-training has to be performed on the ground, as an in-situ implementation is very complicated and resource intensive. To describe the different data downlink requirements, three modes of operation are identified as part of the capture state in Figure 5.3. First capture mode is labeled as minimum operation mode. In this configuration only the processed RSOnet outputs are downlinked from the camera. Second capture mode is labeled as training operation mode. In this mode the detected macros for stars and RSO are downlinked as well as the their RSOnet outputs. Finally, the full frame mode describes the downlink of the entire image and RSOnet output. For ease of comparison, an average of 100

object detections per image will be used as a case study for the PCO camera.

For the minimum operation mode, each image can be RSOnet compressed to 100 rows with 7 attributes, with each attribute equivalent to a 10 bit value. The minimum operation mode yields a compressed image size of 1 kilobyte or 8 kilobits including timestamps, identifiers and auxiliary image data. At a maximum capture rate of 10 Hz, that yields 80 kbps. In-situ classification of stars and RSO, which is a must for attitude determination, can further compress and filter the RSO-only data down to 10 kbps depending on the number of RSO in view. Overall, during operation the range of data generation for downlink ranges between 5 kbps to 50 kbps.

For training operation mode, macros also need to be downlinked where each macro is approximately 400 pixels with 16 bits per pixel. The training operation mode yields an 640 kilobits per image for 100 objects or 6400 kbps at 10 Hz. Some basic compression can be performed to reduce the data rate below 400 kbps by reducing the pixel bit depth, filtering only RSO images, and doing so only for particular RSO. Estimated data rate for full frame mode downlink ranges between 3 mbps and 45 mbps depending on compression.

The data rates described above are estimates based on experimental results of compression on RSOnar mission data. A completed STC design is expected to operate in the minimum operation mode for a majority of the time with a duty cycle that is defined by its orbit and orientation. In this mode, the data generated at the rate of 5 to 50 kbps is considered light by many mission standards and is considered feasible for a hosted payload.

For the RSOnar payload, an average of 10 W was observed during flight. A large portion of the consumption was attributed to the camera and embedded electronics, estimate at nearly 5 W during capture mode and 1.5 W during idle. The POBC and FPGA board selected for the mission was an evaluation kit, which is considered power inefficient and consumed nearly 4 W. Finally the thermal losses for the power converter circuit, additional sensor equipment and secondary payload drew the remaining 1 W of power. COTS star tracker cameras consume between 0.8 to 2.5 W of power for the camera system and another 0.7 to 1.8 W for image processing and attitude determination. This is achieved using custom electronics integration and a stacked assembly with high efficiency components. For the STC, additional data processing for object detection and characterization is not expected to increase the power consumption on the image processing side by a significant amount, especially considering a custom implementation. However, in-situ processing experiment

is necessary to determine true power consumption and data rate requirements. This uncertainty is identified as a key limiting factor for STC adoption.

5.2.3 Contributions to Space Domain Awareness

Variants of the STC are certainly feasible for a large number of satellites that are launched to LEO each year. Additional variations to optimize the aperture size of the camera are also useful methods of improving the utility of each STC. This research has demonstrated the feasibility of the STC as a surveillance instrument for LEO, however further research and development is necessary to commercialize the instrument. At appropriate scale, the STC network has the feasibility to cover LEO in regions where other SDA sensors are not operating such as oceans, overcast regions, non-cooperative nations and light-polluted areas. A standalone STC network would have its own limitations, such as poor accuracy in orbit determination, observing targets beyond GEO and observing in the shadow of the Earth. An integrated STC network with existing ground and space-based radar, passive optical and laser ranging can provide a necessary system-level redundancy. All SDA instruments operate under constraints that cannot always be resolved by a single observer. In a multitude of cases, a secondary observer is used for reference, augmentation or gap-filling. The importance of multiple observers is highlighted by several areas of interesting research, such as light curve completion and forecasting [123], need for 3-dimensional imaging radar for shape characterization [124], multi-exposure imaging [125], sensor network integration with various methods [68] and impact of a conjunction on space surveillance from the perspective of the 18^{th} Space Control Squadron [126].

STC variants can also be upgraded to carry a radio receivers for radar signals transmitted from ground. As shown in Chapter 2, zenith facing cameras yield fewer detections on average; however, a zenith-facing antenna could receive reflected radio signals from RSO thousands of kilometers above their orbit. The reflected radar pulses can also be detected with smaller antennas in orbit, compared to ground, as the signal has to travel shorter distances. A preliminary study of this was conducted previously [127], and is in scope of future technology development research.

6 Chapter Six: Conclusions and Recommendations for Future Work

In conclusion, the research and experimentation presented in this dissertation demonstrates that at scale, space traffic cameras have the potential to offer substantial benefit to the state of our space domain awareness. The study has shown how the commercial instrument known as star tracker imager can effectively add surveillance functionality. Also described are the constraints of the additional functionality and operation. The design has been demonstrated to be compatible with low-power implementations such as a 2U Cubesat. The design constraints are part of the scalability aspect of the idea and it's benefits. These benefits include more frequent detections, longer observation duration, multi-site observations and improved coverage of LEO. The novel contributions of this research highlight and specify the need for a newer surveillance approach and also detail an example that can meet those needs.

6.1 Conclusions

The virtual constellation analysis simulator described in this research estimates that the opportunity to collect thousands of unique and novel observations already exists with existing infrastructure in space and commercial technologies. The improved utilization of the star tracker, albeit an upgraded version, has the potential to produce hundreds of thousands of detections on a daily basis. Centralized effectively, the data collected can be used to develop artificial intelligence algorithms for high fidelity propagators and state estimators to augment current surveillance capabilities in low Earth orbit environment. The contributions of such a network include sub-hourly revisit times, improved characterization with multi-site observations, optical LEO to LEO surveillance of objects

larger than 10 cm and aiding transition from task-based surveillance to search-based surveillance. These results were demonstrated with the design of the virtual constellation analysis simulator or ViCAS. The novel simulator developed for this research has the capability to simulate thousands of RSO and observers. The simulator processes the detection metrics captured from each observer and records them over a 100 minute simulation time. The detection metrics include SNR, distance to RSO, identity and duration of observation. These metrics are defined and explained in context of the low Earth orbit environment. After the observation data is collected, the simulator processes the output data from the propagation steps to provide an overall summary of the surveillance capabilities.

In Chapter 3, multiple scenarios are designed taking into account launch cadence, orbit configurations, camera pointing directionality, camera aperture size, number of observers, number of RSO and background noise. The results of these scenarios are compared against one another and a discussion is provided for the benefits and downsides to each. In this case, the dawn-dusk sun synchronous orbit is certainly the most beneficial; however, other lower inclination orbits (down to 60°) are also suitable with a high observer count. ViCAS is successfully able to illustrate the benefits of surveillance scalability and how they directly address the current SDA limitations. The methodology outlined in this dissertations addresses gaps and limitations in optical surveillance such as weather constraints and atmospheric distortion, distance between observer and RSO, sensor utilization and multiplicity, cost-effective and geographically distributed.

Space traffic camera, described as a modest evolution of the star tracker, is a low-cost and scalable instrument feasible on a nanosatellite. This compatibility constraint is demonstrated as part of the sub-orbital RSOnar mission, which is designed as a 2-U CubeSat. Images captured by a STC have evidently shown RSO detections in multiple real-world scenarios from ground, sub-orbital and orbital observation platforms. This research also discusses the automation of an image processing framework, described as RSOnet, for detection and characterization of RSO and stars. The dual functionality enables the hardware to continue to fulfill it's star tracker role for a host satellite, while passively collecting surveillance data. Further customized training solutions have demonstrated accuracy improvement of 38% for light curve estimation. A similar improvement

is demonstrated with RSO centroiding, with a cross-track accuracy of 2.8 to 6.3 arcseconds and classification accuracies above 90%. Although the STC is not limited to nanosatellites, the qualitative assessment of the smallest STC variant is described and detailed. The proposed model of implementation also improves upon the utility of space infrastructure, with opportunity to generate revenue for satellite owner/operators. Small aperture cameras are potentially capable of detecting thruster firings from large distances, aiding in remote sensing of luminous events like launch or re-entry thruster firings, maneuver detection and explosive events. Opportunistic surveillance can also contribute to observing and characterizing rare events such as orbital conjunctions. Furthermore, the quantity and high dimensionality of the observations, from a photometric perspective, can improve satellite shape and atttitude determination for anomaly analysis and high fidelity orbital propagators.

The quantitative approach to data collection for space domain awareness has the potential to automate and improve upon a majority of SDA objectives. The STC is a highly practical instrument chosen for increasing the data collection capacity by an order of magnitude compared to current methods, and further research is needed to demonstrate this capability. In addition to the multiplicity of observations, optical observations have a high potential for characterization studies which can also improve propagator models. If miniaturized effectively, the STC network concept has the potential for cost savings and improved performance in the field of space domain awareness.

In addition to the simulation efforts, the sub-orbital mission data has been processed and analyzed to achieve a successful result on the metrics discussed. By utilizing the ViCAS simulator, RSOnet processor and the stratospheric balloon RSOnar mission, the research has effectively described the potential of star trackers as space-based space surveillance sensors. This study has opened new possibilities for the utilization of multiple star trackers, which were previously used only for attitude determination. The successful results of this study pave the way for future developments in the use of star trackers as surveillance sensors and highlight the importance of continued research in this area. Overall, the findings of this paper have significant implications for the future of space surveillance and the advancement of space technology.

6.2 Future Work

There are several aspects of research not in the scope of this dissertation that can be valuable to develop further proof of concept and novel applications.

RSO and Star Identification A robust RSO identification methodology is crucial to developing any SDA services. The detections made by an optical instrument must be correlated to an existing or new RSO catalogue entry. Generally, the propagation of an RSO orbit enables prediction of future observation possibilities which need to be verified and timed via routine identification processes. Several propagation and identification processes should be executed in parallel, in an automated method to adapt to the scale of detections made. Star identification is key to attitude estimation and photometric calibration, such that the zero-point for each image can be computed and used for routine light curve calibration. Although most of these processes can be executed on ground servers, the star identification and localization must be conducted in-situ for accurate attitude estimation.

Multi-site observations and orbit determination Further research is needed to quantify the benefits of multi-site observations for initial orbit determination, custody operations and RSO shape, spin rate and attitude characterization. Large quantities of data need to be collected, processed and verified using the multi-site approach to further reference the quality of individual measurement of an instrument as part of a network of observers.

Photometric characterization A significant area of research is needed for photometric analysis of RSO light curves to determine the benefits of optical instruments in SDA. Single observer photometry, be it intensity-only or multi-spectral, has limited resolution ability. Further research into multi-site photometry has potential to drastically improve attitude and shape estimates of an RSO.

Ground Systems Server for a Benchmark data set Finally, a robust ground system server must be developed to aggregate the large quantities of data collected by various optical instruments. In several case studies, trends are observed having annual periods, which require storage processing

and re-assessment of vast archives of data. Formalizing and centralizing this process is key to the success of a space traffic camera network.

Small Debris Detection Feasibility of detecting small debris, sized 10 cm and below, can be evaluated with existing image data set. At distances below 150 kilometers, smaller debris glints can be sampled and evaluated. As described in Chapter 4, closer objects tend to streak over the star tracker's exposure time and the detected streaks can be used to understand how many pieces of small debris pass within the instrument field of view.

Passive Radio Receiver for SDA A passive phased-array antenna has the feasibility to detect radar pulses with a smaller surface area in orbit. The combination of a STC and passive radio receiver can effectively increase the utility of a space-based surveillance sensor, especially for observing higher orbital shells.

Bibliography

[1] Oltrogge, D. L. The "we" approach to space traffic management. *15th International Conference on Space Operations, 2018*, (June):1–21, 2018.

[2] Lawrence, A., Rawls, M. L., Jah, M., Boley, A., Di Vruno, F., Garrington, S., Kramer, M., Lawler, S., Lowenthal, J., McDowell, J., and McCaughrean, M. The case for space environmentalism. *Nature Astronomy*, 6(4):428–435, 2022.

[3] Rowland, J., McKnight, D., Pino, B. P., Reihs, B., and Stevenson, M. A. A worldwide network of radars for space domain awareness in low earth orbit. 2021.

[4] Ash, A., Skuljan, J., Scott, L., Martin, W., Wright, V., and Bessell, T. A summary of 5-Eyes research collaboration into SSA. *Advanced Maui Optical and Space Surveillance Technologies Conference (AMOS)*, 2018.

[5] Scott, R. and Thorsteinson, S. Key Findings from the NEOSSat Space-Based SSA Microsatellite Mission. *Advanced Maui Optical and Space Surveillance Technologies Conference*, 2018.

[6] Pyrak, M. and Anderson, J. Performance of northrop grumman's mission extension vehicle (mev) rpo imagers at geo. In *Autonomous Systems: Sensors, Processing and Security for Ground, Air, Sea and Space Vehicles and Infrastructure 2022*, volume 12115, pages 64–82. SPIE, 2022.

[7] NASA. Orbital debris quaterly news. *NASA Orbital Debris Quaterly News*, 2021.

[8] Molotov, I., Agapov, V., Kouprianov, V., Titenko, V., Rumyantsev, V., Biryukov, V., Borisov, G., Burtsev, Y., Khutorovsky, Z., Kornienko, G., Erofeeva, A., Litvinenko, E., Aliev, A., Zalles, R., Grebetskaya, O., Likh, Y., Rusakov, O., Minikulov, N., Guliamov, M., Abdulloev,

B., Borisova, N., Irsmambetova, T., Vikhristenko, A., Inasaridze, R., Gubin, E., Erofeev, A., Ivaschenko, Y., Yurkov, V., Matkin, A., Rybak, A., Karaush, D., Letsu, A., Tsibizov, O., Ermakov, B., and Siniakov, E. ISON worldwide scientific optical network. *European Space Agency, (Special Publication) ESA SP*, 672 SP(July), 2009.

[9] Ingram, C., Bishop, J., Cunio, P., Hendrix, D., Jeffries, M. W., and Solutions, E. ExoALERT : 1 Year of AI-Enabled Space Traffic Management Services at GEO. *Advanced Optical Maui Optical and Space Surveillance (AMOS) Technologies Conference*, 2022.

[10] Jah, M. Space surveillance, tracking, and information fusion for space domain awareness. pages 1–18, 2016.

[11] April, J. Nanosat employment : a theoretical CONOPS for space object identification. *Naval Postgraduate School*, 2014.

[12] Office, U. S. G. A. SPACE Development and Oversight Challenges in Delivering Improved Space Situational Awareness Capabilities. (GAO-11-545), 2011.

[13] Gaposchkin, E. M., Von Braun, C., and Sharma, J. Space-based space surveillance with the Space-Based Visible. *Journal of Guidance, Control, and Dynamics*, 23(1):148–152, 2000.

[14] Stokes, G. H., Von Braun, C., Sridharan, R., and Sharma, J. The space-based visible program. *Space 2000 Conference and Exposition*, 11(2):205–238, 2000.

[15] Maskell, P. and Oram, L. Sapphire: Canada's Answer to Space-Based Surveillance of Orbital Objects. In Paxson, C., Snell, H., Griffin, J., Kraemer, K., Price, S., Kendra, M., and Mizuno, D. P. E., editors, *Advanced Maui Optical and Space Surveillance Technologies Conference*, page E5, January 2008.

[16] Du, J., Chen, J., Li, B., and Sang, J. Tentative design of SBSS constellations for LEO debris catalog maintenance. *Acta Astronautica*, 155(June):379–388, 2019.

[17] Hertwig, F. D., Colombi, J. M., Cobb, R. G., and Meyer, D. W. Search-Based vs. Task-Based Space Surveillance for Ground-Based Telescopes. *Advanced Maui Optical and Space Surveillance Technologies Conference*, 2019.

[18] Fang, T.-W., Kubaryk, A., Goldstein, D., Li, Z., Fuller-Rowell, T., Millward, G., Singer, H. J., Steenburgh, R., Westerman, S., and Babcock, E. Space weather environment during

the spacex starlink satellite loss in february 2022. *Space Weather*, n/a(n/a):e2022SW003193. e2022SW003193 2022SW003193.

[19] Perovich, N., Folcik, Z., and Jaimes, R. Satellite maneuver detection using machine learning and neural network methodsbehaviors. In *2022 IEEE Aerospace Conference (AERO)*, pages 01–19. IEEE, 2022.

[20] Mark, C. P. and Kamath, S. Review of active space debris removal methods. *Space Policy*, 47:194–206, 2019.

[21] Ray, V. and Scheeres, D. J. Drag coefficient model to track variations due to attitude and orbital motion. *Journal of Guidance, Control, and Dynamics*, 2020.

[22] Levesque, M. Automatic reacquisition of satellite positions by detecting their expected streaks in astronomical images. In *Proceedings of the Advanced Maui Optical and Space Surveillance Technologies Conference*, page E81, 2009.

[23] SSC Unified Data Library and space fence establish direct sensor connection, Apr 2022. Available at `https://www.ssc.spaceforce.mil/Newsroom/Article-Display/Article/3011293/ssc-unified-data-library-and-space-fence-establish-direct-sensor-connection`.

[24] Decision no 541/2014/eu of the european parliament and of the council of 16 april 2014 establishing a framework for space surveillance and tracking support. *Official Journal of the European Union*, L(158):227, May 2014.

[25] Slavin, M., Wood, D., and Jah, M. *Use of ASTRIAGraph to Inform Detectability, Identifiability, and Trackability Metrics for Space Sustainability*.

[26] Slavin, M. Incentivizing collaboration on space sustainability: Detectability, identifiability, and trackability of space missions, 2020.

[27] Danescu, R. G., Itu, R., Muresan, M. P., Rednic, A., and Turcu, V. Sst anywhere; a portable solution for wide field low earth orbit surveillance. *Remote Sensing*, 14(8), 2022.

[28] Zimmer, P., McGraw, J. T., and Ackermann, M. R. Real-time optical space situational awareness of low-Earth orbit with small telescopes. *AMOS Conference*, 2018.

[29] Cogger, L., Howarth, A., Yau, A., White, A., Enno, G., Trondsen, T., Asquin, D., Gordon, B., Marchand, P., Ng, D., Burley, G., Lessard, M., and Sadler, B. Fast Auroral Imager (FAI) for the e-POP Mission. *Space Science Reviews*, 189(1-4):15–25, 2015.

[30] Yau, A. W. and James, H. G. CASSIOPE Enhanced Polar Outflow Probe (e-POP) Mission Overview. *Space Science Reviews*, 189(1-4):3–14, 2015.

[31] e-pop dataset for the fast auroral imager on-board cassiope. Available at `https://epop-data.phys.ucalgary.ca/`.

[32] Clemens, S. On-orbit resident space object (rso) detection using commercial grade star trackers, 2019.

[33] Dave, S., Clark, R., and Lee, R. S. K. Rsonet: An image-processing framework for a dual-purpose star tracker as an opportunistic space surveillance sensor. *Sensors*, 22(15), 2022.

[34] on Earth Observation Satellites, C. CEOS Virtual Constellations Process Paper. pages 1–14, 2019.

[35] Gasdia, F., Barjatya, A., and Bilardi, S. Multi-site simultaneous time-resolved photometry with a low cost electro-optics system. *Sensors (Switzerland)*, 17(6):1–18, 2017.

[36] Coder, R. D. Multi-objective design of small telescopes and their application to space object characterization. 2016.

[37] Clark, R., Dave, S., Wawrow, J., and Lee, R. Performance of Parameterization Algorithms for Resident Space Object (RSO) Attitude Estimates. *Advanced Maui Optical and Space Surveillance Technologies Conference*, pages 1–14, 2020.

[38] Jolley, A., Bédard, D., and Wade, G. A. Multicolour Optical Photometry of Active Geostationary Satellites. *Advanced Optical Maui Optical and Space Surveillance (AMOS) Technologies Conference*, 2015.

[39] Griffith, N., Lu, E., Nicolls, M., Park, I., and Rosner, C. Commercial space tracking services for small satellites. 2019.

[40] Maffei, M., Aubry, A., Maio, A. D., and Farina, A. On the exploitability of the ka band for spaceborne radar debris detection and tracking measurements. In *2019 IEEE 5th International Workshop on Metrology for AeroSpace (MetroAeroSpace)*, pages 355–360, 2019.

[41] Cognion, R. L. Observations and Modeling of GEO Satellites at Large Phase Angles. *Advanced Maui Optical and Space Surveillance Technologies*, 2013.

[42] Krag, W. E. Visible magnitude of typical satellites in synchronous orbits. 1974.

[43] Hejduk, M. and Lambert, J. Satellite Detectability Modeling for Optical Sensors. *AMOS Technical Conference*, pages 101–110, 2004.

[44] Vallado, D. *Fundamentals of Astrodynamics and Applications*. Springer, New York, NY, USA, 3rd edition, 2007.

[45] Howell, S. *Handbook of CCD Astronomy*. Cambridge Observing Handbooks for Research Astronomers. Cambridge University Press, 2006.

[46] DeMars, K. J., Jah, M. K., and Schumacher, P. W. The use of angle and angle rate data for deep-space orbit determination and track association. *Advances in the Astronautical Sciences*, 136:815–828, 2010.

[47] Cunio, P. M., Bantel, M., Flewelling, B. R., Therien, W., Jeffries Jr, M. W., Montoya, M., Butler, R., and Hendrix, D. Photometric and other analyses of energetic events related to 2017 geo rso anomalies. In *Proceedings of the Advanced Maui Optical and Space Surveillance (AMOS) Technologies Conference*, 2017.

[48] Früh, C., Kelecy, T. M., and Jah, M. K. Coupled orbit-attitude dynamics of high area-to-mass ratio (hamr) objects: influence of solar radiation pressure, earth's shadow and the visibility in light curves. *Celestial Mechanics and Dynamical Astronomy*, 117(4):385–404, Dec 2013.

[49] Kabayashi, D. and Frueh, C. Reformulating Compressed Sensing to be used with Semi-Resolved Point Spread Function and Light Curves for Space Object Imaging: LEO. *Advanced Optical Maui Optical and Space Surveillance (AMOS) Technologies Conference*, 2022.

[50] Cakaj, S., Kamo, B., Lala, A., Shinko, I., and Agastra, E. The Apsidal Precession for Low Earth Sun Synchronized Orbits. *International Journal of Advanced Computer Science and Applications*, 6(9), 2015.

[51] Gkolias, I., Daquin, J., Gachet, F., and Rosengren, A. J. From Order To Chaos in Earth Satellite Orbits. *The Astronomical Journal*, 152(5):119, 2016.

[52] Nastasi, K. M. and Black, J. *An Autonomous Sensor Management Strategy for Monitoring a Dynamic Space Domain with Diverse Sensors*.

[53] Hoots, F. R. and Roehrich, R. L. Spacetrack Report No. 3–Models for Propagation of NORAD Elements Sets. *Spacetrack Report*, 3(3):1–91, 1980.

[54] Klinkrad, H. and Fritsche, B. Orbit and attitude perturbations due to aerodynamics and radiation pressure. In *ESA workshop on space weather, ESTEC, Noordwijk, Netherlands*, 1998.

[55] Pastor, A., Escribano, G., Sanjurjo-Rivo, M., and Escobar, D. Satellite maneuver detection and estimation with optical survey observations. *The Journal of the Astronautical Sciences*, pages 1–39, 2022.

[56] Thomas, D. J., Nastasi, K. M., Schroeder, K., and Black, J. T. Autonomous multi-phenomenology space domain sensor tasking and adaptive estimation. In *2018 21st International Conference on Information Fusion (FUSION)*, pages 1331–1338, 2018.

[57] Cunio, P. M., Bishop, J., Ingram, C. W., Therien, B., Hendrix, D., Clark, C., Bantel, M., Jeffries, M. J., and Solutions, E. Analysis of Orbit Residual Behavior to Determine Contact in Rendezvous and Proximity Operations at Geosynchronous Orbit. *Advanced Optical Maui Optical and Space Surveillance (AMOS) Technologies Conference*, 2022.

[58] Sanchez, N., Casal, E. O., Ramos-Lerate, M., and Perez, E. M. Space based optical images within a space surveillance system. *International Astronautical Federation - 59th International Astronautical Congress 2008, IAC 2008*, 4(December 2015):2473–2487, 2008.

[59] Harris, C., Thomas, D., Kadan, J., Schroeder, K., and Black, J. Expanding the Space Surveillance Network with Space-Based Sensors Using Metaheuristic Optimization Techniques. *Advanced Optical Maui Optical and Space Surveillance (AMOS) Technologies Conference*, 2021.

[60] Key, C., Ferris, A., Geissbuhler, M., Horwood, J., Aerospace, S., Street, A., and Segundo, E. All-Sky Electro-Optical Tracking of Mega-Constellations in Low Earth Orbit. *Advanced Optical Maui Optical and Space Surveillance (AMOS) Technologies Conference*, 2022.

[61] Payne, T. E., Castro, P., Weisenbach, L., Vantilburg, E., Wilson, M., Godar, T., Wiley, V., Frith, J., Milster, S. P., and Rvsw, A. Peacock : A Persistent Wide-Field-Of-View Simultaneous Multispectral System Based on COTS Hardware. *Advanced Optical Maui Optical and Space Surveillance (AMOS) Technologies Conference*, 2022.

[62] Boer, M. A new tool to observe low and higher earth orbits: the metatelescope. volume 7, 2017. `https://conference.sdo.esoc.esa.int/proceedings/sdc7/paper/305/SDC7-paper305.pdf`.

[63] Krantz, H., Pearce, E. C., Block, A., and Observatory, S. Characterization of LEO Satellites With All-Sky Photometric Signatures. *Advanced Optical Maui Optical and Space Surveillance (AMOS) Technologies Conference*, 2022.

[64] A . Petit, L. . D. H. . T. R. . L. D. . G., A . Rolin. Extraction of light curve from passive observations during survey campaign in LEO , MEO and GEO regions. *Advanced Optical Maui Optical and Space Surveillance (AMOS) Technologies Conference*, 2022.

[65] Nunes, M., Wright, R., Lucey, P., Ferrari-wong, C., Flynn, L., Pilger, E., Imai-hong, A., Zhu, F., Yoneshige, L., Ben, Y., and Sorensen, T. Hyperspectral Thermal Imaging CubeSat for SSA applications Fredrik Bruhn. *Advanced Optical Maui Optical and Space Surveillance (AMOS) Technologies Conference*, 2022.

[66] Jian-li, W., Jin-yu, Z., and Shi-xue, Z. Large fov mobile eo telescope for searching and tracking low-orbit microsatellites and space debris. 2013.

[67] Fitzgerald, G., Zachary, F., Cabello, A., Ansari, V., and FletcherFunke, J. Toward deep-space object detection in persistent wide field of view camera arrays . *AMOS Technical Conference*, 2021.

[68] Peters, E., Brown, M., Lambert, A., Glina, L., Bateman, T., Kruzins, E., Saleem, R., Bessell, T., Spitzer, T., Wang, T., Tripathi, H. D., Kriti, Soire, M., and Zinsli, S. A sensor network for integrated Space Traffic Management for Australia . *AMOS Conference*, 2022.

[69] Yanagisawa, T., Kurosaki, H., and Oda, H. Detection of LEO Objects Using CMOS Sensor. *Transactions of the Japan Society for Aeronautical and Space Sciences, Aerospace Technology Japan*, 14(ists30):Pr 51 – Pr 55, 2016.

[70] Zuehlke, D. Space Image Processing and Orbit Estimation Using Small Aperture Optical Systems. 2019.

[71] Simms, L. M. Space-based telescopes for actionable refinement of ephemeris pathfinder mission. *Optical Engineering*, 51(1):011004, 2012.

[72] Davis, J., Waltho, F., Bramly-Jennings, T., and Symons, J. Sensor management for space-based sensing constellations. *AMOS Conference*, 2022.

[73] Clemens, S., Lee, R., Harrison, P., and Soh, W. Feasibility of Using Commercial Star Trackers for On-Orbit Resident Space Object Detection. 2018.

[74] Clark, R., Fu, Y., Dave, S., and Lee, R. Simulation of rso images for space situation awareness (ssa) using parallel processing. *Sensors*, 21(23), 2021.

[75] Lang, D., Hogg, D. W., Mierle, K., Blanton, M., and Roweis, S. Astrometry.net: Blind Astrometric Calibration of Arbitrary Astronomical Images. , 139(5):1782–1800, May 2010.

[76] Denver, T., Benn, M., Jørgensen, J. L., Jørgensen, P. S., Herceg, M., and Jack, E. Space Debris Detection and Tracking Using Star Trackers. 21:9822, 2019.

[77] Badura, G., Valenta, C. R., and Gunter, B. Convolutional Neural Networks for Inference of Space Object Attitude Status. pages 1–23, 2019.

[78] Jin Choi, J. H. J. U. o. S., Astronomy, T. . U. . K., Astronomy, S. S. I. . K. . H.-S. Y. K., and Science, S. Short-arc orbit determination results and space debris test observation of the OWL-Net. 2017.

[79] Zhang, L., Yang, H., Lu, H., Zhang, S., Cai, H., and Qian, S. Cubature Kalman filtering for relative spacecraft attitude and position estimation. *Acta Astronautica*, 105(1):254–264, 2014.

[80] Delabie, T., De Schutter, J., and Vandenbussche, B. An accurate and efficient Gaussian fit centroiding algorithm for star trackers. *Journal of the Astronautical Sciences*, 61(1):60–84, 2014.

[81] Wan, X., Wang, G., Wei, X., Li, J., and Zhang, G. Star centroiding based on fast gaussian fitting for star sensors. *Sensors (Switzerland)*, 18(9), 2018.

[82] Herbel, J., Kacprzak, T., Amara, A., Refregier, A., and Lucchi, A. Fast point spread function modeling with deep learning. *Journal of Cosmology and Astroparticle Physics*, 2018(7), 2018.

[83] Lin, T.-Y., Goyal, P., Girshick, R., He, K., and Dollár, P. Focal loss for dense object detection, 2017.

[84] Fitzgerald, G., Liu, R., and Asari, V. Geosynchronous satellite detection and tracking with WFOV camera arrays using spatiotemporal neural networks (GEO-SPANN). In Alam, M. S. and Asari, V. K., editors, *Pattern Recognition and Tracking XXXIII*, volume 12101 of *Society of Photo-Optical Instrumentation Engineers (SPIE) Conference Series*, page 1210104, May 2022.

[85] Austin, I., Spencer, R., Williams, B., Aerospace, S., Kramer, S., Fu, K., Noster, T., and Fu, K. Convolutional neural network approaches for deep-space object detection in wide field of view camera arrays. *Advanced Optical Maui Optical and Space Surveillance (AMOS) Technologies Conference*, 2022.

[86] Privett, G., Appleby, G., and Sherwood, R. Image stacking techniques for GEO satellites and a three-site collection. *AMOS Conference*, 2014.

[87] Wozniak, P., Prasad, L., and Wohlberg, B. Moving point source detection and localization in wide-field images. *AMOS Conference*, 2018.

[88] Do, H. N., Chin, T.-J., Moretti, N., Jah, M. K., and Tetlow, M. Robust foreground segmentation and image registration for optical detection of geo objects. *Advances in Space Research*, 64(3):733–746, 2019.

[89] Zhang, Y., Wang, C., Wang, X., Zeng, W., and Liu, W. FairMOT: On the Fairness of Detection and Re-identification in Multiple Object Tracking. *International Journal of Computer Vision*, 129(11):3069–3087, 2021.

[90] Berclaz, J., Fleuret, F., Turetken, E., and Fua, P. Multiple object tracking using k-shortest paths optimization. *IEEE Transactions on Pattern Analysis and Machine Intelligence*, 33(9):1806–1819, 2011.

[91] Hall, D., Calef, B., Knox, K., Bolden, M., and Kervin, P. Separating Attitude and Shape Effects for Non-resolved Objects. *Advanced Maui Optical and Space Surveillance Technologies Conference, Wailea Maui, Hawaii*, 2007.

[92] Furfaro, R., Linares, R., and Reddy, V. Space Debris Identification and Characterization via Deep Meta-Learning. *1st International Orbital Debris Conference*, pages 1–9, 2019.

[93] Mcquaid, I., Merkle, L. D., Borghetti, B., Cobb, R., and Fletcher, J. Space Object Identification Using Deep Neural Networks. *19th Annual Advanced Maui Optical and Space Surveillance Technologies Conference*, 2018.

[94] Krantz, H., Pearce, E. C., and Block, A. Characterizing the all-sky brightness of satellite mega-constellations and the impact on astronomy research, 2021.

[95] Svehla, D. Earth orientation quaternion and modeling the satellite orbit using quaternions. In *36th COSPAR Scientific Assembly*, volume 36, page 3034, January 2006.

[96] Svehla, D. Geometrical theory of satellite orbits and gravity field. *Geometrical Theory of Satellite Orbits and Gravity Field*, pages 261–265, 2018.

[97] Libraro, P., Kasdin, N. J., Choueiri, E. Y., and Dutta, A. Quaternion-based coordinates for nonsingular modeling of high-inclination orbital transfer. *Journal of Guidance, Control, and Dynamics*, 37(5):1638–1644, 2014.

[98] Tadini, P., Tancredi, U., Grassi, M., Anselmo, L., Pardini, C., Branz, F., Francesconi, A., Maggi, F., Lavagna, M., De Luca, L. T., Viola, N., Chiesa, S., Trushlyakov, V., and Shimada, T. Active debris removal space mission concepts based on hybrid propulsion. *Proceedings of the International Astronautical Congress, IAC*, 3(August 2015):2319–2328, 2013.

[99] (SpaceX), S. E. T. C. Designing and Building Safe , Reliable and Demisable Satellites Extremely Low Orbit Insertion Operating Below 600 km. pages 1–14, 2022. Available at `https://www.spacex.com/updates/#sustainability`.

[100] Telesat lightspeed leo network, May 2022.

[101] McDowell, J. Jonathan's space pages, 2019. Available at `https://planet4589.org/space/stats/star/starstats.html`.

[102] Dave, S. and Lee, R. Feasibility of a Virtual Constellation using Small Aperture, Wide Field of View Optical Systems for Space Domain Awareness and Applications. *AMOS Conference*, 2022.

[103] Bédard, D. and Lévesque, M. Analysis of the canx-1 engineering model spectral reflectance measurements. *Journal of Spacecraft and Rockets*, 51(5):1492–1504, 2014.

[104] Sakai, S., Tashiro, Y., Kawada, S., and Sugawa, S. Pixel scaling technology in CMOS image sensors with a lateral overflow integration capacitor. *Kyokai Joho Imeji Zasshi/Journal of the Institute of Image Information and Television Engineers*, 64(12):1944–1950, 2010.

[105] et. al., N. S. COSMOS: ihubble space telescope/i observations. *The Astrophysical Journal Supplement Series*, 172(1):38–45, sep 2007.

[106] Nemati, B., Stahl, H. P., Stahl, M. T., Ruane, G. J., and Sheldon, L. J. Method for deriving optical telescope performance specifications for Earth-detecting coronagraphs. *Journal of Astronomical Telescopes, Instruments, and Systems*, 6(03), 2020.

[107] Ahi, K. Mathematical modeling of thz point spread function and simulation of thz imaging systems. *IEEE Transactions on Terahertz Science and Technology*, 7(6):747–754, 2017.

[108] Cogger, L., Howarth, A., Enno, G., and Yau, A. CASSIOPE FAI Characterization Report Document No : ePOP – 4771 Table of Contents. (June):38–40, 2008.

[109] Meredith, C., Privett, G., George, S., and Feline, W. Novel Image Alignment Technique for Extraction of Astrometry and Photometry from Small Field of View Astronomical Sensors . *Advanced Optical Maui Optical and Space Surveillance (AMOS) Technologies Conference*, 2022.

[110] Kief, C., Hannon, M., Lyke, J., Peters, C., Fronterhouse, D., and Ahlberg, M. SPARC - 1: A New, Improved Modular 6U Spacecraft. *IEEE Aerospace Conference Proceedings*, 2019-March:2–9, 2019.

[111] Li, J. yinizhizhu/GNMOT: Graph Networks for Multiple Object Tracking. *Wacv*, pages 719–728, 2020.

[112] Schulter, S., Vernaza, P., Choi, W., and Chandraker, M. Deep Network Flow for Multi-Object Tracking : Supplemental Material. *Cvpr*, (3):6951–6960, 2017.

[113] Rangesh, A., Maheshwari, P., Gebre, M., Mhatre, S., Ramezani, V., and Trivedi, M. M. TrackMPNN: A Message Passing Graph Neural Architecture for Multi-Object Tracking. (1), 2021.

[114] Raab, H. Detecting and measuring faint point sources with a CCD. *MACE2002 Proceedings*, pages 1–6, 2002.

[115] Liu, D., Chen, B., Chin, T. J., and Rutten, M. G. Topological sweep for multi-target detection of geostationary space objects. *IEEE Transactions on Signal Processing*, 68:5166–5177, 2020.

[116] Berlin Space Technologies. *ST400 Star Tracker Datasheet, Hyperion Technologies*, 2016. `https://catalog.orbitaltransports.com/st400-star-tracker/`.

[117] PCO - Excelitas Technologies Corp. *PCO Panda 4.2 Datasheet*, March, 2021. v104.

[118] ZEISS Corp. *ZEISS Dimension 2/25 Datasheet*, March, 2021.

[119] Ash, A., Skuljan, J., Scott, L., Martin, W., Wright, V., and Bessell, T. A summary of 5-eyes research collaboration into ssa. Advanced Maui Optical and Space Surveillance Technologies Conference, 2010.

[120] Al-Ali, F., Gamage, T. D., Nanayakkara, H. W., Mehdipour, F., and Ray, S. K. Novel Casestudy and Benchmarking of AlexNet for Edge AI: From CPU and GPU to FPGA. *Canadian Conference on Electrical and Computer Engineering*, 2020-August:2020–2023, 2020.

[121] Deak, N., Creţ, O., Echim, M., Teodorescu, E., Negrea, C., Văcariu, L., Munteanu, C., and Hângan, A. Edge computing for space applications: Field programmable gate array-based implementation of multiscale probability distribution functions. *Review of Scientific Instruments*, 89(12):125005, 2018.

[122] Brosser, F., Milh, E., Geijer, V., and Larsson-Edefors, P. Assessing scrubbing techniques for xilinx sram-based fpgas in space applications. In *2014 International Conference on Field-Programmable Technology (FPT)*, pages 296–299. IEEE, 2014.

[123] Goumiri, I., Dunton, A., Muyskens, A., Priest, B., and Armstrong, R. Light curve completion and forecasting using fast and scalable Gaussian processes (MuyGPs) . *AMOS Conference*, 2022.

[124] Anger, S., Jirousek, M., Dill, S., and Peichl, M. Iosis – a high performance experimental imaging radar for space surveillance. In *2019 IEEE Radar Conference (RadarConf)*, pages 1–4, 2019.

[125] Muruganandan, V. A., Lambert, A., Clare, R., and Weddell, S. Improving the Resolution of Low Earth Orbit Objects by Multi-Exposure Imaging and Deconvolution . *AMOS Conference*, 2022.

[126] Ramos, C., Skrehart, B., Hutchinson, D., Thurston, R., and McKissock, D. Report on 2021 COSMOS 1408 Event and Impact to Space Domain Awareness Mission . *AMOS Conference*, 2022.

[127] Dave, S. Design and Prototype of a Phased-Array Antenna for Nanosatellite Radar and Communication Applications, July 2018.